

NUMERICAL MODELLING AND DESIGN OF LOW-RISE
CONCENTRICALLY BRACED FRAMES WITH DOUBLE-PIN
DISSIPATIVE CONNECTIONS

Nicolae Danila

A Thesis in the Department of Building, Civil & Environmental Engineering

Presented in Partial Fulfillment of the Requirements
for the Degree of Master of Applied Science (Civil Engineering) at
Concordia University
Montreal, Quebec Canada

December 2013

© Nicolae Danila, 2013

CONCORDIA UNIVERSITY

School of Graduate Studies

This is to certify that the thesis prepared by

By: Nicolae Ionel Danila

**Entitled: Numerical Modelling and Design of Low-Rise Concentrically
Braced Frames with Double-Pin Dissipative Connections**

and submitted in partial fulfillment of the requirements for the degree of

Master of Applied Science (Civil Engineering)

complies with the regulations of the University and meets the accepted standards
with respect to originality and quality.

Signed by the final examining committee:

Dr. A. Bagchi Chair

Dr. L. Tirca Supervisor

Dr. R. Sedaghati Examiner
External (to program)

Dr. A. Bhowmick Examiner

Dr. A. Bagchi Examiner

Approved by: _____
Chair of Department or Graduate Program Director

Dean of Faculty

Date: _____

ABSTRACT

Numerical Modelling and Design of Low-Rise Concentrically Braced Frames with Double-Pin Dissipative Connections

Nicolae Ionel Danila

Concentrically braced frames, CBFs, are the most popular systems used in seismic areas in Canada, due to their large stiffness. However, after braces buckle in compression, their stiffness is significantly reduced and their hysteresis response, displayed in terms of force-displacement, shows an asymmetric behavior. To overcome this drawback, researchers proposed to add fuses that were conceived to be installed either in braces or brace-to-frame connections. The purpose of these fuses is to dissipate the earthquake input energy, while preserving braces to respond in elastic range. In this thesis, a new type of fuse, designed to be installed in brace-to-frame connections, is proposed. This device is labeled dissipative pin connection. Depending on the level of axial tension/ compression force that has to be transferred from the brace to the connection, this device can be manufactured in single-pin, double-pin and multi-pin configurations.

The objective of this thesis was two-fold: i) to develop design rules for double-pin connections displayed in-line and in-parallel and ii) to study the seismic response of a 4-storey CBF building with and without dissipative connections, located in Victoria, BC.

In this thesis, the computations were carried out by means of OpenSees (open system for earthquake engineering simulation). The numerical model developed for single-pin connection

was calibrated based on experimental tests carried out at the Technical University of Lisbon. Similarly, the double-pin connection was calibrated using the same approach. Based on experimental test results conducted on single pin connections, design rules were proposed. It was concluded that by doubling the pin member and employing the parallel configuration, the load-carrying capacity of the dissipative connection increases two times, while the deflection is similar to that experienced by an equivalent single-pin device.

The second part of this thesis emphasizes comparative results, in terms of the seismic response of a 4-storey CBF building with and without dissipative connections. The design of the seismic force resisting system was conducted according to CAN CSA S16-09 and NBCC 2010 provisions. The seismic response was studied under two sets of ground motions that are representative for Victoria, BC., Canada. Both sets of crustal and subduction ground motions are composed of seven records each.

The results have shown that forces generated in structural members were reduced due to an increase in building period and system ductility. Thus, by lowering the axial force developed in the CBF columns, a reduction of foundation size can be achieved, which implies reduction in the overall building cost. The effect of earthquake type on the building response is also discussed. However, to prove the efficiency of double-pin connections displayed in-line and in-parallel, further experimental tests are required.

Acknowledgements

Foremost, I would like to express my sincere gratitude to my advisor Prof. Lucia Tirca for the continuous support of my Master study and research, for her patience, enthusiasm, motivation and great knowledge. Her guidance helped me throughout the time of research and writing of this thesis, while her iron grasp towards perfection moulded me to the present day and forced me to strive for the very best.

Thank you to Concordia University and their precious professors, who guided, helped me along the way and made my years in university some that I will always remember.

Mom, Dad, Alina and Cristinel you are my spiritual columns of support in a world of shaking structural motivation.

I would like to thank the rest of my former university colleagues Cristina, Gurinderbir, Juan David, Leon, Zhi and Aid for the moments shared during our studies and for teaching me the foundation of a multicultural society. I hope our paths will cross again in the future!

Last but not the least, I would like to thank my wife, Diana for her immense support throughout my thesis, spiritual enlightening and help along every step of this journey. Thank you and I love you.

Table of Contents

LIST OF FIGURES	viii
Chapter 1. Introduction	1
1.1 General	1
1.2 Objectives and Scope	3
1.3 Description and Methodology	3
1.4 Thesis Organization	4
Chapter 2. Literature Review	7
2.1 General Overview	7
2.2 HSS Brace Fuse	8
2.3 Dissipative U-Shape Connection Device	10
2.4 Dissipative Single-Pin Connection Device	12
Chapter 3. Modelling and Design of Dissipative Pin Connections	18
3.1 Introduction of Dissipative Pin Connections	18
3.2 Dissipative Pin Connections	18
3.3 Design and Behaviour of Single-Pin Connection Device	22
3.3.1 Theoretical beam model	22
3.3.2 OpenSees beam model	26
3.4 Validation of the OpenSees model of P-A9 and P-3 joints vs. Experimental Test Results	37
3.5 Numerical Modelling of Double-Pin Connection Device	42
3.5.1 Modelling and Behaviour of Double-Pin Connection with Pins Placed In-Parallel	42
3.5.2 Modelling and Behaviour of Double-Pin Device Placed In-Line	45
Chapter 4. Design and Behaviour of CBF in X-Bracing Configuration	50
4.1 Design of 4-Storey CBF in X-Bracing Configuration	50
4.2 Building Description	50
4.3 Members Design	56
4.3.1 Braces design	56
4.3.2 SFRS Columns and Beams Design	57
4.4 Modeling the 4-Storey CBF Building in OpenSees	59
4.4.1 The OpenSees Framework	59
4.4.2 Modeling of Beams and Columns	60
4.4.3 Braces Modeling in OpenSees	62
4.4.4 CBF model	63
4.4.5 Gusset Plates Modelling Definition	64
4.5 Dynamic Analysis of the CBF System Using OpenSees	67

4.5.1	Selecting the Ground Motions	68
4.5.2	Ground Motions Scaling Procedure	71
4.5.3	Seismic Response of the Studied CBF's	75
Chapter 5.	Seismic Analysis of a 4-Storey Building Equipped with Double-pin Connections Displaced in-Parallel Using OpenSees	88
5.1	Design of the 4-storey CBF Equipped with Double-Pin Connections Displaced in-Parallel	88
5.2	Dissipative Connection Design for the 4-Storey CBF	88
5.3	Ground Motions Scaling Procedure for the 4-Storey Frame with Double-pins Connections	91
5.4	Seismic Response of the Studied CBF with Double-pin Connections	91
5.5	CBF Frames with and without Double-pin Connections: Comparison Results	101
5.5.1	The Analysis Run Time Under Selected Ground Motions	101
5.5.2	Interstorey Drift and Residual Inerstorey Drift resulted for all analyses	102
5.5.3	The Influence of Pinching4 Model Parameters	104
Chapter 6.	Conclusions and Future work	107
6.1	Conclusions	107
6.2	Future work	111
References		113

LIST OF FIGURES

Figure 2.1: HSS brace fuse configuration	9
Figure 2.2: CBF Equiped with U-Shape Connections Displaced parallel and perpendicular to braces's ends	10
Figure 2.3: U-Shape Connection Device	11
Figure 2.4: Pin connection configurations	12
Figure 2.5: Testing Pin Connection in CBF	13
Figure 2.6: Finite element model of the quarter connection	14
Figure 2.7: Deformation phases of the CBF brace with ends pin connections	15
Figure 2.8: Design steps of the pin member and its tri-linear curve	16
Figure 3.1: Dissipative single-pin connection, 3D view	19
Figure 3.2: Detail of dissipative single-pin connection	19
Figure 3.3: 3D view of double-pin connection with pins in parallel	21
Figure 3.4: 3D view of double-pin connection with pins in in-line	21
Figure 3.5: Theoretical elastic beam model	23
Figure 3.6: Theoretical beam deflected shape	24
Figure 3.7: Bending moment redistribution	25
Figure 3.8: Failure mechanism of theoretical beam	25
Figure 3.9: Tri-linear curve	26
Figure 3.10: OpenSees beam model of single pin device	27
Figure 3.11: The geometry of tested specimens PA-9 and P-3	30
Figure 3.12: Theoretical tri-linear curve of the PA-9 and P-3 devices	30
Figure 3.13: Strain along PA-9 pin's height recorded at midspan	31
Figure 3.14: Stress along PA-9 pin's height recorded at midspan	31
Figure 3.15: Numerical modeling of the PA-9 specimen; Schematic representation of pin member in OpenSees	32
Figure 3.16: Strain-Deflection Curves of pin PA-9	33
Figure 3.17: Strain and stress of pin P-3; recorded over its height at the pin's mid-span length	34

Figure 3.18: Numerical modeling of the P-3 specimen; Schematic representation of the pin member in OpenSees	35
Figure 3.19: Strain-deflection curves of P-3 specimen	35
Figure 3.20: Hysteresis loops as per the OpenSees model vs. experimental test	37
Figure 3.21: Failure mechanism of specimens PA-9 and P-3	38
Figure 3.22: Pinching4 material definition	40
Figure 3.23: Normalized cumulative dissipated energy of numerical model vs. physical test: P-A9 and P-3 specimens	41
Figure 3.24: DP-PP connection; Tri-linear curve and 3D Model	43
Figure 3.25: Stress and strain diagram of one of the two pins placed in-parallel, recorded at pin's mid-span length	44
Figure 3.26: Strain deflection curves of one of the two pins placed in-parallel	44
Figure 3.27: 3D scheme of double-pin connection device with pins placed in-line	46
Figure 3.28: The OpenSees model of double-pin connection with pins placed in-line	46
Figure 3.29: Stress and strain diagram of pins placed in-line, recorded at pins mid-span	48
Figure 3.30: Strain deflection curves of both pins placed in-line	49
Figure 4.1: Plan view of the 4-storey building	51
Figure 4.2: Elevation of the 4-storey CBF with participating gravity columns	52
Figure 4.3: Design spectrum for Victoria, B.C.	53
Figure 4.4: Members sizes of the 2D CBF with participating gravity columns	59
Figure 4.5: OpenSees Steel02 material response	61
Figure 4.6: Beams and columns cross-section fibres discretization in OpenSees	62
Figure 4.7: Fibre distribution of braces cross-section, and brace member discretization	63
Figure 4.8: OpenSees model of the 4-storey CBF with participating gravity columns	64
Figure 4.9: Brace to frame gusset plate connection	65
Figure 4.10: Selected Crustal Ground Motions Accelerations	70
Figure 4.11: Selected Subduction Ground Motions Accelerations	70
Figure 4.12: Crustal GM's non-scaled Spectral Acceleration $S_{a(g)}$	72
Figure 4.13: Subduction GM's non-scaled Spectral Acceleration $S_{a(g)}$	73
Figure 4.14: Spectral acceleration of scaled Crustal GM's with the Mean and UHS	74

Figure 4.15: Spectral acceleration of scaled Subduction GM's with the Mean and UHS	74
Figure 4.16: The CBF response in terms of peak interstorey drift	75
Figure 4.17: The CBF time-history response of braces under the C5 record	78
Figure 4.18: CBF time-history response under C5	79
Figure 4.19: CBF time-history response of braces under C7	80
Figure 4.20: CBF time-history response under C7	81
Figure 4.21: CBF time-history response of braces under S2	84
Figure 4.22: CBF time-history response under S2	85
Figure 4.23: CBF time-history response of braces under S4	86
Figure 4.24: CBF time-history response under S4	87
Figure 5.1: Elevation of a 4-storey CBF equipped with double-pin brace-to-column joists	90
Figure 5.2: Inter-storey Drift of CBF with double-pin joists displaced in parallel	92
Figure 5.3: Behaviour of braces of CBF with double-pin connections under the C7	92
Figure 5.4: Time-history response in terms of force-displacement of double-pin joints under C5	94
Figure 5.5: Time-history series obtained for CBF with pins in-parallel under the C5	95
Figure 5.6: Time-history response in terms of force-displacement of double-pin joints under C7	96
Figure 5.7: Time-history series obtained for CBF with pins in-parallel under the C7	97
Figure 5.8: Time-history response in terms of force-displacement of double-pin joints under S2	99
Figure 5.9: Time-history series obtained for CBF with pins in-parallel under the S2	100
Figure 5.10: Time-history series obtained for CBF with pins in-parallel under the S4	100
Figure 5.11: Hysteretic response of double-pin joints with pins in-parallel under C7 Record obtained for different <i>Pinching4</i> material parameters	104
Figure 5.12: Time-history floor displacement series resulted under C7 record when <i>Pinching4</i> material parameters rForceP received 0.65 and 0.45 value	105
Figure 6.1: Proposed Multi-Pins Connection	111
Figure 6.2: Reinforced Multi-Pin Connections	112

Chapter 1. Introduction

1.1 General

Concentrically braced steel frame buildings (CBF), designed to withstand earthquake forces, are widely used in Canada. This system is characterized by a high stiffness-to-weight ratio and limited ductility, whereas brace members are designed to yield in tension and buckle in compression. Thus, the current design philosophy consists of sizing braces to dissipate energy through buckling and/or yielding, while all other braced frame members behave elastically. During the braces hysteresis response, after buckling occurred, deterioration in term of storey shear resistance of the system is observed, as well as an unsymmetrical response. In general, the CBF system is prone to soft-storey mechanism and the replacement of braces becomes time consuming and the labour costs fairly high.

To overcome this drawback, researchers have proposed to add fuses in braces or brace-to-frame joints. In this light, the hysteresis energy is dissipated in fuses, while braces are protected against buckling. On the other hand, researchers have identified failure of brace-to-frame connections that may be brittle when bolts fail in shear. Thus, damages observed from seismic events indicate the stringent need to develop innovative structural systems, able to provide high stiffness, ductility and feasibility of repair.

In order to develop a more efficient system, the concept of braced frame members equipped with dissipative brace-to-column connections is studied. Although this concept is not new, it has not been promoted in seismic design. In this case, the input energy is dissipated during the hysteretic response of joints components. Related to current codes provisions, the European seismic code (Eurocode 8, 2004) states that for concentrically braced frames “the over-strength condition for

connections need not apply if the connections are designed to contribute significantly to the energy dissipation capability” of the system. However, the statement is not followed by specific design requirements. Accordingly, the Canadian Design of Steel Structures standard (S16-09) states that for primary framing members forming the seismic-force-resisting system of conventional constructions, the connections can be “designed and detailed such that the governing failure mode is ductile when the member gross section strength does not control the connection design loads”. Through this statement, the approach of dissipative brace-to-column connections was introduced somehow indirectly.

Initially, the concept of dissipative connections consisted of single-pin devices was proposed and experimentally tested during the European INERD (Innovations for Earthquake Resistant Design) project (Plumier et al., 2004). Further, this research topic has been continued in North America (Tirca et al. 2012a, Tirca et al., 2012b, Tirca et al., 2013). From the aforementioned studies resulted that the capacity of single-pin connections is limited and the development of multi-pin connections is required. A detailed study on the behaviour and design of single-pin connections was carried out by Caprarelli (2012). The main advantage of these types of connections is the replacement costs in case of a failed brace after earthquake. Similarly to dissipative pin connections, friction devices are installed between braces and frames and are designed to transfer axial forces triggered in braces. The difference between friction devices and pin devices consists in the mechanism of energy dissipation.

Therefore, the main purpose of this research is to study the behaviour of dissipative pin connections in various configurations and to investigate the response of low-rise concentrically braced frames equipped with these devices.

This study is conducted by means of the OpenSees (Open System for Earthquake Engineering Simulation) finite element software, which provides researchers with the opportunity to implement several building materials with diverse properties in order to simulate and reveal their behaviour under dynamic loads.

1.2 Objectives and Scope

The first objective is to study the behaviour of dissipative pin connections in various configurations by using numerical modelling and to propose design regulations. This task is based on the results obtained from experimental tests conducted on single-pin device during the INERD project. In this study, two new types of pin devices were developed. They were labelled dissipative connections with pins displaced in- parallel and in-line.

Secondly, the seismic response of a 4-storey CBF building with and without dissipative pin connections was studied by means of OpenSees. Furthermore, the procedure developed to evaluate the type and size of dissipative pin connections is discussed.

Third, a comparative study on the behaviour of concentrically braced frames without and with dissipative pin connections is carried out. This study was conducted based on nonlinear time-history analyses and the studied building was subjected to two sets of ground motions: crustal and subduction.

1.3 Description and Methodology

The above objectives are achieved by solving the following steps:

- Study the pin member's behaviour using the theoretical beam model until the failure of connection is reached. It is noted that the pin member behaves as a four-point loaded beam and is designed to dissipate energy while deflecting in bending.

- Develop the OpenSees beam model and perform nonlinear time-history analysis under quasi-static cyclic loading upon failure. The OpenSees beam model was calibrated against experimental tests results carried out at Technical University of Lisbon, Portugal (Calado, 2004). After calibration, conduct pushover analysis and obtain the backbone curve. Compare the theoretical beam model with the OpenSees beam model.
- Develop the double-pin connection with pins displaced in-line and in-parallel. Then, by following the same procedure as above, study their behaviour and capacity to dissipate energy.

In the second part of this thesis, the behaviour of a 4-storey concentrically braced frame structure, CBF, without and with dissipative connections was investigated. The building was located in Victoria, BC. and was subjected to two categories of 7 ground motions each. Both, the crustal and the subduction effect were analysed. The number of selected records per ground motion set is in agreement with the ASCE /SEI 2007 procedure.

A comparative study is conducted on the seismic response of CBFs with and without dissipative connections. The following parameters are discussed: building period, base shear, inter-storey drift and residual deformation.

1.4 Thesis Organization

The research work is grouped into six chapters. The first chapter covers a brief introduction including a general overview of this thesis' work, a well-defined scope, objectives and methodology. The description and steps to follow in order to complete this study are also given.

Chapter two reveals past studies that was carried out on fuses and more specifically on fuses incorporated either in braces or in brace connections. Various types of fuses reported in the literature are presented. A general overview of experimental tests performed on dissipative single-pin connections that were developed in the frame of INERD project is presented. In this chapter, the impeded need for developing structural systems with dissipative connections is emphasised.

The third chapter shows the results for the single-pin connection device as well as for the proposed double-pin connection with pins placed in-parallel and in-line. The numerical models of pin connections are simulated using the OpenSees finite element software and the employed methodology is explained. A validation against the experimental test results of a single pin connection is also performed.

In the fourth chapter, a 4-storey CBF building with typical gusset plate connections is designed using the CSA/S16-2009 standard (CSA, 2009) and NBCC 2010 provisions. The braced frame building located in Victoria, B.C. is subjected to two sets of scaled ground motions. The input parameters as well as the CBF design are also discussed. Then, the seismic response is studied based on numerical model by using OpenSees. The building response is given in terms of interstorey drift, force-deformation hysteresis loops developed in braces and the residual interstorey drift.

Chapter five illustrates the design of the same 4-storey CBF building where the brace-to-frame gusset plate connections were replaced by dissipative double-pin connections. The seismic response is studied by using the OpenSees software. The same ground motions as those used in the previous chapter are considered. The numerical model of pin connections developed in

Chapter three is used. The same seismic response parameters as those mentioned in Chapter four are discussed for comparison purposes.

Lastly, the final conclusions as well as future work recommendations are given in Chapter six.

Chapter 2. Literature Review

2.1 General Overview

Concentrically braced frames are used as seismic force resistant systems. They are designed to dissipate the seismic input energy through buckling and/or yielding of braces, while in the same time the remaining structural elements are designed to perform in elastic range. This type of braced frame provides a high lateral stiffness, moderate to low ductility and appropriate strength.

However, the bracing system has a few drawbacks as follows:

- high stiffness imposes increases in base shear demand which in turn requires large size of structural members, as well as of the CBF columns' foundations. Overall, the cost of the structural system increases;
- the CBF is prone to concentrated deformations within a floor level which drive the system to a storey mechanism formation;
- when subjected to earthquake loading, braces behave asymmetrical after the buckling capacity was reached;
- replacing the damaged braces after an earthquake event means high cost;
- moderate ductility capacity.

To prevent the braces from buckling during an earthquake, researchers have proposed several types of energy dissipative devices to be incorporated either in braces, (Kassis & Tremblay, 2008), (Desjardins & Legeron, 2010), (St-Onge, 2012) or their connections (Plumier, et al., 2006), (Vayas & Thanopoulos, 2005), (Caprarelli, 2012). In this light, other type of dissipative connections are steel yielding fuse connections (Gray et al. 2010).

These fuses complement the behaviour of braced frame system by providing a symmetrical response. Fuses are designed to yield at a lower force than the buckling strength of braces. Meantime, these fuses constrain the development of tensile capacity of braces. Therefore, structural damage that would normally be triggered in braces is diminished and the system is able to perform in elastic range.

2.2 HSS Brace Fuse

Starting with the year 2000, a fuse system incorporated in a rectangular tube brace was studied at École Polytechnique de Montréal (Rezai et al. 2000), (Kassis & Tremblay, 2008), (Tremblay, et al. 2011). The fuse system consists of a cut performed in the HSS brace along a determined length located at a close distance of the braces' end. This hole is reinforced by four welded angles into either side of the HSS brace. The four angles have to transfer the load between the ends of the brace segments. The angle end legs have been trimmed so that the desired brace tensile resistance was attained. The cut in the angles was designed in such a way that the deformation occurring at a local level would not admit any local angle fractures. The out of plane buckling of the brace at the area of the cut had been prevented by the built-up box as shown in Figure 2.1.

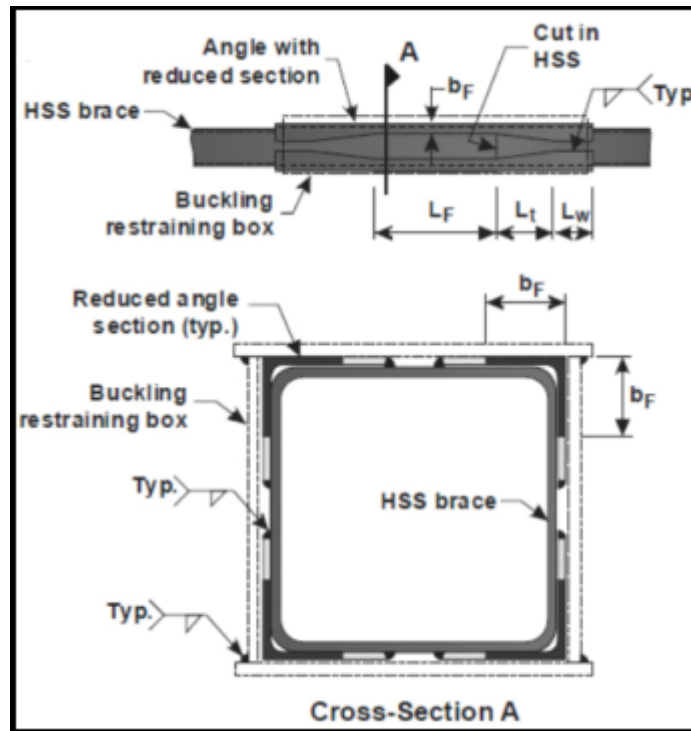


Figure 2.1. HSS brace's fuse configuration (Rezai et al. 2000)

Full scale quasi-static and dynamic tests were conducted for a single diagonal brace and different types of fuse configuration designs. During the tests, the overall fuse exhibited fracture in tension while reaching the designed ductility of its intended design.

It was noticed that the yield of the fuse connection was higher than that of the compressive resistance resulting in the buckling of the brace in compression with the fuse still under yield for the tension cycle side. The solution to minimize this behaviour was to increase the width-to-thickness ratio of the brace cross-section that would then eliminate the low-cycle fatigue failure at the plastic hinge location. The overall study concluded that the ductility demand of the structure had increased and as a result larger deformations were attained.

2.3 Dissipative U-Shape Connection Device

In order to obtain a symmetrical response in tension and compression, dissipative U-shape connections were proposed within the frame of the European INERD project.

This U-shape dissipative connection is illustrated in Figure 2.2 and it consists of a main steel plate bent in U shape. This connection is able to dissipate the input energy when the U-shape plate is subjected to bending.

This type of U-shape connection can be incorporated into a bracing system where the force acting in the brace is transferred perpendicularly to it. To find the optimal behaviour, researchers have proposed two positions of the U-shape member. Thus, the U-shape device was placed perpendicular and parallel to braces as is shown in Figure 2.2. The test set-up is shown in Figure 2.3.

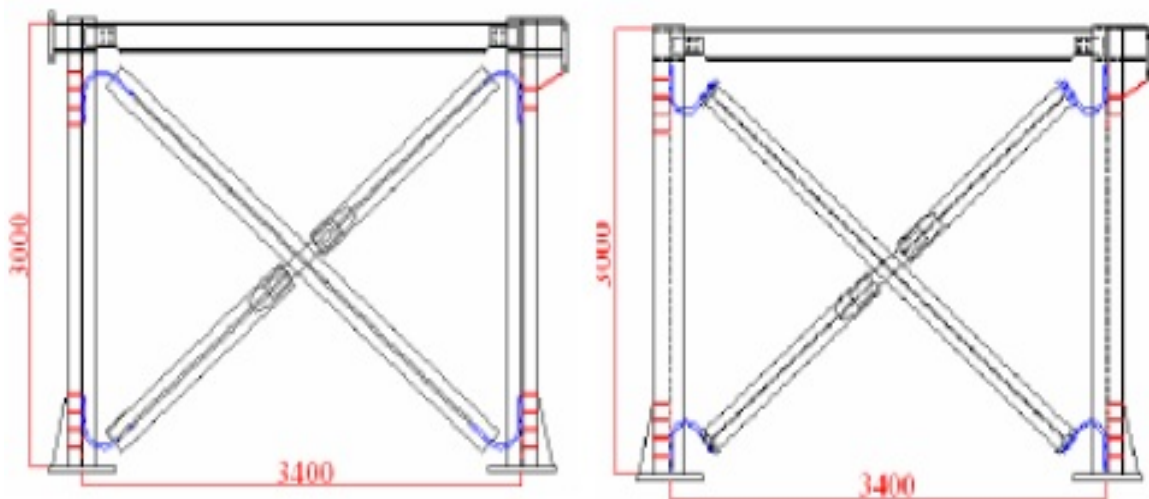


Figure 2.2. CBF equipped with U-shape connections displaced parallel and perpendicular to brace 's ends (Calado et al., 2004)

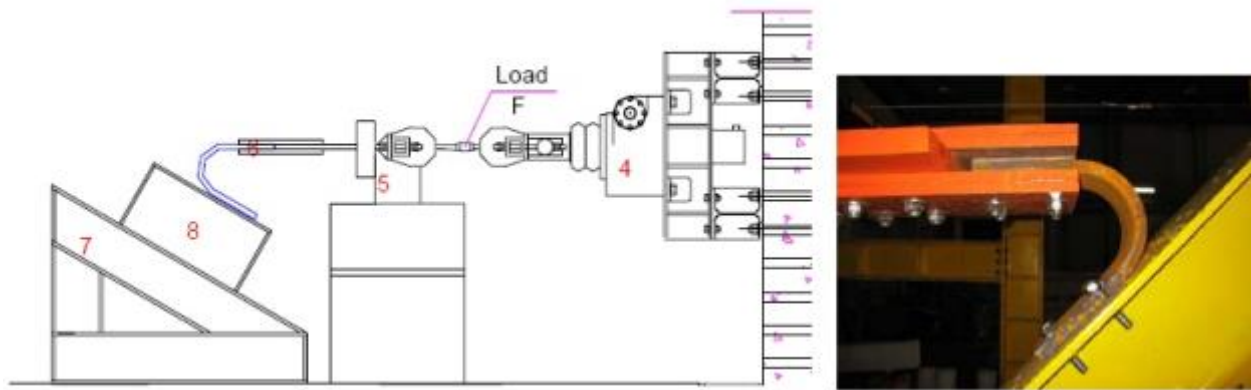


Figure 2.3. U-shape connection device (Calado et al. 2004)

For the U-shape elements to work as dissipative connections, they have to yield in bending before braces, while all other elements of the structure remain elastic.

These U-shape specimens were tested under the ECCS loading protocol (ECCS, 1986).

These U-shape connections comply with the followings:

- The design of these connections was conducted to limit the plastic strains and high residual stresses;
- The connection was designed to have an elongation capacity consistent with the global braced frame deformation in order to satisfy the global drift demand.

The U-shape devices that were tested at the Technical University of Lisbon were made of steel plates with 25 mm and 30 mm thicknesses, respectively. The steel strength was S 355. The amplitudes exerted on these devices were always 40, 80, 120 and 160 mm and the yield displacement was obtained analytically.

It was shown that in terms of the dissipative behaviour, the U-shape devices displaced parallel to braces behaved better than those displaced perpendicular, especially in strength, and

that the dissipative behaviour improves with increasing the radius of the bent plate when forming the U-shape profile.

2.4 Dissipative Single-Pin Connection Device

Another dissipative brace-to-frame connection device is the single-pin type that was also devised and proposed during the European INERD project.

The single pin connection device was subjected to several physical testing procedures at the Technical University of Lisbon, Portugal (Calado L, 2004). These connections were subjected to cyclic loading. Two types of single pin connection configurations are illustrated in Figure 2.4. As shown, the pin member has a rectangular cross-section mounted in its weak axis. The results showed a good behaviour and a symmetrical force displacement loops with same pinching. Then, the single pin connections were incorporated in a full scale single storey CBF in X-bracing configuration and the experimental tests were conducted at Politecnico di Milano

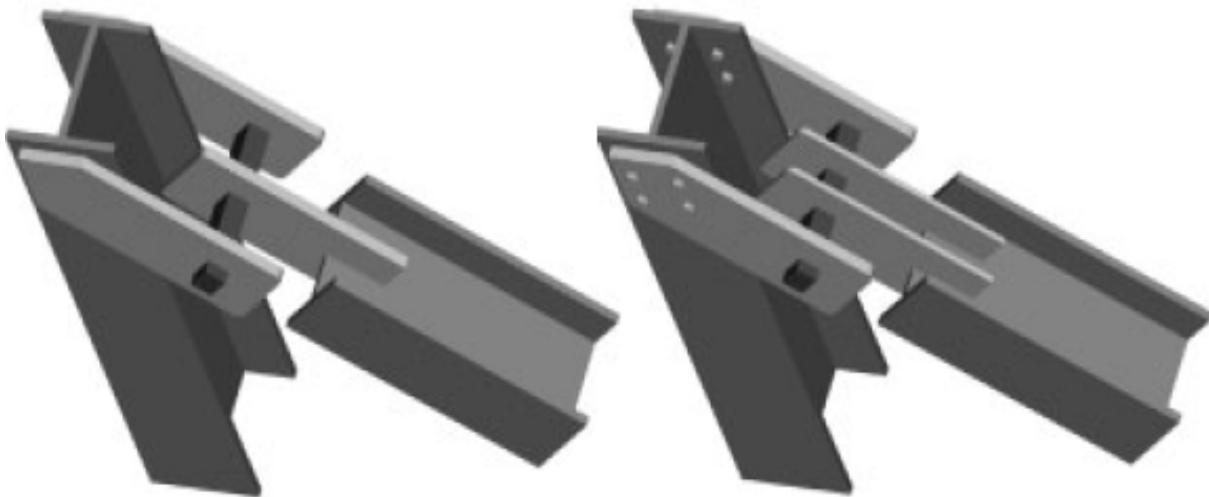


Figure 2.4. Pin connection configurations (Vayas and Thanopoulos, 2005)

(Castiglioni, 2004). The behaviour of a single-pin brace to frame connection is shown in Figure 2.5.

Further on, a numerical finite element model that analyse the behaviour of pin connection had been approached in Athens, Greece (Vayas & Thanopoulos, 2005) by using the software ABAQUS. The model developed for half of single pin connection due to the symmetric shape is presented in Figure 2.6.

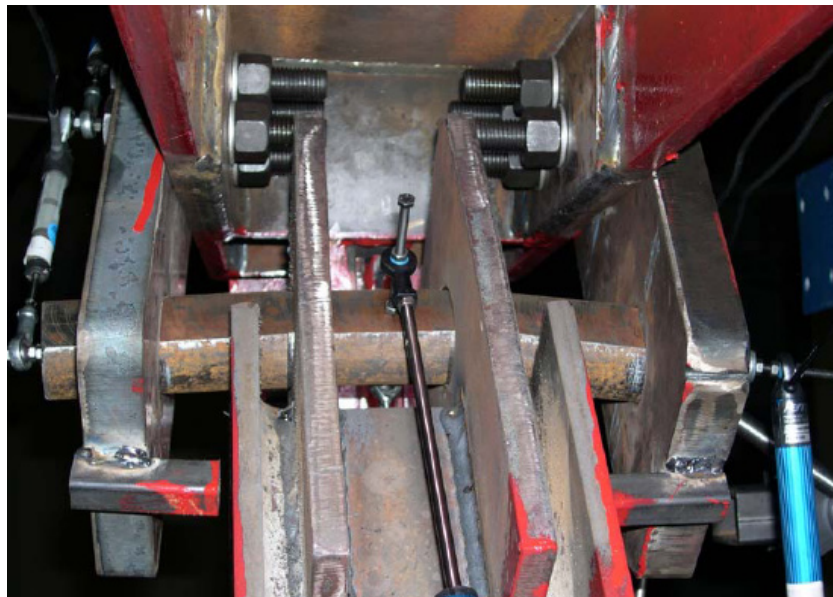


Figure 2.5. Testing Pin connection in CBF (Castiglioni, 2004)

The finite element model developed by Vayas and Thanopoulos (2006) was subjected to several monotonic and cyclic loading in order to note the stress developed in the outer plate and inner plate, as well as, in the pin member. The deflection of pin member and connection components was investigated as well. It was concluded that the main factors that influence the connection behaviour alongside the pin were the thickness of inner- and outer- plates that join the brace to column through the pin member.

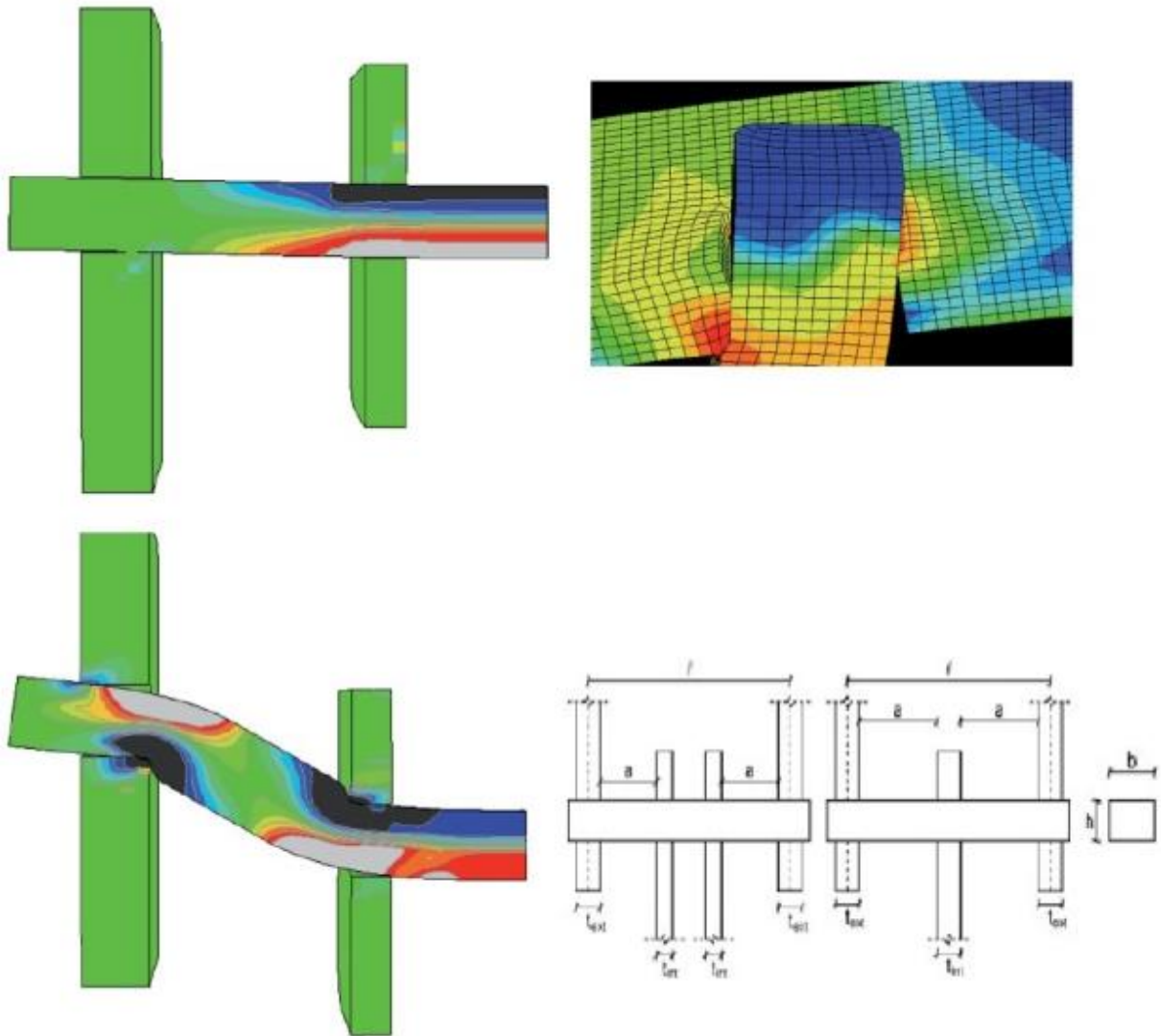


Figure 2.6. Finite element model of a quarter connection (Vayas & Thanopoulos, 2006)

Pinching was observed in the pin connection behaviour after the pin deflected and same clamping forces have developed in the outer plate hole supports. The resulting conclusion was that the pins' yielding behaviour is influenced by its cross-sectional shape and size, as well as by

the distance between inner-plates. In addition, the thickness of the outer-plates influences the pin's behaviour. The thicker the outer plate, the more clamping effect caused by the bearing stress will occur, as well as, an increasing in the overall connection strength was observed. Several design factors were devised. Among them, the thickness of the outer plates should be at least 50% of that of the pin cross-sectional height, while the thickness of inner plates should be larger than 50% of that of outer plates.

It has been observed that when the brace is subjected to tension, the outer plates in the dissipative connection act in tension and they exhibit a deformation towards the exterior, while when the brace is loaded in compression, the outer plates act in compression and they will deform toward the interior as shown in Figure 2.7.

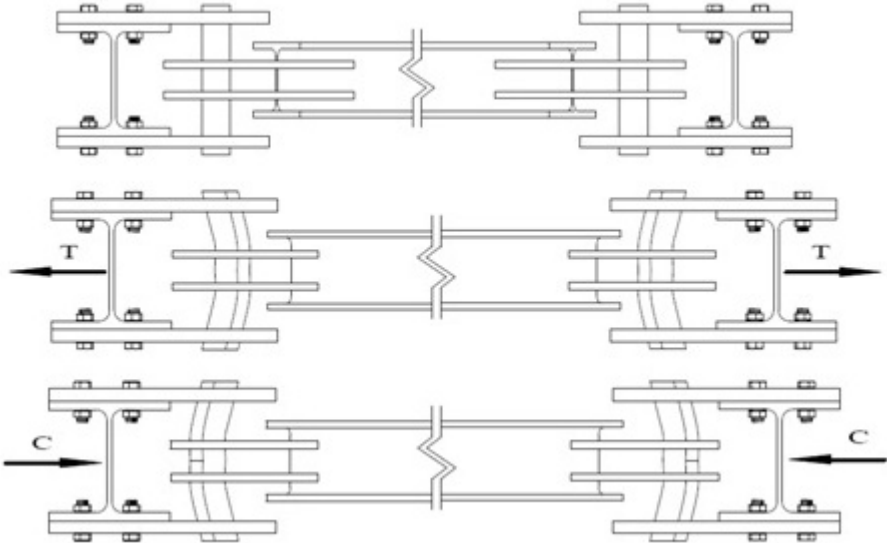


Figure 2.7. Deformation phases of the CBF brace with ends pin connections

In the frame of the INERD project, the single pin connection was numerically studied by using the SOFISTIK finite element. Based on these analysis and experimental tests same design provisions were proposed and are given in Figure 2.8.

The overall European studies concluded that dissipative pin connections provide larger ductility to structure, while maintaining drift requirements and reducing the force induced into the structure. The energy dissipation is higher than that of a regular CBF and all members of the structural frame (brace, beam and column) behave elastically, while the pin connection attains a plastic energy dissipating behaviour.

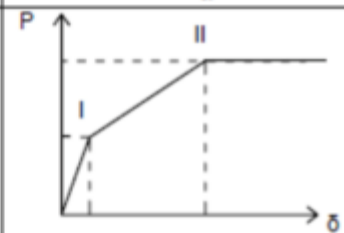
	Force P	Deformations δ
Point I "yielding y"	$P_y = \frac{2 \cdot M_p}{a}$	$\delta_y = 1,5 \cdot \frac{M_p \cdot l^2 \cdot \alpha}{EI} \cdot (3 - 4\alpha)$
Point II "ultimate u"	$P_u = \frac{4 \cdot M_u}{a}$	$\delta_{II} = 0,2 \cdot a$
Deformation capacity		$\delta_{lim} = 0,4 \cdot a$
$M_p = W_{pl} \cdot f_y$, $M_u = W_{pl} \cdot f_u$, $W_{pl} = b \cdot h^2 / 4$ (for rectangular pins) l = pin length, h = pin height, b = pin width a = axial distance between internal and external eye-bars $\alpha = a/l$ f_y = yield stress of pin f_u = tensile strength of pin		

Figure 2.8. Design steps of pin member and its tri-linear curve (Plumier et al., 2004)

Further extensive research regarding the pin dissipative connection had been carried out at Concordia University using the OpenSees finite element software and several other computer

programs (ETABS, Inventor, Femap). Research conducted in this field was disseminated by Tirca et al. (2011), Tirca et al. (2012a, 2012b), Caprarelli (2012). For example Caprarelli (2012) studied the behaviour of a single-pin connection device and its behaviour when installed in a single and two-storey building located in Victoria, BC. All analyses were conducted in OpenSees.

The research carried out in order to study the behaviour of a single-pin connection device and the overall results obtained by analysing 1- and 2-storey CBFs with incorporated pin connections concluded to the following:

- The dissipative energy capacity of connection devices increases when larger distance between inner-plates is provided;
- Fatigue strength curves like the ones presented in Eurocode 3 (European Committee for Standardization) allow predicting the stress range and number of stress cycles to fatigue failure. Low cycle fatigue failure is not a typical failure mode for these devices;
- Ground motions with dominant short periods impose less deformation and less shear forces upon the CBF with dissipative pin connection;
- For middle-rise buildings located in seismic area with high risk, pins transferring large axial forces are required. Thus, the double-pin brace-to-column connections are recommended instead of single-pin devices (Caprarelli, 2012).

The next Chapter will continue the work abovementioned by proposing two new connections labelled double-pin connections with pins placed in-line and in-parallel.

Chapter 3. Modelling and Design of Dissipative Pin Connections

3.1 Introduction of Dissipative Pin Connections

This chapter is based on the paper “Numerical modelling of dissipative pin devices for brace column connections” (2013) co-authored by Tirca, Danila and Caprarelli. The computation of strain-deflection curves resulted for the single-pin connection displaced in two configurations, all calculations regarding the double-pin connections, and the comparison between single pin and double pin connections were carried out by Danila, while the OpenSees model of the single-pin connection device and its calibration with the experimental test results were developed by Caprarelli (2012).

The main purpose of this chapter is to illustrate the behaviour of dissipative double-pin connections device versus the single-pin through numerical modelling and parametric studies by using the OpenSees framework (McKenna et al. 2009). The proposed design methodology and numerical models are validated by means of results obtained from existing experimental tests that were carried out for single-pin connections only. The innovative double-pin connection with pins displaced in-parallel and in-line, proposed herein, has large redundancy and is recommended in design.

3.2 Dissipative Pin Connections

The single-pin fuse integrated in brace connection was initially proposed and experimentally tested in the frame of the European INERD project (Plumier et al., 2006). The single-pin connection that joins the brace to column (Figure 3.1) consists of two outer-plates

welded or bolted to column flanges, two inner-plates welded to the brace and a rectangular pin member with rounded corners running through the four plates, as illustrated in Figure 3.2.

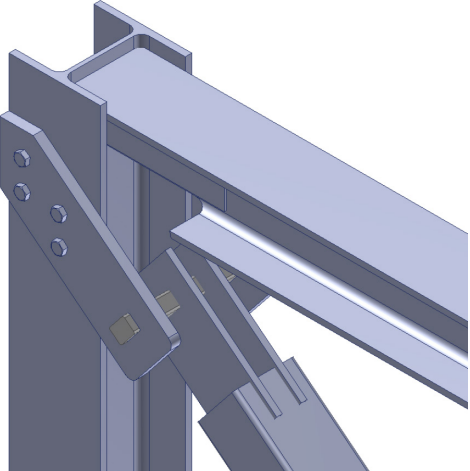


Figure 3.1. Dissipative single-pin connection, 3D view

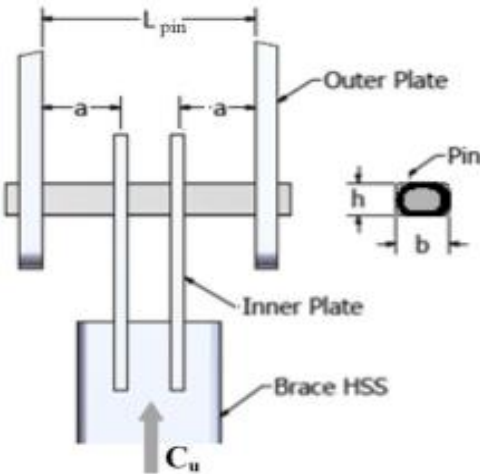


Figure 3.2. Detail of dissipative single-pin connection

As illustrated in Figures 3.1 and 3.2, the configuration of the pin device depends on the size and depth of the CBF column's cross-section that governs the pin's length, L , while the size of the pin member depends on the probable compressive resistance of the connected brace, C_u ,

and the distance between the inner-plates (L-2a). As illustrated in Figure 3.2, parameter “a” is the distance between the outer-plate and the centerline of the inner-plate. The pin element is proportioned to yield in flexure under a force equating 60% C_u of attached hollow structural section (HSS) brace (Caprarelli, 2012).

In this study, the behaviour of single-pin device is analyzed through numerical modelling, developed in the OpenSees framework version 2.2.0 (McKenna et al., 2009). Then, the calibration of the single-pin connection model against results obtained from experimental tests, conducted at Instituto Superior Technico of Lisbon (IST), Portugal (Plumier et al., 2006) is discussed. When large axial forces need to be transferred from braces to CBF columns through connections, the available sizes of single-pin member are not sufficient. To overcome this drawback, an innovative double-pin connection with pins displaced either in-parallel or in-line is proposed, and the 3D view of this device depicted in both configurations is illustrated in Figures 3.3 and 3.4, respectively. By employing the same design approach as that used for the single-pin device, the double-pin connection is analyzed through theoretical and numerical modelling in the aim of sizing the specimens and preparing the upcoming experimental tests.

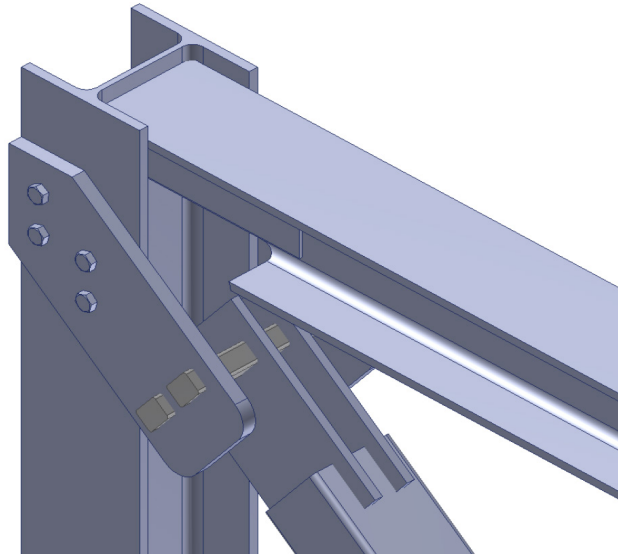


Figure 3.3. 3D view of double-pin connection with pins in-parallel

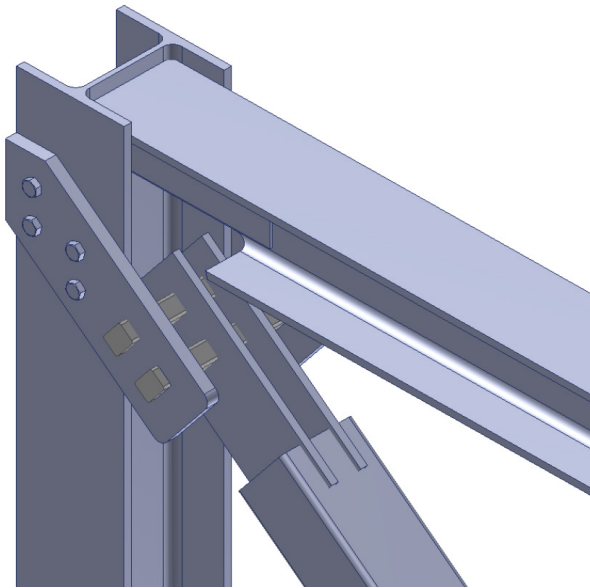


Figure 3.4. 3D view of double-pin connection with pins in-line

3.3 Design and Behaviour of Single-Pin Connection Device

To validate the design method for the single-pin connection device, two numerical models are employed and defined as follows: the theoretical beam model and the OpenSees beam model. Regarding the theoretical beam model, the same approach considered by Vayas and Thanopoulos (2005) and refined by (Tirca et al. 2012) is used to size the pin cross-section and the connection's member components. Then, the theoretical beam model was replicated in the OpenSees framework with the aim of investigating the development of stresses versus strain along the pin cross-section, as well as the length of plastic zone resulted under incremental static loading up to the point of failure. By using data from both theoretical and OpenSees beam models, two experimental tests conducted at IST Lisbon under quasi-static displacement loading were replicated. The calibration of the model was validated when both the experimental and simulated models match in terms of hysteresis loops generated from plotting the force versus displacement and the cumulative dissipated energy.

3.3.1 Theoretical beam model

The behaviour of the single-pin device in terms of its capacity to dissipate energy under cyclic loading is influenced by the following parameters: the length of the pin, L_{pin} , its cross-sectional shape and size, as well as the distance between the inner-plates ($L-2a$). As illustrated in Figure 3.5, the axial force developed in the brace, P , is transferred to the pin through the two inner-plates as uniformly distributed loads which act along the thickness of the plates. For simplicity, the pin is considered to behave as a four-point loaded beam, where the concentrated load $P/2$ is the resultant of the uniformly distributed force, as illustrated. When the yielding moment $M_y = W_y F_y$ is reached, the pin starts to yield in bending under the applied point load

$P_y/2$, where $P_y/2 = M_y/a$. By employing Hooke's law, yielding of the pin is initiated when the maximum normal strain that is developed at the top and bottom fibre of the rectangular pin's cross-section ($b_p \times h_p$) is $\epsilon_y = F_y/E$, where b_p and h_p are the dimension of pin's cross-section and E is the modulus of elasticity.

Thus, under the applied $P_y/2$ loads, the simply supported beam deflects in single curvature as illustrated in Figure 3.6. It is noted that 1 mm clearance was provided between the pin and the outer-plate hole, which meets the requirements of the current standard.

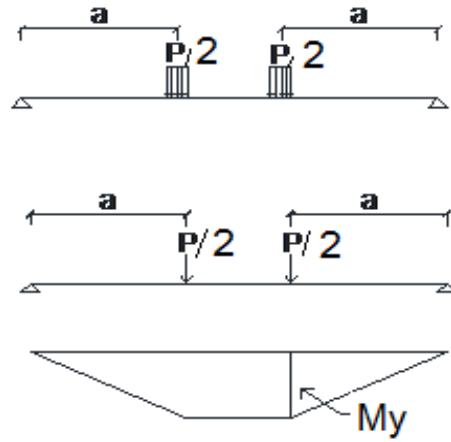


Figure 3.5. Theoretical elastic beam model

The deflection required to produce the material's yielding at the pin's mid-span is $\delta_y = \rho(1 - \cos(L_{pin}/2\rho))$, where ρ is the radius of curvature and the curvature is defined as $k_y = 1/\rho = 2 \epsilon_y / h_p$. However, the strain corresponding to the static yield stress may be two to five times the yield strain ϵ_y (Ziemian, 2010). At this stage, the strain considered to compute the static yield stress, ϵ_1 , is expressed as: $\epsilon_1 = 1.5\epsilon_y$, the corresponding curvature becomes $k_1 = 2(1.5\epsilon_y)/h_p$ and $\rho_1 = h_p/(3\epsilon_y)$. The maximum deflection computed at the pin's mid-span is given by Equation 3.1 and

the maximum deflection under the point of loading may be obtained by multiplying δ_y with the ratio $2a/L_{pin}$. Although the provided deflection equation applies rigorously for the case of pure bending, as is the segment between inner-plates, the assumption that the cross-sections remain plane and perpendicular to the deformed axis leads to expressions for normal strain ϵ and stress σ that are quite accurate in the elastic range even in the case of non-uniform bending ($dM/dx = V(x) \neq 0$), as are the segments between the outer- and the inner-plate.

$$\delta_y = \delta_I = (h/3\epsilon_y) (1 - \cos (1.5L_{pin}\epsilon_y/h_p)) \quad (3.1)$$

The yielding moment, $M_y = W_y F_y$, is reached under the application of two $P_y/2$ loads that are defined in accordance with Equation 3.2.

$$P_I = P_y = 2M_y/a \quad (3.2)$$

For a rectangular cross-section, the ratio between the plastic moment M_p and M_y equates the shape factor given by $W_y/W_p = 1.5$. After the attainment of M_y , some clamping forces start developing at the pin's ends and in consequence the boundary conditions gradually allow the development of end bending moment (Figure 3.7).

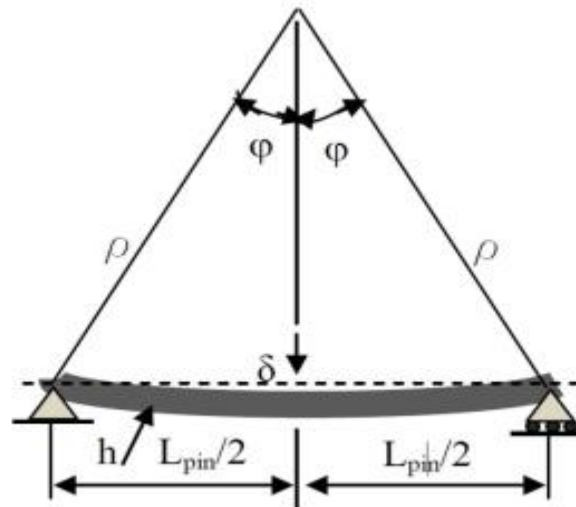


Figure 3.6. Theoretical beam - deflected shape

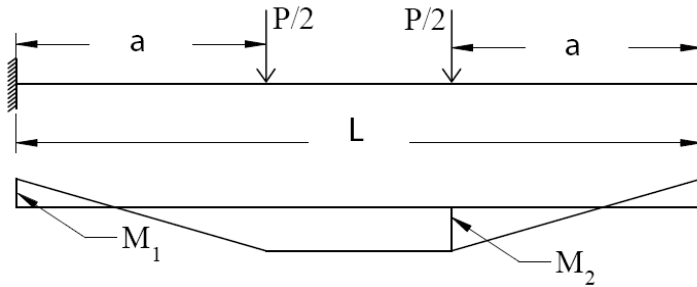


Figure 3.7. Bending moment redistribution

By equating the external work, $P\delta/2 = P(\phi a)/2$, with the internal work, $(M_1 + M_2)/\phi$, where ϕ is the rotation as illustrated in Figure 3.8, the magnitude of the ultimate load carried by the beam, P_{II} , is given in Equation 3.3. It is estimated that the ultimate flexural capacity of the pin member, M_u , is computed as: $M_u = W_p F_u$, where F_u is the steel ultimate strength. Under the two-point loads $P_u/2$, the ultimate strain, ϵ_{II} , is approximated as being equal to $\epsilon_{II} = 50\epsilon_y = 0.1$ and the corresponding curvature is $k_{II} = 2\epsilon_{II}/h = 0.2/h_p$. The value of the ultimate plastic rotation, ϕ_u , becomes $\phi_u = k_{II} l_p = l_p (0.2)/h_p$ radians. Herein, the length of the plastic hinge, l_p , is anticipated as being 1.25 times the height of the pin's cross-section, h_p . As presented hereafter, the development of the plastic hinge length may vary with the distance between the inner-plates and the magnitude of the applied forces.

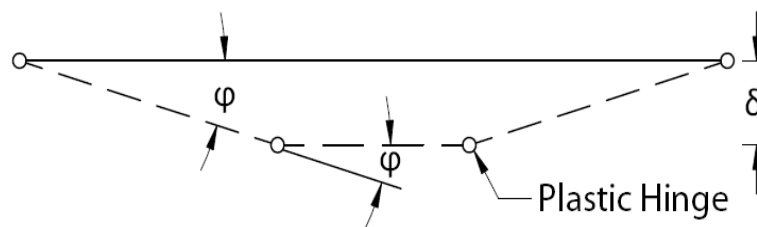


Figure 3.8. Failure mechanism of theoretical beam

The ultimate deflection, δ_{II} , at distance a from the pin's support is given in Equation 3.4.

$$P_{II} = P_u = 2(M_1 + M_2)/a \sim 4M_u/a \quad (3.3)$$

$$\delta_{II} = \varphi_{II}a = \delta u = (lp/h)(0.2a) = 1.25(0.2a) \quad (3.4)$$

During the incursions in plastic range, the magnitude of load P_{II} may slightly increase due to material strain hardening to a value P_{III} , while the maximum deflection of pin at failure is estimated to be $\delta_{III} = 0.4a$ (Vayas & Thanopoulos, 2005); (Thanopoulos, 2006).

From the above it was found that the failure mechanism depicted in Figure 3.8 is formed when plastic hinges are developed at the location of inner-plates where loads are applied. By employing Equation 3.1 to Equation 3.4 and the parameters at failure: P_{III} and δ_{III} , the pin response follows a tri-linear curve as illustrated in Figure 3.9.

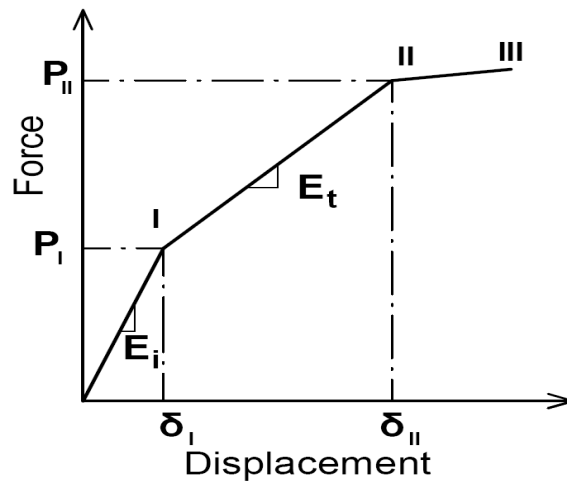


Figure 3.9. Tri-linear curve

3.3.2 OpenSees beam model

The purpose of developing the OpenSees beam model is to simulate the behaviour of the pin in its outer-plate supports and to measure the developed strains, stresses, and deformations. Thus, until the yielding moment is reached, the pin behaves as a simply supported beam. Then,

by increasing the applied loads, the pin member behaves in the plastic range and its deformed shape causes bearing pressure to the contact surface of the outer-plate hole, which is the pin's support. In this stage, bending moment is generated at both pin ends and its magnitude is incremented until the pin reaches its failure mechanism. The development of bending moment diagram across the pin's length depends on the pin-to-outer-plate stiffness ratio, $(I_{pin}/L_{pin})/(I_{op}/H_{op})$. When the aforementioned ratio approaches zero, the pin member imposes no restraint on joint rotation and it behaves as a pure fixed-fixed member, while it triggers the largest axial compression force. It is desirable to optimize the size of outer-plates such that the mid-span bending moment to be slightly larger than that developed at the pin's support. To satisfy this demand, the outer-plate should be sized to comply with the following expression:

$$(I_{pin}/L_{pin})/(I_{op}/H_{op}) = 0.5.$$

Therefore, the OpenSees beam model was built to simulate the behaviour of the pin member acting as a four-point loaded beam, as previously described.

The model shown in Figure 3.10 consists of eight nonlinear beam-column elements with distributed plasticity and four integration points per element. The pin's cross-section is made

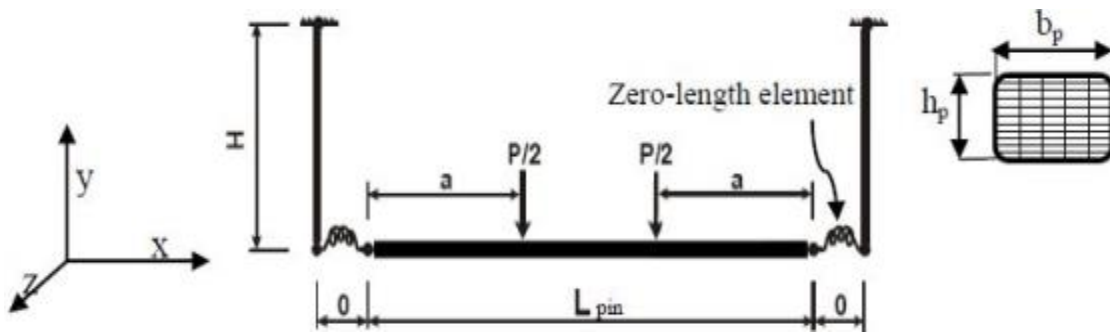


Figure 3.10: OpenSees beam model of single pin device

up of 60 fibres. Among them, 12 fibres are assigned along the height of the cross-section, h_p , and 5 along its width, b_p , as illustrated in Figure 3.10.

The length of the pin, L_{pin} , is the clear span between the outer-plates, which acts as supports. Herein, the pin's supports (outer-plates) are modelled as rigid links of length H_{op} , which represents the free length. Theoretically, the deformation between the pin member and the support (rigid link) can be represented by translational springs acting in the direction of pin's length. When the pin member is deflected downward or upward, its length is subjected to shortening.

To simulate this behaviour, a zero-length element object that is defined between two nodes generated at the same location is added at both pin members' ends, as illustrated in Figure 3.10. These nodes of identical coordinates are connected by springs, with the aim to represent the force-deformation relationship exhibited by the pin in the outer-plate supports. The uniaxial material assigned to the pin member and rigid links is *Steel02*, which is also known as Giuffre-Menegotto-Pinto material. It is recommended that the steel strength of plates to be the same with that of the pin. Nonetheless, the length and thickness of the outer-plates influence the behaviour of the connection, while the deflection of the pin controls the transversal deflection of outer-plates. When the pin member behaves elastically, both links (outer-plates) act as cantilever members with a stiffness $K_{op} = 3EI_{op}/H_{op}^3$, where $E_{op}I_{op}$ is the flexural stiffness of the link. To simulate the non-linear behaviour of pin member in the outer-plate supports, two translational springs were added in the zero-length element, in the x -direction and one in the y -direction. Among them, one spring is made of *Steel02* material and others of *Pinching4* material that is defined in the OpenSees library (Mazzoni et al., 2006).

The *Pinching4* material represents a pinched force-deformation response and it allows users to simulate the deformed shape of the pin in the outer-plate's hole support after the pin member is loaded below its elastic bending capacity.

The OpenSees beam model was developed by using data from two experimental tests conducted at Technical University of Lisbon, and the employed specimens, PA-9 and P-3, are shown in Figure 3.11. The pin member considered in the experimental test has a solid rectangular shape with rounded corners and was mounted in the weak axis as illustrated in Figure 3.11. The difference between PA-9 and P-3 specimen is only the distance between the inner-plates. In both cases, the pin is made of steel with the following characteristics: $F_y = 396$ MPa and $F_u = 558$ MPa, while the pin's cross-sectional dimensions are 60x40 mm. The tri-linear curves of both specimens, PA-9 and P-3, are built by using the theoretical values computed with Equations 3.1 to 3.4 and are plotted in Figure 3.12.

To investigate the correlation between the theoretical tri-linear curve and that resulted from the OpenSees beam model, an incremental analysis is performed. Pairs of applied forces and deflections recorded under the point of loading are plotted in Figure 3.12 together with the theoretical tri-linear curve. In addition, at each incremental loading application, the strain and stress corresponding to each one of the 12 fibres is recorded at beam's mid-span of specimen P-A9 and is plotted in Figure 3.13 and respectively Figure 3.14. Thus, when both forces $P_y/2$ are applied to the OpenSees beam model, as illustrated in Figure 3.6, the strain recorded in the extreme fibres of the mid-span cross-section is ϵ_y and the associated stress is F_y . By using the geometry of P-A9 specimen, the force P_y computed with Equation 3.2 is 145kN. As depicted in

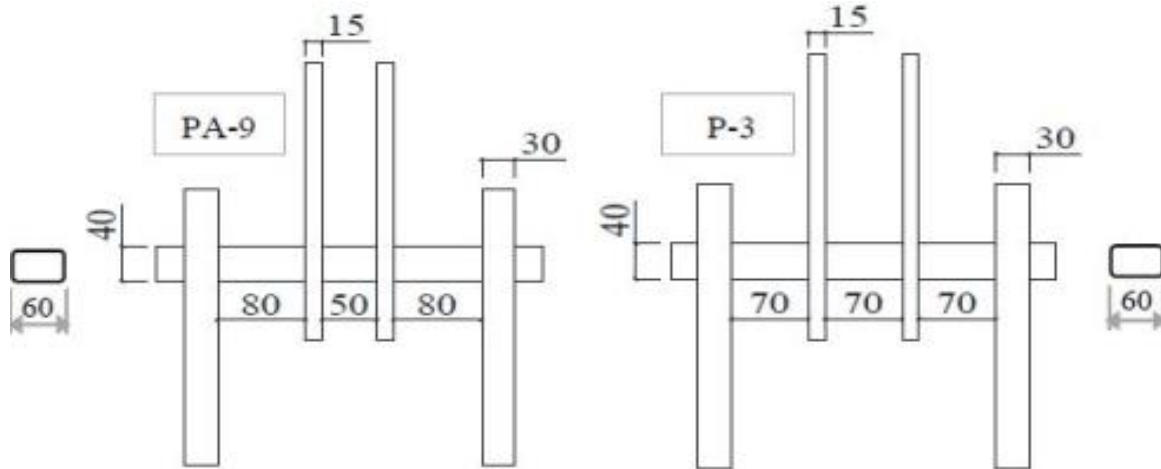


Figure 3.11. The geometry of tested specimens PA-9 and P-3

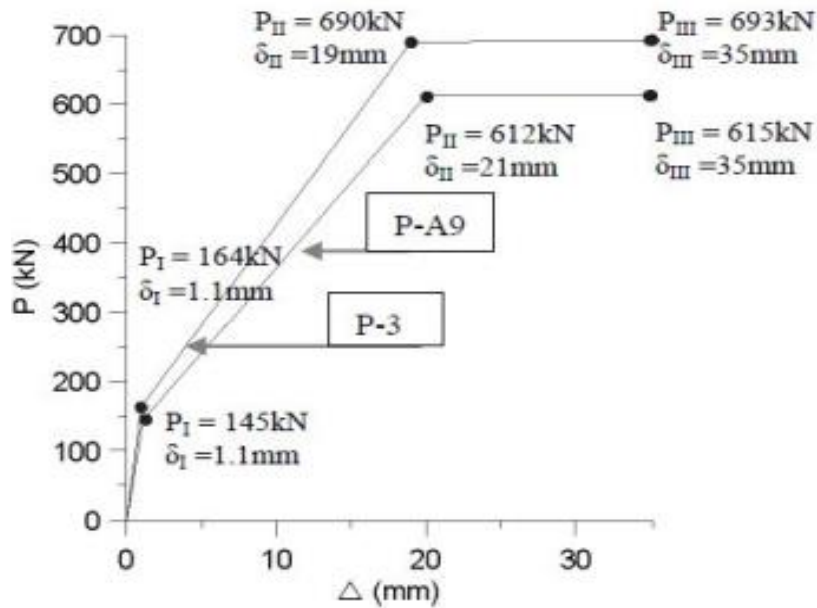


Figure 3.12. Theoretical tri-linear curve of the PA-9 and P3 connection devices

Figures 3.13 and 3.14 , under P_{II} forces, the numerical model shows a slight difference in strain and stress recorded at the extreme tension and compression fibre of the pin's mid-span length. Herein, the strain in the tensile fibres is about 12% larger than that in compression fibres, while the variation of stresses in fibres is between F_y and F_u .

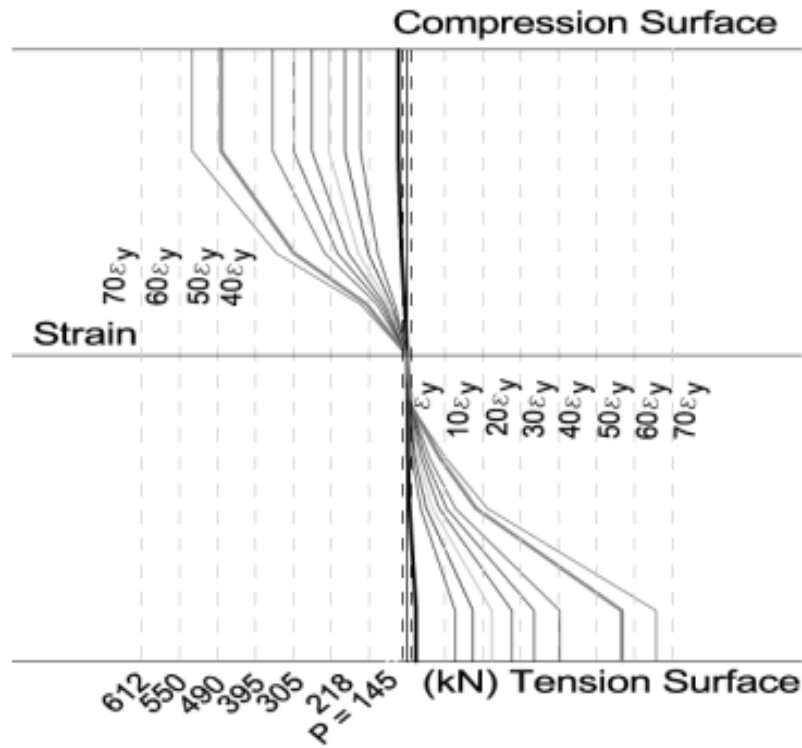


Figure 3.13. Strain along PA-9 pin's height recorded at midspan

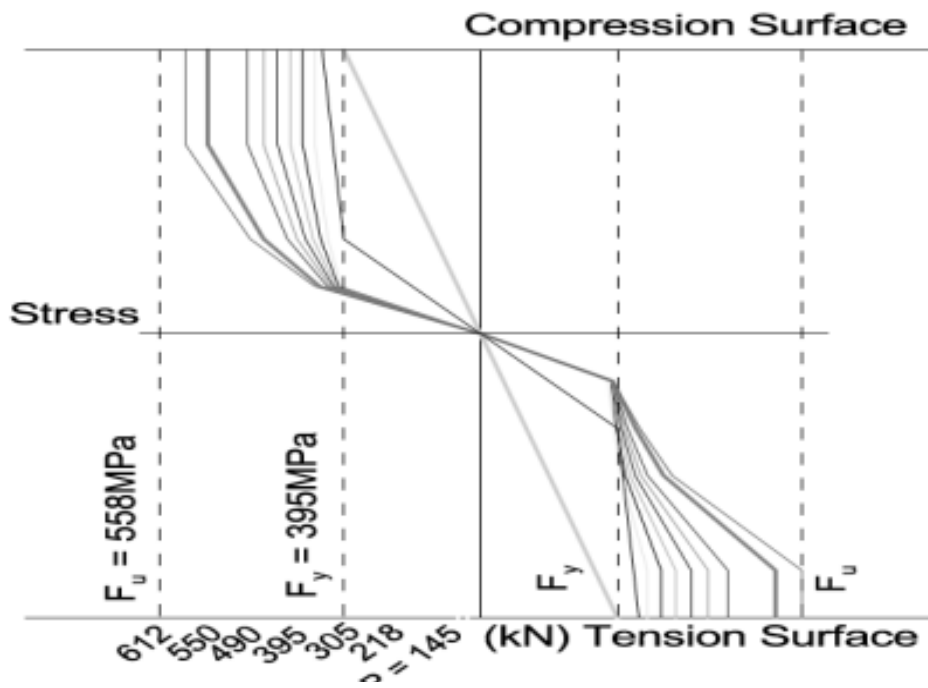


Figure 3.14. Stress along PA-9 pin's height recorded at midspan

Thus, the analytical and the OpenSees beam models show a good correlation and the stress and strain diagrams validate the theoretical equations previously devised.

To analyze the propagation of plasticity along the pin’s length under incremented static loads, the strain time-history series that are developed in the extreme fibres are investigated. In this numerical model, the pin member is divided in eight force-based beam-column elements, rigidly connected, as illustrated in Figure 3.15. These beam-column elements are made of cross-sections based on fibre formulation, while the depth of pin’s cross-section is divided in 12 fibres, in conformity with Figure 3.10. Each fibre made of *Steel02* material is defined by an area and a location (x, y). As shown in Figure 3.15, four Gauss-Lobatto integration points are placed along each element and the force-deformation response at each integration point is recorded at the defined section.

To define the length of the developed plastic zone exhibited by the pin member, the values corresponding to the strain – deflection curve are recorded at the upper and lower fibre (1 and 12, respectively) of sections belonging to the integration points of elements number 3 and 4 (Figure 3.15). As shown in Figure 3.16, when the applied force increases above the elastic range, the portion of the pin between the inner-plates deforms in the non-linear range under the developed constant bending moment.

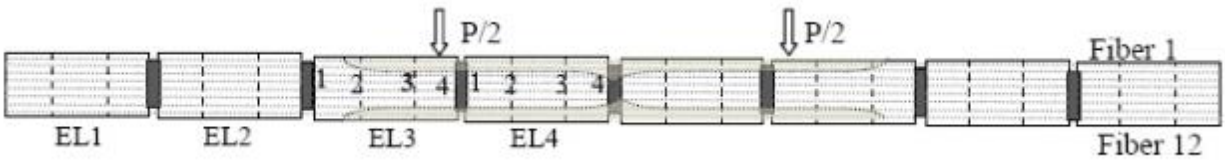


Figure 3.15. Numerical modeling of the PA-9 specimen; Schematic representation of pin member in OpenSees

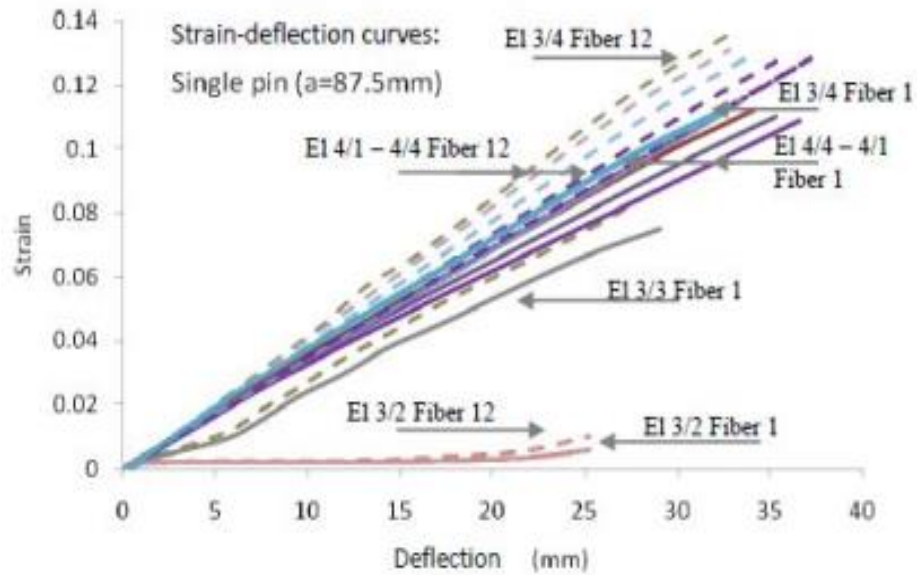


Figure 3.16. Strain-deflection curves of pin PA-9

The larger deformation is recorded at the pin's mid-span, while the larger strain is recorded at the location of inner-plates. Fibre 12 belonging to the tension surface shows a slightly larger strain than fibre 1, located at the compression surface. This difference increases with the magnitude of applied forces. For the modeled PA-9 specimen, the strain-deflection curves of extreme fibres located between the inner-plates show a linear relationship. In this example, the left inner-plate intersects the pin member in the vicinity of section 4 of element 3. For the half-length pin, it is observed that the plastic region length ends close to section 2 of element 3, which corresponds to a distance of $h_p/2$ measured from the inner-plate, where h_p is the depth of the pin member. As illustrated in Figure 3.16, the maximum deflection at pin's mid-span is 36 mm. Similarly, Figure 3.17 illustrates the strain and stress diagram of the P-3 specimen model that is measured in each one of the 12 fibres located at the pin's mid-span.

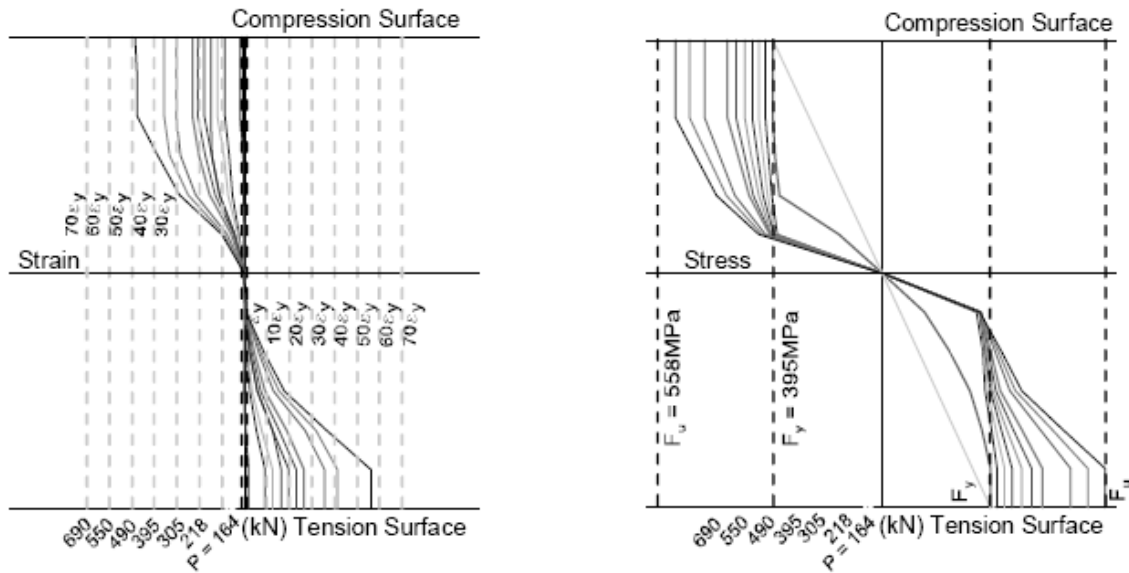


Figure 3.17. Strain and stress of pin P-3 recorded over the pin's height and at its mid-span length

The difference between the P-3 and PA-9 specimens was set by distance **a**, which in case of P-3 was reduced by 13%. Thus, the pin of the P-3 specimen is able to transfer a force that is 113% larger (690 kN versus 612kN), while exhibiting lower strain. As depicted in Figure 3.17, the strain recorded in the extreme fibres at the pin's mid-span length displays values that are lower by 13%.

A schematic representation of the pin member of the P-3 specimen model is shown in Figure 3.18 and the time-history series of strain-deflection curves of the extreme tension and compression fibres (12 and 1) are depicted in Figure 3.19.

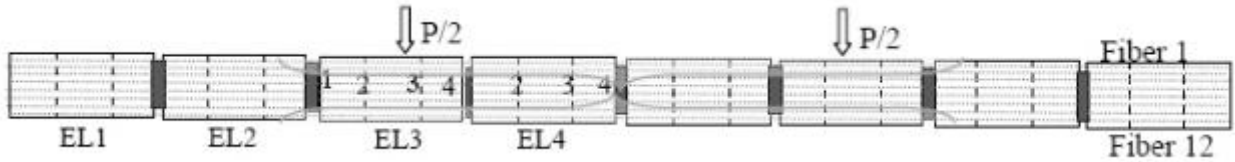


Figure 3.18. Numerical modelling of the P-3 specimen; Schematic representation of the pin member in OpenSees

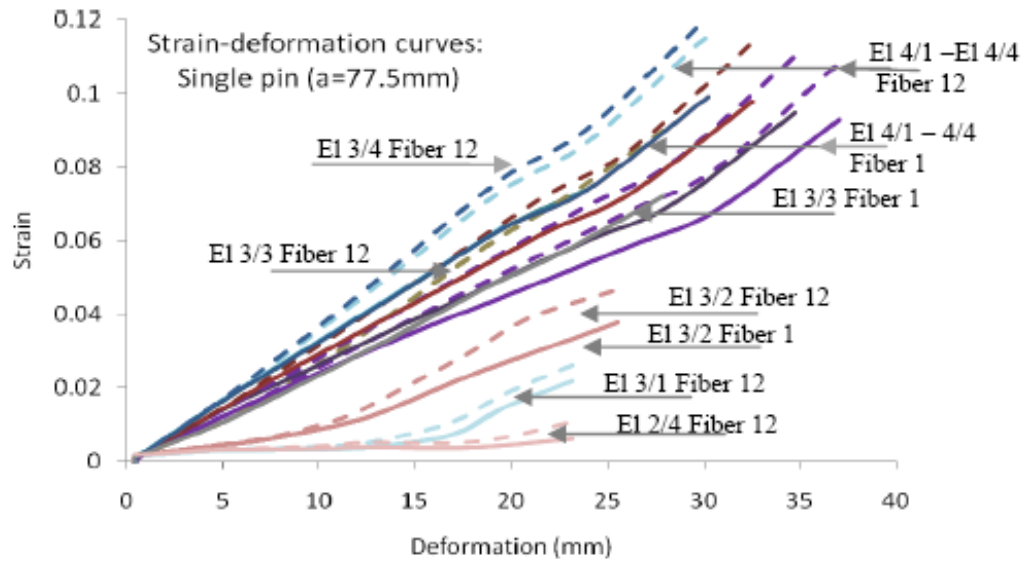


Figure 3.19. Strain-deflection curves of P-3 specimen

In the case of P-3 specimen model, the strain-deflection curves show a weaving behaviour with a sharp increasing in strain for forces larger than 612 kN. The maximum strain is experienced by fibre 12 of element 3, section 4, located in vicinity of inner-plate. It displays a deformation of 20 mm for a tensile strain of 0.08 or $40\epsilon_y$ and 30 mm at failure when the associated strain is about 0.12. In comparison with the PA-9 pin model, the fibre 12 of element 3, section 4 of both pin specimens experienced the same strain for a 20 mm deflection, but at the state of failure, the corresponded strain and deflection value experienced by the same fibre of pin

P-3 has dropped by 13%. In addition, by comparing the tensile and compression strain recorded at pin's mid-span (fibres 12 and 1 of element 4, section 4) the P-3 pin developed lower strain values (Figure 3.19).

The difference in behaviour is due to a/L_{pin} ratio. In the case of P-3 specimen, $a/L_{pin} = 0.323$ where $a = 77.5$ mm and $L_{pin} = 240$ mm. By considering the pin and outer-plate cross sections 60×40 mm and 180×30 mm, respectively, the computed pin-to-outer-plate stiffness ratio is $(I_{pin}/L_{pin})/(I_{op}/H_{op}) = 0.5$, where $I_{pin} = 60 \times 40^3/12$, $I_{op} = 180 \times 30^3/12$ and $H_{op} = 150$ mm. When the point of applied force moves toward the middle of the pin (PA-9 specimen), slightly larger outer-plate stiffness is required to sustain the same applied force. In the case of PA-9, $a = 87.5$ mm, $a/L_{pin} = 0.365$ and the change in the a/L_{pin} ratio with respect to the previous case is 113% (e.g., $0.365/0.323 = 1.13$). As noted above, the ratio between the maximum force carried by P-3 specimen and PA-9 specimen is 1.13 (692 kN versus 612 kN). In addition, from previous studies (Vayas & Thanopoulos, 2005) it was found that clamping effect increases until the thickness of outer-plates reaches $0.75h_p$.

In the nonlinear range, axial compression force is developed in addition to bending moment which magnitude is slightly larger at pin's mid-span than at its support. The compression force developed between the inner-plates is smaller than that developed between the inner-plate and outer-plate due to the tangential component of applied load that acts in opposite direction. Failure of pin occurs under the combined effect of axial force and bending moment. From data collected for both specimens P-3 and PA-9 it was found that the normalized bending moment component has the largest weight in the interaction equation while the normalized axial force component is less than 10% in the mid-span segment and less than 15% at pin's support.

To summarize, the behaviour of pin member is influenced by the distance between the inner- and outer-plate that is expressed by parameter a , as well as by the dimensions of outer-plates. When the distance between inner-plates ($L_{pin} - 2a$) increases (e.g. P-3 specimen vs. PA-9), the portion of pin that is subjected to plastic deformation expands across the pin's length, while the maximum strain decreases. From numerical computations, the length of plastic hinge developed over the pin member is approximated as being: $(L_{pin} - 2a + h_p)$. However, both PA-9 and P-3 pins experience the same deflection at the mid-span length and display larger strain in tension than in compression. The OpenSees beam model was used to emphasise the distribution of strain and stress across the pin's length.

3.4 Validation of the OpenSees Model of P-A9 and P-3 Joints vs. Experimental Test Results

The two selected specimens PA-9 and P-3 were tested on a box stand under the ECCS cyclic quasi-static loading protocol (Technical Committee - Structural safety and loading, 1986).

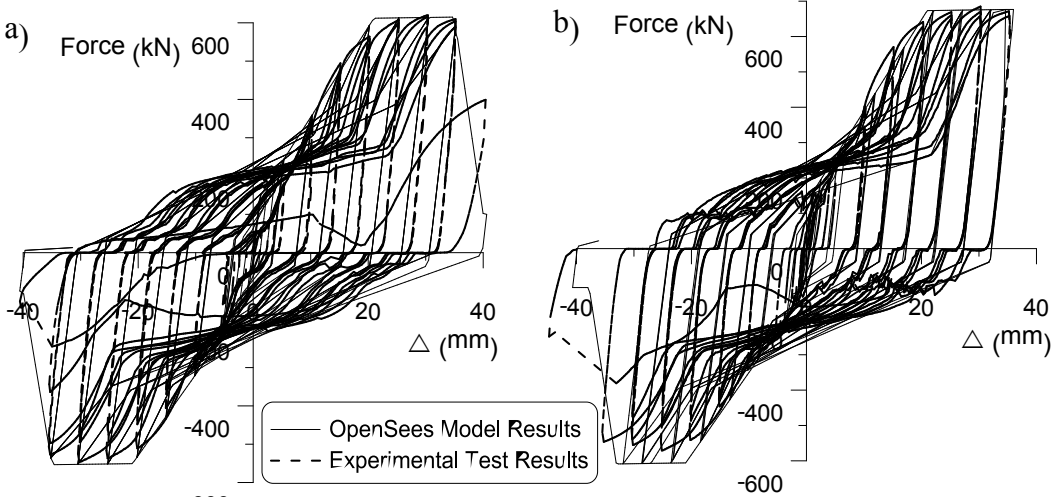


Figure 3.20, Hysteresis loops as per the OpenSees model vs. experimental test
a) PA-9 and b) P-3

The displacement loading applied to the PA-9 sample has 25 cycles with a rate of loading of 0.45 mm/s and a maximum displacement in the last cycle of 40 mm. The displacement loading protocol applied to the P-3 sample has 21 cycles, a rate of loading 0.33 mm/s and a maximum displacement of 45 mm. In both cases, three consecutive cycles reaching the same displacement amplitude were considered. The force-displacement hysteresis loops that characterize the behaviour of specimens PA-9 and P-3 are shown in Figure 3.20.

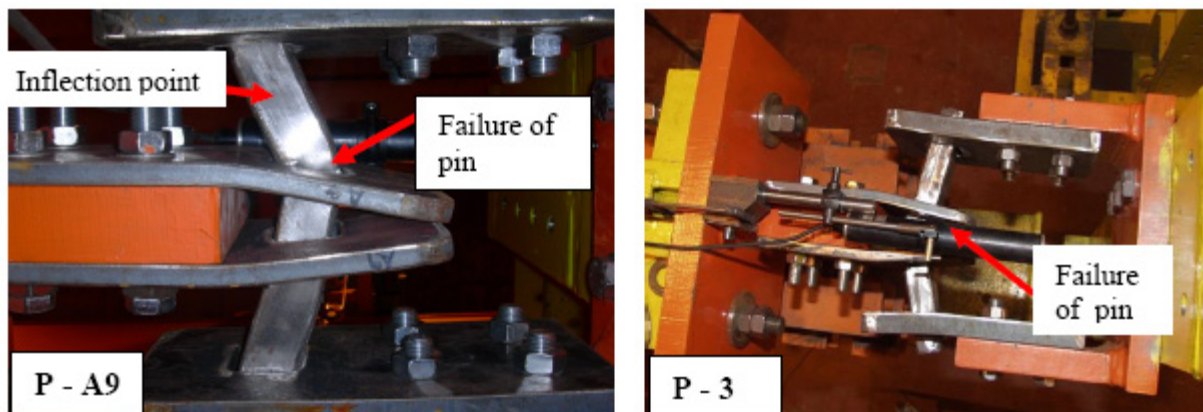


Figure 3.21. Failure mechanism of specimens PA-9 and P-3 (Calado, 2004)

In both cases, the failure of the pin occurred at one of the two points of load application, when it is reloaded in tension (Plumier, et al., 2006), as illustrated in Figure 3.21. Thus, in the case of specimen PA-9, when the distance between the outer- and inner-plate is larger than the distance between inner-plates, the failure occurs in the longer pin segment, at the external face of the inner-plate. In the case of specimen P-3, the failure occurred in the middle segment at the internal face of the inner-plate. For both specimens, the same stiffness degradation occurred during reloading. Although both specimens reached approximately the same magnitude of maximum deformation in bending, 37 mm, the corresponding ultimate tensile forces of PA-9

(615 kN) is lower than that recorded for P-3 (694 kN). On the other hand, for both specimens, the capacity in tension is larger than that in compression by 13%. This difference in strength is due to the out-of-plane bending of outer-plates, which implies an increased distance between the pin's supports in the outer-plate hole. In this case, the outer-plates deflect toward the exterior, as is shown in Figure 3.21. As a result, the stiffness and the thickness of outer-plates influence the behaviour of pin connection. As discussed above, it is recommended that the stiffness of the outer-plate to be two times larger than the stiffness of the pin and $t_{op} \geq 0.75h_p$.

The purpose of developing the OpenSees model for pin connections is to study the behaviour of CBFs equipped with pin devices placed in-line with brace members. In this light, the rigid link (outer-plates) is fixed to the column at the location of column-to-beam joint and is connected by means of zero-length element to brace member. *Pinching4* material is assigned to translational springs and was employed in this study with the aim of simulating the changes in pin member behaviour, while undergoing different degrees of fixity when changing from a pinned to a clamped support. To simulate the hysteretic response of specimens P-3 and PA-9, the unloading stiffness degradation model for a hardening-type response envelope is used and calibrated against experimental test results.

The hysteresis shape defined by the *Pinching4* uniaxial material model is illustrated in Figure 3.22 and it corresponds to that provided in the OpenSees manual (Mazzoni et al., 2006). The coordinates of force-deformation corresponding to a hardening-type response envelope are those computed for the tri-linear curve (e.g., Figure 3.12) and are depicted in Figure 3.22: (ePf1, ePd1), (ePf2, ePd2) and (ePf3, ePd3). However, the hysteresis shape may not be symmetric when the outer-plates behave in tension or compression as shown in Figure 3.20. To define pinching, three additional floating points (rForceP•ePf3, rDispP•ePd3 and uForceP•ePf3) are required to be

identified in tension and three in compression. Points involving these coordinates are symbolized with “X” in Figure 3.22. For example, in the case of PA-9 specimen depicted in Figure 3.20 a), the floating point $rForceP \cdot ePf_3$ represents the ratio of the force at which reloading occurs, 291 kN, to the total hysteretic force demand, 615 kN. Similarly, the second floating point $rDispP \cdot ePd_3$ represents the ratio of displacement where reloading begins, 24 mm, to the total hysteretic displacement demand, 37 mm. In this light, the computed ratios are 0.47 and 0.65, respectively. The third floating point $uForceP \cdot ePf_3$ is the ratio of force at negative unloading, 17 kN, to the total load during monotonic testing, 615 kN, resulting in a value of 0.03. Therefore as is shown above, the pinching envelope is built by multiplying certain values of the skeleton curve, better known as the tri-linear curve, with the above floating point values, defined for the tension side. For the compressive side, the floating points are reported to a total compressive force of 549 kN.

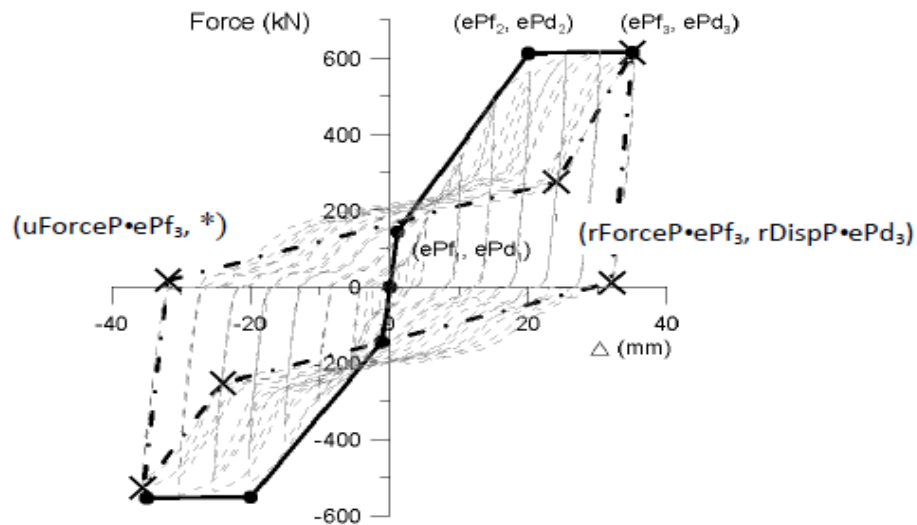


Figure 3.22. Pinching4 material definition

To validate the OpenSees pin model that is simulated for specimens PA-9 and P-3, the normalized cumulative energy, $E/P_y\delta_y$, illustrated in Figure 3.23, is computed as the summation of the normalized energy dissipated per cycle, $E_{cycle}/P_y\delta_y$. Herein, the energy dissipated per cycle is calculated as the area enclosed by the associated cycle over the energy at yield, $P_y\delta_y$. The difference between the numerical model and physical test increases significantly for the last cycle prior failure. The hysteresis response of both specimens shows the occurrence of failure when the specimen is reloaded in tension.

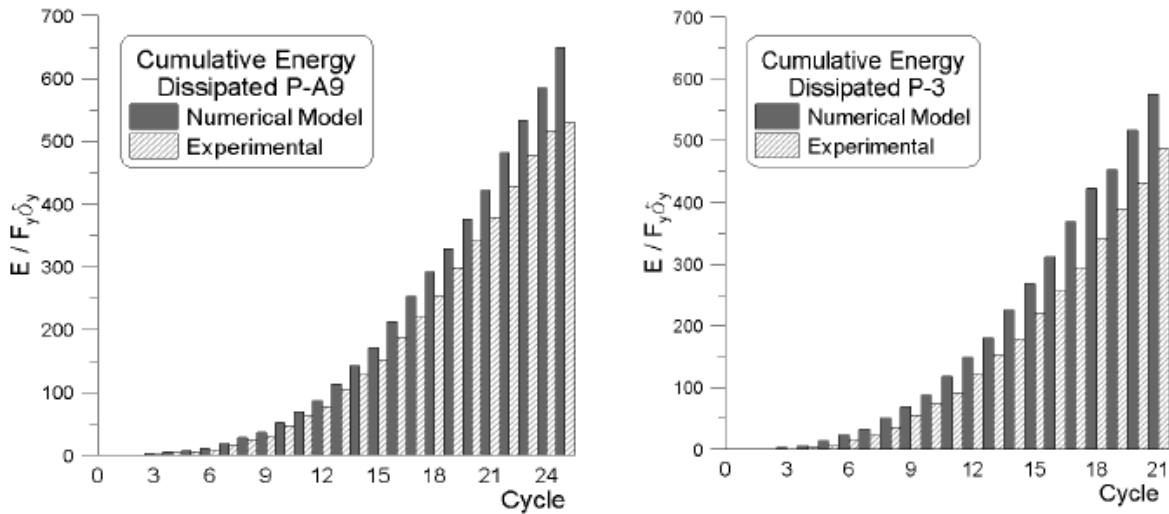


Figure 3.23. Normalized cumulative dissipated energy of numerical model vs. physical test: PA-9 and P-3 specimens

Thus, the OpenSees model is able to replicate the global behaviour of single-pin connection. The P-3 specimen was subjected to 21 cycles, while the PA-9 specimen to 25 cycles. To summarize, under similar conditions (equal number of cycles), the single-pin connection with larger distance between inner-plates possesses a larger dissipative energy capacity.

3.5 Numerical Modelling of Double-Pin Connection Device

To transfer large axial force triggered in brace members to brace-column connections, the capacity of the single-pin device may not satisfy the demand. For this case, the double-pin connection device with pins displaced either in-parallel (Figure 3.3) or in-line (Figure 3.4) are proposed. The double-pin connection is analyzed through numerical models by following the same approach that was used for the single-pin. In this study, only the case with a larger outer-to inner-plate distance is considered ($a = 87.5$ mm). For comparison purposes, two small pins of rectangular shape 40x35 mm that possess an equivalent flexural stiffness with that of single-pin 60x40 mm are selected for investigations.

3.5.1 Modelling and behaviour of double-pin connection with pins placed in-parallel

As illustrated in Figure 3.3, the double-pin connection with pins placed in-parallel (DP-PP) has a symmetrical geometry. Due to its symmetry, the study can be conducted for half of the device and its behaviour is expected to be similar with that for a single-pin. Thus, each pin must be proportioned to carry half of the force triggered in the brace, while undergoing the same deflection that is expected to be experienced by an equivalent single-pin device. In this example, the same geometry of pin's length, outer- and inner-plates as that illustrated for the specimen PA-9 are considered and used in the single-pin OpenSees beam model depicted in Figure 3.10. The theoretical tri-linear curve computed for each pin displaced in-parallel may be plotted similarly with that developed for a single-pin. The tri-linear curve and three-dimensional model of the DP-PP connection are illustrated in Figure 3.24. The strain and stress diagram corresponding to each one of the two pins subjected to incremental static loading is shown in Figure 3.25.

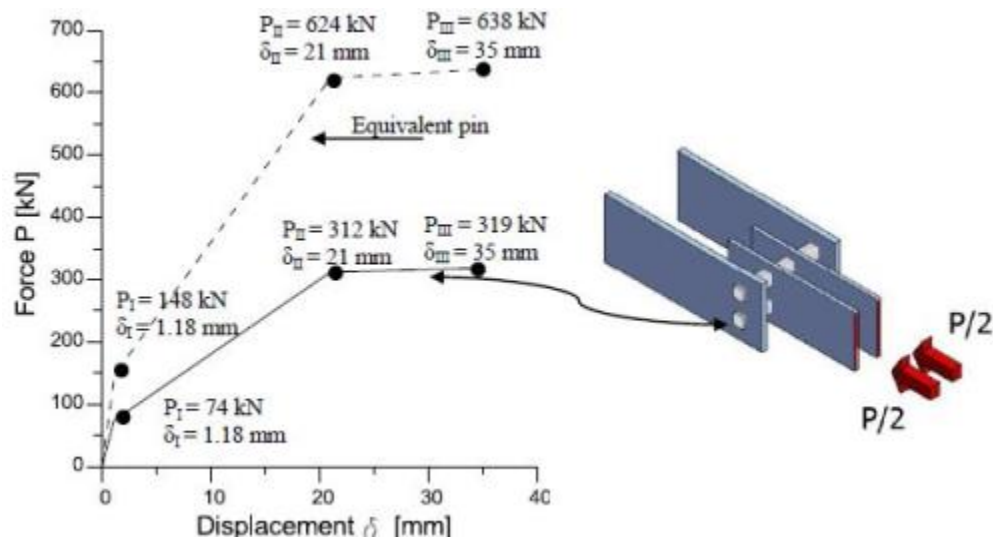


Figure 3.24. DP-PP connection: Tri-linear curve and 3D Model

Data in Figure 3.25 was recorded for each one of the 12 fibres (Figure 3.10) that represent the pin's cross-section located at pin's mid-span length.

From Figure 3.25, it is observed that slightly larger strain is developed in tension than compression upon failure. The values of strain and stress, recorded for one of the two pins when subjected to half of the force applied to PA-9 specimen, show almost the same values with those plotted in Figure 3.13 and Figure 3.14. The 40x35 pin member is subdivided in 8 elements as depicted in Figure 3.15. Similarities in the strain-deformation time-history series depicted for the 40x35 pin and shown in Figure 3.26 were also observed.

As illustrated, the maximum strain is recorded in the extreme tensile fibre (fibre 12) at the location of section 4 that belongs to element 3. In addition, the length of plastic region is similar with that illustrated for PA-9 pin model, while the time-history strain-deformation curves show a linear relationship for fibres located between the inner-plates. Thus, by doubling the pin member,

the load-carrying capacity of connection increases two times, while the deflection remains the same as that experienced by an equivalent single-pin device.

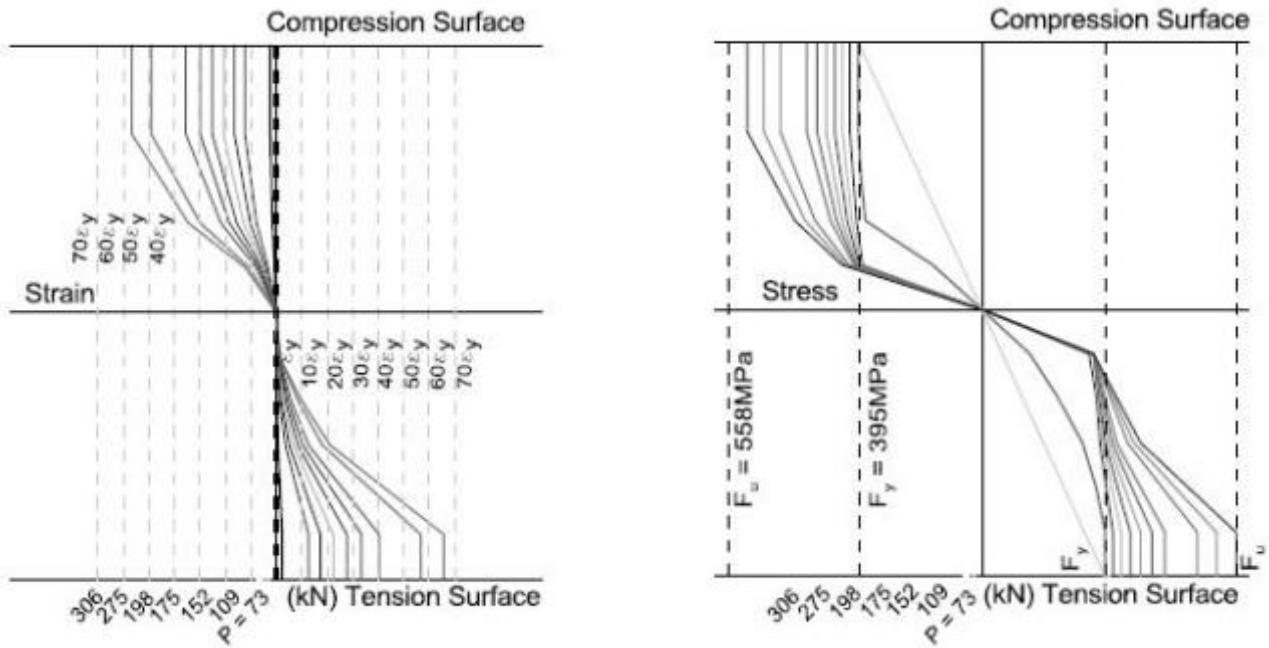


Figure 3.25. Stress and strain diagram of one of the two pins placed in-parallel and recorded at pin's mid-span length

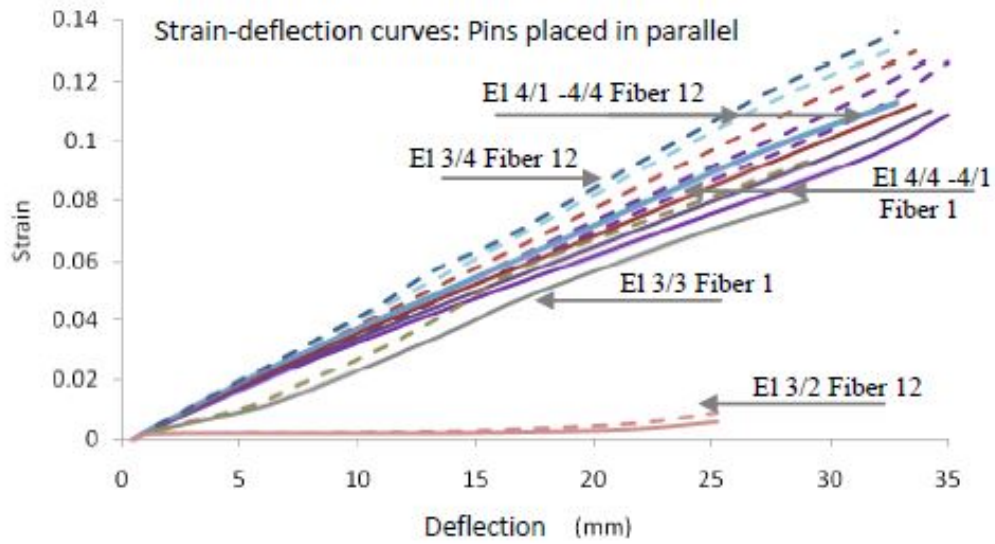


Figure 3.26. Strain deflection curves for one of the two pins placed in-parallel

3.5.2 Modelling and behaviour of double-pin device placed in-line

The three-dimensional scheme of double-pin connection with pins placed in-line (DP-PL) is shown in Figure 3.27 and the OpenSees model is illustrated in Figure 3.28.

Each one of the two pins is composed of 8 force-based beam-column elements with spread plasticity along the member length as depicted in Figure 3.15. Pins cross-sections are made of 60 fibres distributed as illustrated in Figure 3.10. *Steel02* material was assigned to all fibres. A zero-length element is placed at each pin ends in order to simulate the complexity of pin's support in the outer-plate hole. In addition, zero-length elements are placed at the connection between pin members and inner-plates. Through design, the pin members of the DP-PL connection are assumed to dissipate energy in flexure, while the remaining components such as the outer- and inner-plates behave elastically. Due to the large stiffness of the inner-plate in the plane of loading, both pins are subjected to equal deformation, while the system composed of two pins connected by the two inner-plates behaves as an equivalent W-shape beam where both flanges are supported in the four outer-plates holes. In this example, the distance between the centerline of the two pins is $2.5h_p$ (100mm) and it can be increased to $3h_p$, the thickness of the outer-plates is 30 mm ($t_{op} \geq 0.75h_p$), while that of inner-plate is 20 mm ($t_{ip} \geq 0.5h_p$). The net area of outer-plate across the pin hole, normal to the axis of the member, shall be at least 1.33 times the cross-sectional area of the pin member. In the same time, the distance from the edge of the pin hole to the edge of the outer-plate member, measured transverse to the axis of the member, shall not exceed four times the thickness of the material at the pin hole (e.g., the width of outer-plate is $b_{op}=180mm$ and $(180-40)/2 \leq 4t_{op}$ where $t_{op}=30 mm$). This verification is applied to inner-plates as well (e.g., for $b_{ip}=180mm$ it results $(180-40)/2 \leq 4t_{ip}$ where $t_{ip} = 20 mm$).

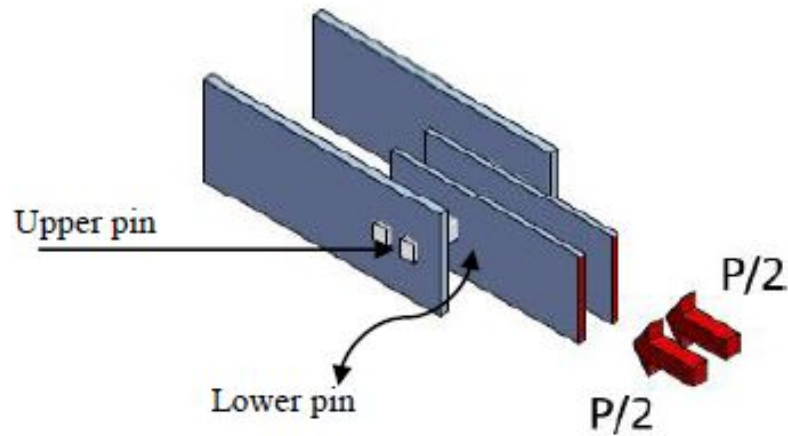


Figure 3.27. 3D scheme of double-pin connection device with pins placed in-line

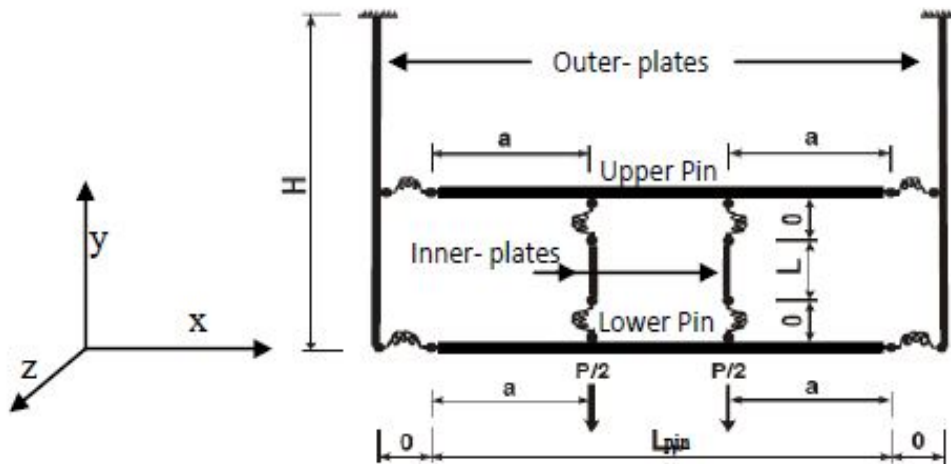


Figure 3.28. The OpenSees model of double-pin connection with pins placed in-line

To simulate the connection between the pin member and the outer-plate support, three translational and one torsional spring are assigned in the zero-length element illustrated in Figure 3.28.

Among them, two translational springs are placed in the x -direction and one in the y -direction, while the torsional spring assures that no twist occurs in the z -axis. One of the two translational springs, made of *Steel02* material and assigned in the x -direction, simulates the

effect of the outer-plate. The second translational spring, assigned in the x -direction, is made of *Pinching4* material and represents the pinched force-deformation relationship that controls the pin behaviour. On the other hand, between the inner-plate and the pin member is a pinned connection that is simulated by two translational and one torsional spring, assigned in the zero-length element. Among the two translational springs, made of *Steel02* material, one is placed in the x - and the other in the y -direction, while the torsional spring is added to restrain torsion about z .

However, there is a difference in the development of strain in the plastic range of the upper and the lower pin. When pins deflect in-plane, they engage the outer-plates to bend toward interior, whereas the outer-plates are rigidly connected to column flanges. In addition, the deformation of the two pins is controlled by the force-deformation relationship exhibited by the inner-plates in the process of transferring the axial force from the brace to the column.

Thus, the two pins experience equal deformation in bending, although the pin located toward the brace (lower pin) is subjected to larger stress and strain than that on the above (upper pin), as shown in Figure 3.29. In this light, the maximum strain that is developed in the lower pin is about $40\varepsilon_y$ in both tension and compression. This maximum strain value is smaller than that shown for the same pin's size displaced in-parallel (Figure 3.25). To summarize, dissipative connection with pins in-line shows lower demand in strains and stresses than the equivalent connection with pins in-parallel, while carrying the same magnitude of forces.

To analyze the undergoing deformation of the pin members, the time-history series of strain-deformation of the extreme pin's fibres is plotted in Figure 3.30. Herein, the maximum tensile strain recorded in fibre 12 of element 4, section 4 (mid-span length) of the upper pin is 0.06 versus 0.072 of the lower pin. However, for the same section location, the maximum

compressive strain developed in fibre 1 of the lower pin is double than that developed in the upper pin. Meanwhile, the lower pin shows a linear strain-deformation relationship, while the upper pin shows a parabolic relationship. Each pin is made of eight non-linear beam-column elements as illustrated in Figure 3.15. The length of the plastic region is similar with that illustrated in Figure 3.26, while the maximum bending deformation is slightly reduced.

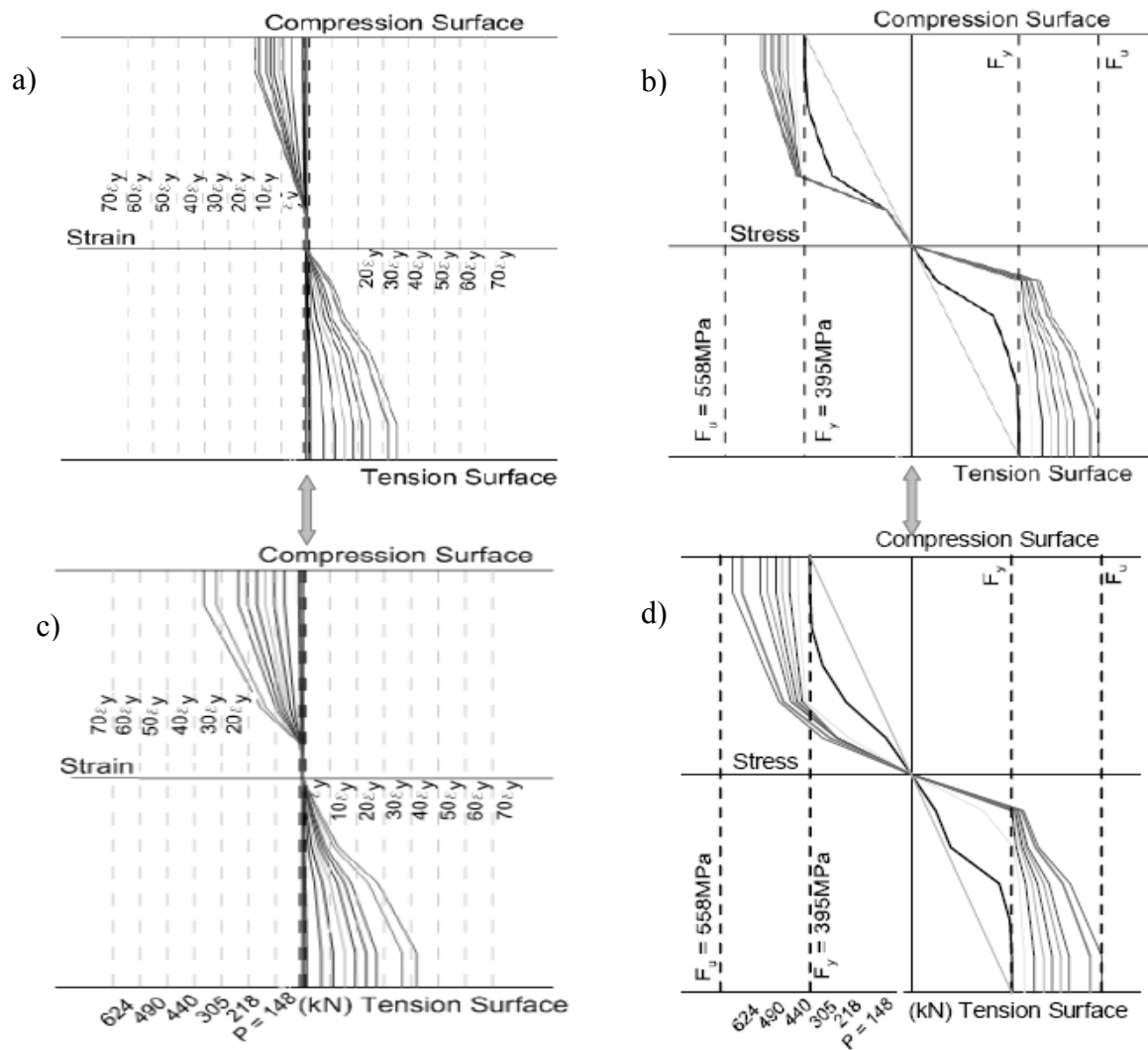


Figure 3.29. Stress and strain diagram of pins placed in-line, recorded at pins mid-span length
a) strain of upper pin, b) stress of upper pin, c) strain of lower pin, d) stress of lower pin.

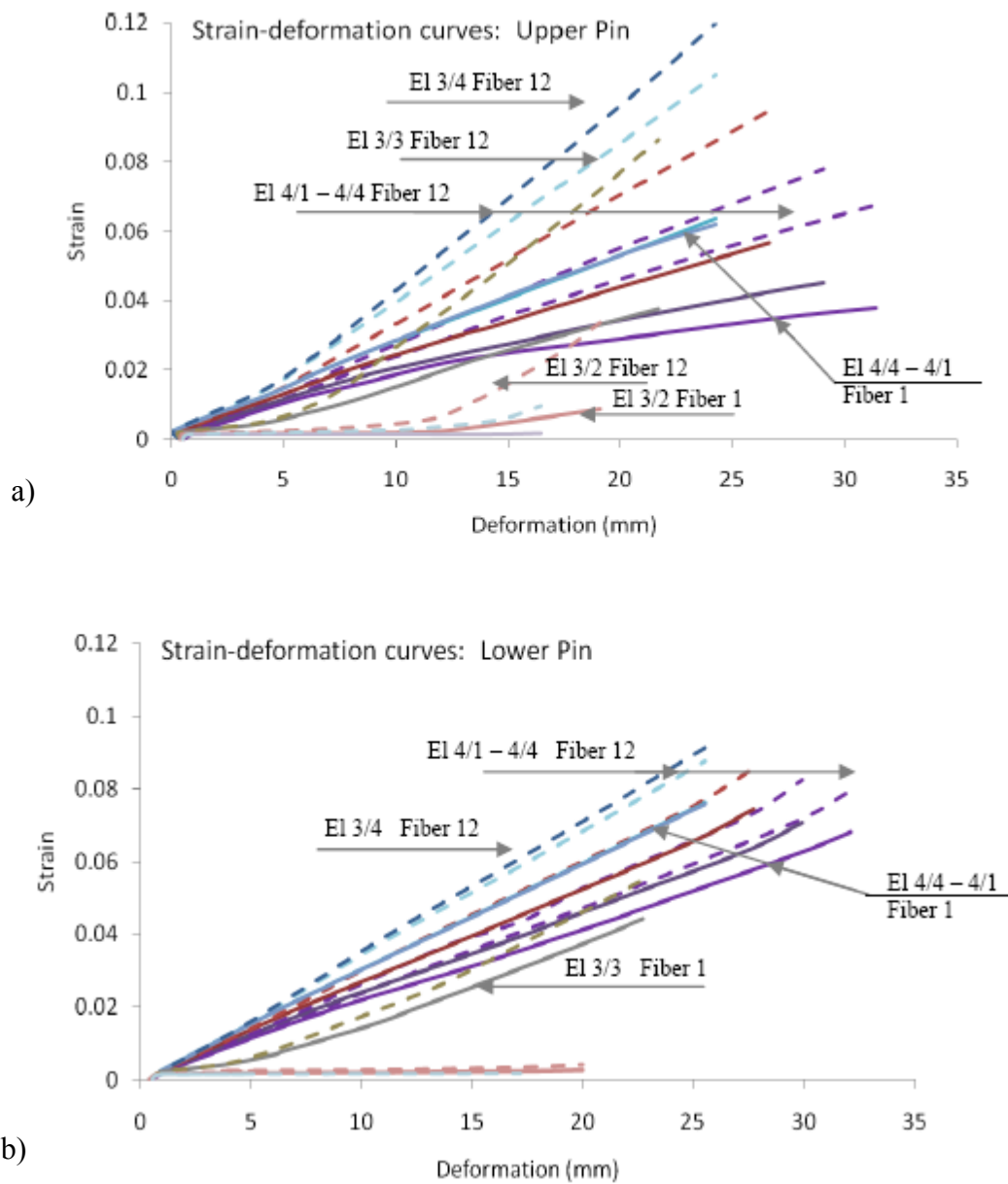


Figure 3.30. Strain deflection curves of both pins placed in-line: a) upper pin, b) lower pin.

Chapter 4. Design and Behaviour of Concentrically Braced Frame in X-Bracing Configuration

4.1 Design of 4-Storey Concentrically Braced Frame in X-Bracing Configuration

The purpose of the previous chapter was to evaluate the behaviour of pin connections displayed in single and double configuration.

To compare the seismic response of structures with and without dissipative pin connections, in this chapter the behaviour of a low-rise CBF in X bracing configuration is presented and the results are obtained by using the OpenSees software (McKenna et al., 2009).

4.2 Building Description

The selected building, with type of occupancy office, is located in Victoria, BC, on Class C soil and its plan view and 2D frame elevation are shown in Figure 4.1 and Figure 4.2, respectively.

In order to design the CBF building, both gravity and seismic force resisting system are proportioned by using the National Building Code of Canada (NRCC, 2010) and the S16-2009 standards.

From specifications, if the structure is less than 60 m in height, the code allows to use the equivalent static force procedure in order to design the seismic force resisting system. In this light, the base shear force is computed by using Equation 4.1:

$$V = S(T_a)M_v I_E W / (R_d R_0) \quad (4.1)$$

The minimum and maximum base shear value is given in Equation 4.2 and Equation 4.3 respectively.

$$V_{min} = S(2.0)M_v I_E W / (R_d R_0) \quad (4.2)$$

$$V_{max} = 2S(0.2)M_v I_E W / (3R_d R_0) \quad (4.3)$$

The fundamental period of the 4-storey building T_a , is evaluated by employing Equation 4.4, where h_n is the total building height and is equal to 15.2 meters.

$$T_a = 0.025h_n \quad (4.4)$$

The value for the fundamental period of the 4-storey building is 0.38s. According to the code requirements, if a dynamic analysis is employed, the period of the structure may be estimated to $2T_a$ resulting 0.76s.

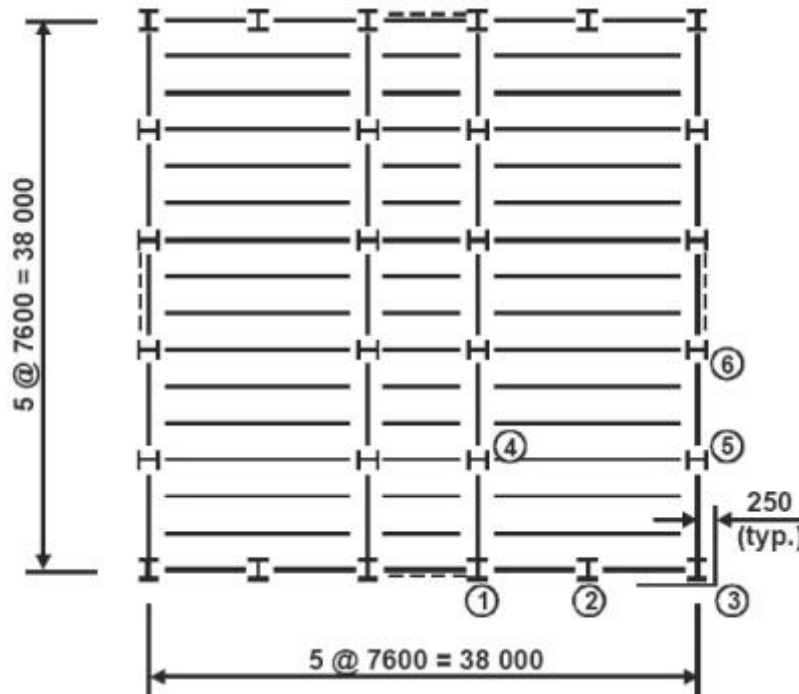


Figure 4.1. Plan view of the 4-storey building

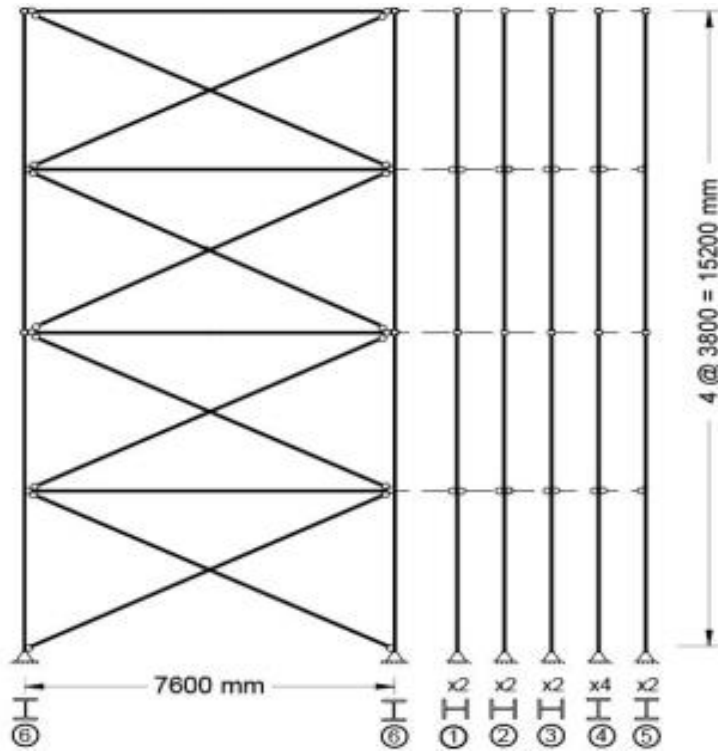


Figure 4.2. Elevation of the 4-storey CBF with participating gravity columns

The acceleration and velocity based site coefficients F_a and F_v are equal to 1 (NRCC, 2010). The design spectral response acceleration $S(T)$ is determined by using data from the uniform hazard spectrum computed from 2% probability of exceedence in 50 years. The $S(T)$ ordinates are given in Appendix "C" of the (NRCC, 2010) for the following period values: 0.2s, 0.5s, 1.0s and 2.0s. For 4.0s the value is half of that given for the 2.0s ordinate. These aforementioned spectral ordinates are given in Table 4.1 and the design spectrum is illustrated in Figure 4.3. By linear interpolation, the spectral ordinate corresponding to $T_a = 0.76s$ is: $S(T_a) = 0.59g$.

Table 4.1. Uniform hazard spectrum for Victoria, B.C

T(s)	0	0.2	0.5	1.0	2.0	4.0
Sa(g)	1.2	1.2	0.82	0.38	0.18	0.09

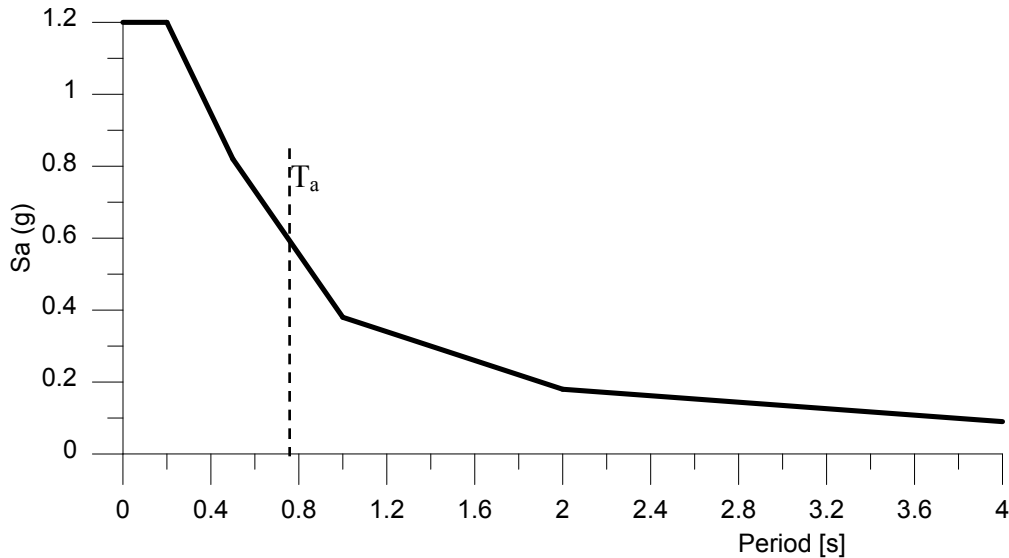


Figure 4.3. Design spectrum for Victoria, B.C

The importance factor I_E has been selected for an office building and is equal to the value of 1. The braced frame structure is classified as Moderately Ductile. The ductility related force modification factor is $R_d = 3.0$ and the overstrength related force modification factor is $R_0 = 1.3$. Herein, R_d is a factor that takes into regard the ability of the structure to dissipate energy and the over-strength force modification factor, R_0 takes into account the reserved strength from the members of the structure.

The specified gravity (dead, live and snow) loads are shown in Table 4.2.

Table 4.2. Building Loads

Roof	Dead Load	3.4 kPa
	Snow Load	1.48 kPa
Floor	Dead Load	5.0kPa
	Live Load	2.4 kPa
Exterior walls		1.2 kPa

The seismic weight per floor is composed of the weight of composite steel deck including partition walls, floor finishing, mechanical and ceiling, the weight of columns, cladding walls and the 25% of the snow load at the roof level. The total seismic weight of the building is 22683.8 kN. In Equation 4.1, M_v is the factor to account for higher mode effect on base shear and is related to the fundamental period of the building. For the 4-storey building $M_v = 1.0$. Thus, the base shear computed with Equation 4.1 is: $V = 0.59 \times 1.0 \times 22683.8 / (3 \times 1.3) = 3432$ kN. The resulted base shear is smaller than V_{max} computed as per Equation 4.3 and in consequence, the structural design is conducted for $V = 3432$ kN. As illustrated in Figure 4.1 there are two CBF systems in the N-S direction and two CBF systems in E-W direction. Thus, in each direction, each CBF system has to be designed to carry $3432/2 = 1716$ kN in addition to forces generated by P-delta effect and torsion.

To establish the sensitivity to torsion of the studied buildings, the ratio $B = \delta_{max}/\delta_{ave}$ must be computed in agreement with the NBCC 2010 provisions; where δ_{max} is the maximum storey displacement calculated at the extreme points of the building in the direction of the applied static lateral forces acting at distances of $\pm 0.1D_{nx}$ from the centers of mass at each floor, and D_{nx} is the dimension of the building perpendicular to the direction of the applied forces. Furthermore, δ_{ave} is the average storey displacement of these extreme points. For the cases $B > 1.7$, buildings are

considered as irregular. However, due to the symmetrical shape, the B ratio is less than 1.7 and therefore the building is not torsional sensitive. Due to building's symmetry, the center of mass coincides with the center of rigidity. Herein, for simplicity, the effect of accidental torsion was neglected.

The lateral forces distribution along the building height is established according to Equation 4.5 where W_x is given in Table 4.3:

$$F_x = (V - F_t) \frac{W_x h_x}{\sum_{i=1}^n W_i h_i} \quad (4.5)$$

By using the above equation, the distribution of forces per floor, as well as the shear forces are computed and given in Table 4.4. Because $T_a > 0.7s$, a concentrated force computed in agreement with NBCC 2010 provisions was considered.

Table 4.3. Seismic weight of the structure (total / frame)

Storey	h_x [m]	W_x [kN]
4	15.2	2853.1
3	11.4	6244.8
2	7.6	6789.5
1	3.8	6796.5
Total		22683.8

Table 4.4. Shear force distribution over the structure height

Storey	h_x [m]	V_x [kN]
4	15.2	918.4
3	11.4	2125.6
2	7.6	3000.7
1	3.8	3432
Total		3432

4.3 Members Design

4.3.1 Braces design

The following load combinations are considered for brace sizing: DL + 0.5*LL + E and 1.25*DL + 1.5*LL. Based on limit state design method, factored forces in member should be lower or at most equal to the member resistance. Thus, $C_f < C_r$ and $T_f < T_r$, where C_f and T_f are the factored compression and tension forces and C_r and T_r are the member resistance force in compression and tension, respectively.

The C_r and T_r values are calculated in accordance with Equations 4.6 and 4.7, respectively as per CSA/S16-2009.

$$C_r = 0.9 A F_y (1 + \lambda^{2n})^{-1/n} \quad (4.6)$$

$$T_r = 0.9 A F_y \quad (4.7)$$

where F_y is the yield stress of the steel, 350 MPa, and A is the cross-sectional area of the brace.

The computed slenderness is $\lambda = \frac{KL}{r} \sqrt{\frac{F_y}{\pi^2 E}}$, where r is the radius of gyration and L is the clear length of brace.

The slenderness ratio of all members, KL/r , and the width-to-thickness ratio have to be thoroughly checked. The end support conditions have to be taken into account when computing the KL value for compression brace members. The length L of the braces is the length between the end of brace that is welded to the gusset plates. In addition, for compression members, the ratio KL/r should be less than 200, while the selected HSS braces should be Class 1 sections. For X-bracing configuration, the tensile brace provides mid-span support to the compressive brace. In this light, in the computed slenderness ratio expression, half of brace length is considered. In conformity with clause 27.5.3.2 of S16-2009, the width-to-thickness ratio of HSS members shall not exceed $330/F_y^{0.5}$ for braces with $kL/r \leq 100$ and $420/F_y^{0.5}$ for braces with $kL/r = 200$. When $100 < kL/r < 200$ linear interpolation is used.

Braces were designed based on forces computed from the static equivalent method. For beams and columns design the effect of braces was considered.

4.3.2 SFRS Columns and Beams Design

The beams and columns of the seismic force resistant system (SFRF) are selected to be Class 1 sections and are made of W-shape cross-sections. Beams of CBFs in X-bracing configuration behave in bending under the gravity load combination $1.25*DL + 1.5*LL$ and in bending and axial compression under the $DL + 0.5*LL + E$ combination. For design, the following interaction equation is considered:

$$\frac{C_f}{C_r} + 0.85U_{1x} \frac{M_{fx}}{M_{rx}} \leq 1 \quad (4.8)$$

where C_r and M_r are the members' compressive and bending resistance, respectively; C_f and M_f are the factored compressive force and in-plane bending moment. In the case of seismic resistant

system, the width-to-thickness ratio limit for Class 1 sections in bending for W-shapes is $b/t \leq 145/F_y^{0.5}$.

The columns are considered continuum over two storeys.

The selected cross-sections for structural members such as: braces, beams and columns are given in Table 4.5 and are also depicted in Figure 4.4.

Table 4.5. Selected members for the 4-storey CBF frame

Storey	Braces	Beams	Columns
4	HSS 127 x 127 x 9.5	W 410 x 60	W 360 x 110
3	HSS 152 x 152 x 9.5	W 460 x 74	W 360 x 110
2	HSS 178 x 178 x 9.5	W 460 x 74	W 360 x 237
1	HSS 178 x 178 x 13.0	W 460 x 82	W 360 x 237

The behaviour of the structure studied has been designed through dynamic analysis by using the response spectrum method implemented in ETABS software and afterwards the numerical integration nonlinear time-history method implemented in the OpenSees software framework (McKenna, et al. 2009).

By using a 3D model developed in ETABS, the period of building in the first and second vibration mode in the direction of calculation was $T_1 = 0.816s$ and $T_2 = 0.21s$. As resulted, the fundamental period is very close to that considered in the hand calculation.

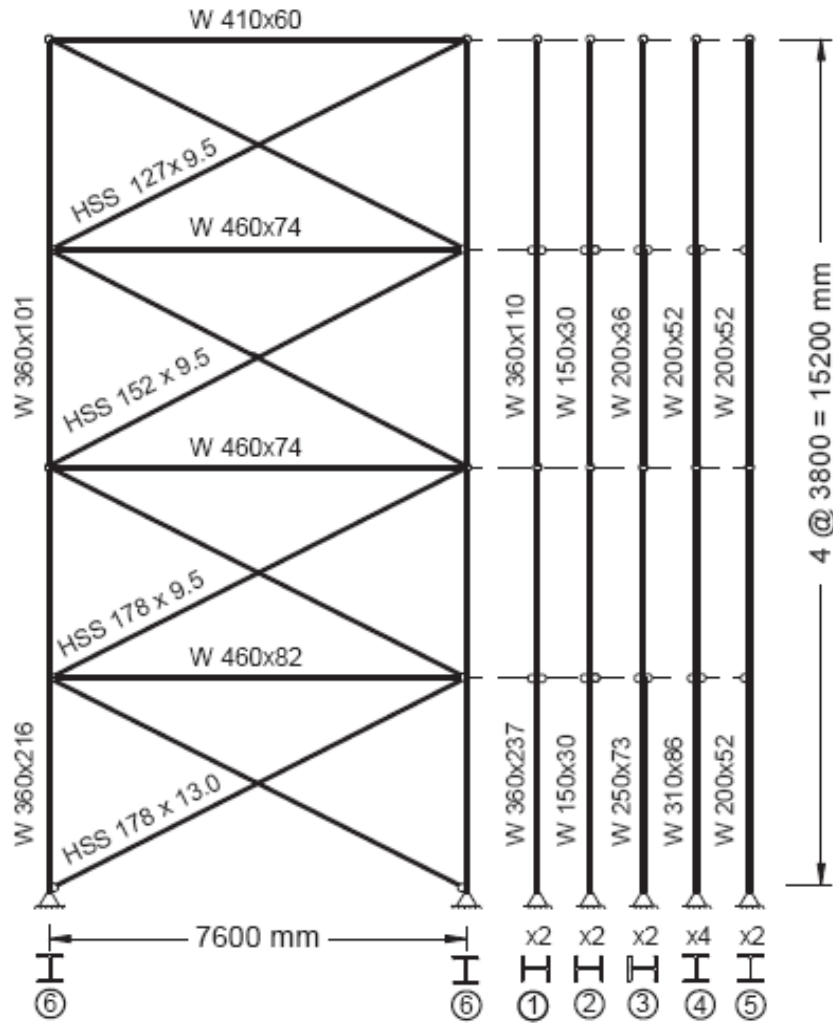


Figure 4.4. Members sizes of the 2D CBF with participating gravity columns

4.4 Modeling the 4-Storey CBF Building in OpenSees

The OpenSees software, version 2.3.2 was used to analyze the 4-storey structure.

4.4.1 The OpenSees framework

The OpenSees framework is an open source program developed at the University of California, Berkeley. The software framework is used for developing applications to simulate the performance of structure upon failure.

This software allows defining material non-linearity, elements, numerical algorithms and visualization inputs. The framework uses the TCL computer programming language to model, analyze and extract the output of the models built. This TCL language resembles closely to the C++ programming language.

The application input consists of simple defined texts on which the user has to define the elements, sections, nodes, load patterns, time series, materials and more factors that define the structure needed to be analyzed. The program uses a central domain to store the data provided by the definition of the model and outputs to an analysis module according to the recorder provided. The analysis application is time dependent and acts based on a translation from an initial time t_i to an incremented time ($t_i + dt$). The time for running the simulation is imposed by the user.

4.4.2 Modelling of beams and columns

The beams and columns selected for the structures are shown in Table 4.5. These members are modeled in OpenSees as force based nonlinear beam-column elements, while the *Steel02* material that is known as the Giuffrè-Menegotto-Pinto material was assigned. This type of uniaxial steel material with isotropic strain hardening allows the material to yield under developed strain while the cross-sections of the element is centered about its neutral axis.

The material definition input requires the elastic modulus, $E = 200\text{GPA}$ and the yield stress of the steel, $F_y = 350\text{MPa}$ to be inserted. The element contains a series of parameters that control the transition of the steel material from an elastic range to a plastic one as well as isotropic strain hardening values. As seen in Figure 4.5, the material behaviour is different for each selected R value (e.g., R equal to 5 and 20).

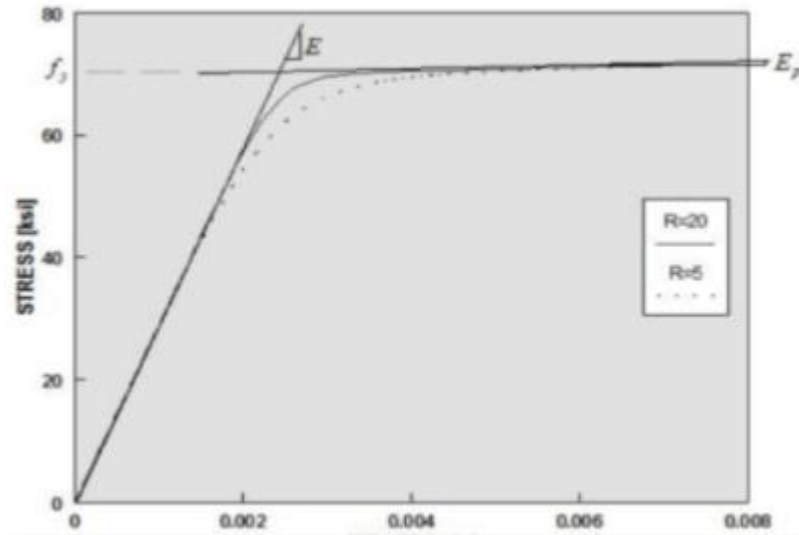


Figure 4.5. OpenSees *Steel02* material response (Mazzoni et al., 2007)

The elements that have been used to model the beams and columns are beam with hinges which belong to the nonlinear beam column elements category. These elements are able to concentrate plasticity in the user defined plastic hinge sections located at element's ends, while the remaining middle segment zone behaves elastically. This element also provides the ability to define the length of plastic hinges at its ends while considering two integration points per plastic hinge that represent the linear curvature distribution.

To sum it up, in order to assign the elements that simulate the behaviour of beams and columns in the OpenSees software, the following parameters should be defined: the member geometry, the length of the plastic hinge and the cross-sectional properties of the structural element.

The length of the plastic hinge is assumed to be equal to the height of member's cross-section. The beams and columns cross-sectional definition is composed of vertical and horizontally placed fibres as illustrated in Figure 4.6.

The web of the cross-section contains 6 vertical fibres and each flange has 5 horizontal fibres which gives a total of 16 fibres.

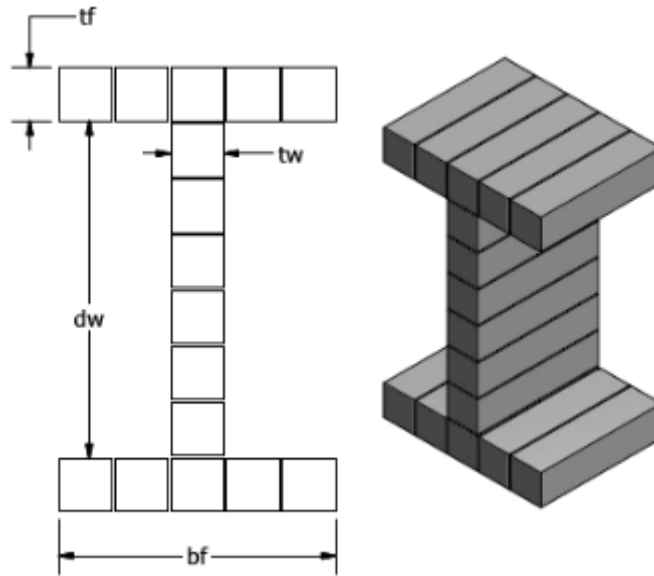


Figure 4.6. Beams and columns cross-section fibres discretization in OpenSees

4.4.3 Braces modeling in OpenSees

Each brace member is discretized in 16 force based nonlinear beam column element with distributed plasticity. Because this element does not contain pre-defined integration points, four integration points have been considered per element. The same *Steel02* material is assigned to braces. The out-of-straightness parameter is set to be equal to $L/500$ for HSS braces as per Zemian recommendation (Zemian, 2010), where L is half of the brace length in the particular case of “X-bracing”. The brace cross-section is then divided into 216 fibres, following the discretization model with rounded corners (Tremblay, 2008) as illustrated in Figure 4.7.

Each end of individual half of brace is connected to beam and column by means of gusset plate. Both diagonal bracing members are connected in the intersection points 5,8,11 and 14 with

two *zero-length* spring elements assigned in the *zero-length* elements, C_2 as seen in Figure 4.8 which illustrates the OpenSees model.

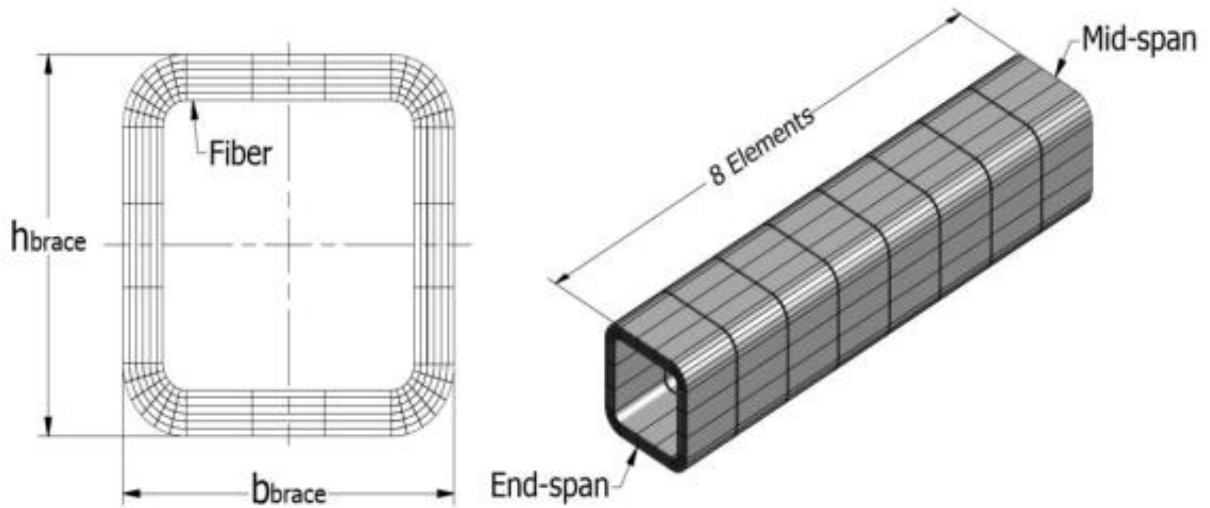


Figure 4.7: Fibre distribution of braces cross-section, and brace member discretization in OpenSees

4.4.4 CBF model

The overall building structure has two seismic force resistance systems in both X and Y directions. Half of the gravity columns are added to the model as is shown in Figure 4.4 in order to simulate the behaviour of the participating stiffness in the desired load applying direction. These gravity columns are defined as pin-ended members over two storeys and are linked at each floor level to the seismic force resistant systems by rigid links as shown in Figure 4.8. Columns of CBFs are pinned connected to beams and are continuum over two storeys. Beams are pinned connected to columns, as is shown in Figure 4.2.

4.4.5 Gusset plates modelling definition

In the nonlinear range, HSS braces buckle out-of plane and plastic hinges are developed at brace's mid span and in gusset plates at the end of the brace. This behaviour of brace's gusset plate is simulated in the zero-length element as rotational springs assigned in the *zero-length* elements illustrated in Figure 4.8. The *zero-length* element is located between the rigid link and the brace member. These connections simulated by two rotational and one torsional spring are numbered as C_1 , C_3 , C_5 and C_6 . These springs allow out-of-plane rotation, in-plane rotation and in-plane torsion.

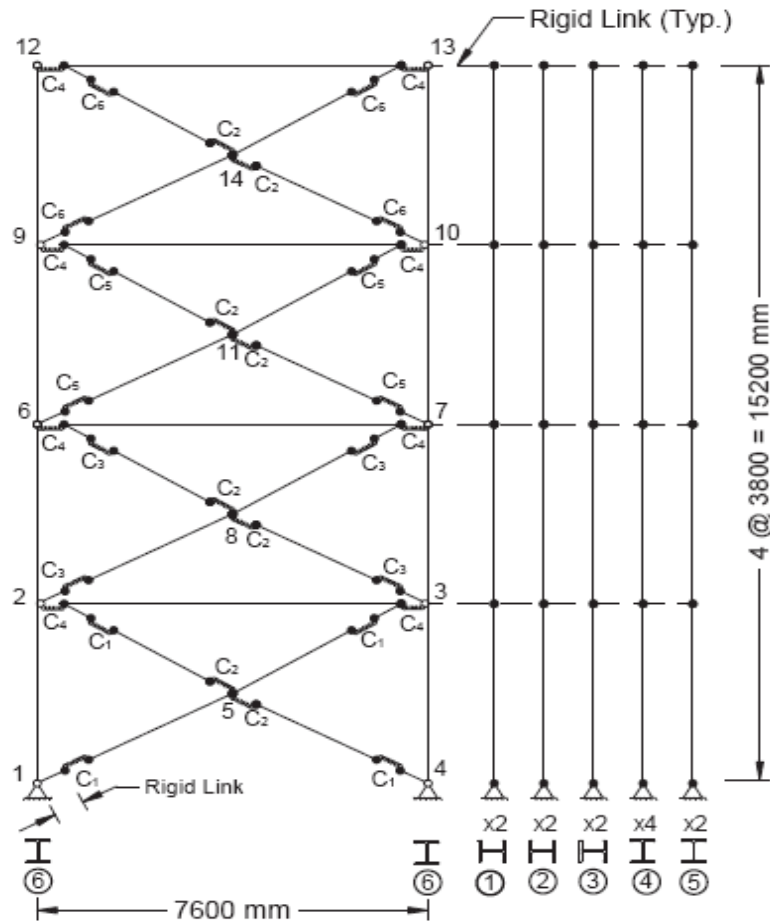


Figure 4.8: OpenSees model of the 4-storey CBF with participating gravity columns

The connection between the beam and column is simulated by the rotational spring C_4 as shown in Figure 4.8. This rotational spring assigned in the *zero-length* element has very small flexural stiffness in order to simulate the behaviour of beam defined theoretically as a pinned ended member.

In order to determine the dimensions for the gusset plate we have to follow several steps, starting by computing the length of welding, thickness of gusset plate, the Whitmore width, W_w , and by assuming the steel strength of steel plate. The geometry of gusset plate is depicted in Figure 4.9.

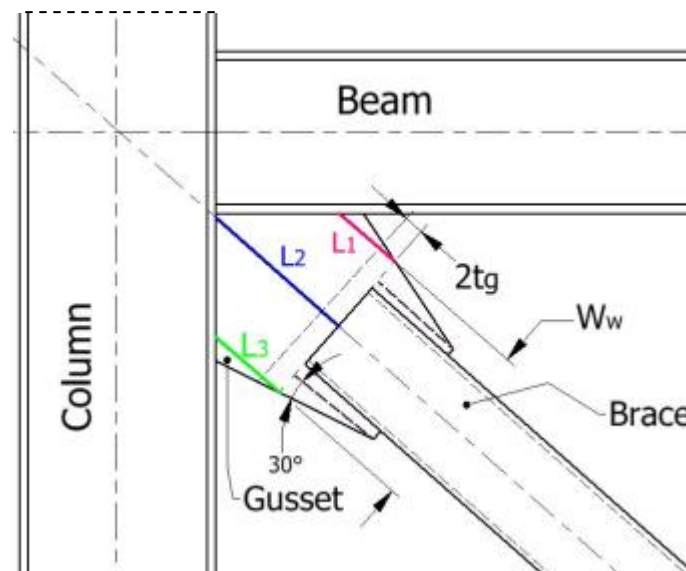


Figure 4.9. Brace to frame gusset plate connection

In order to meet the capacity design criteria, the compressive and tensile strength resistance of gusset plate should be greater than that of the braces. By rephrasing, the probable tensile and compression resistance of braces (T_u and C_u) should be lower than the gusset

resistance in tension and compression ($T_{r,g}$ and $C_{r,g}$) that are given in Equation 4.9 and Equation 4.10, respectively.

$$T_{r,g} = \phi F_y W_w t_g \quad (4.9)$$

$$C_{r,g} = \phi A_g F_y (1 + \lambda_g^{2n})^{-\frac{1}{n}} \quad (4.10)$$

where, λ_g is given in Equation 4.11.

$$\lambda_g = \frac{KL_g}{t_g} \sqrt{\frac{12F_y}{\pi^2 E}} \quad (4.11)$$

The length of gusset plate showed in Equation 4.11 is calculated as: $L_g = L_{ave} = (L_1 + L_2 + L_3)/3$ and $k=0.5$. The representation of L_1 , L_2 , and L_3 is shown in Figure 4.9.

The length of $2t_g$ is required to allow the plastic hinge to form in the gusset plate when the brace buckles out-of-plane.

In the OpenSees model, the gusset plate connection is replicated by means of two rotational and one torsional spring assigned in the *zero-length* element that connects the brace's end with the rigid link.

The out-of-plane flexural stiffness of the gusset plate, as proposed by Hsiao et al. (2012) is EI_g/L_{ave} , where L_{ave} is the average of the lengths: L_1 , L_2 and L_3 that have been depicted in Figure 4.9, E is the elastic modulus of the gusset plate and I_g is the moment of inertia which is $I_g = W_w t_g^3/12$. Thus, the stiffness assigned to one rotational spring that simulates the out-of-plane bending of gusset is in agreement with that proposed by Hsiao et al. (2012) and the stiffness assigned to the second rotational spring which simulates the in-plane bending is assigned to be larger than the flexural stiffness of brace. The third spring assigned in the *zero-length* element is taking into consideration the torsional stiffness of the gusset plate defined as GJ/L_{ave} where G is the shear modulus of steel and J the torsional constant which is given by Equation 4.12.

$$J = 0.333b_w t g^3 \quad (4.12)$$

In this study, $F_y = 350$ MPa is the yield strength of steel, J is the torsional moment of inertia for the gusset plate and I the flexural moment of inertia of the same plate. The rigid link showed in Figure 4.8 simulates the remaining part of the gusset plate that is welded to beam and column. Elastic steel material is assigned to all rigid links.

4.5 Dynamic Analysis of the CBF System Using OpenSees

For Victoria, B.C., the ground motions used to simulate the seismic load arrive from two sources: crustal and subduction. In general, the time step of recording the accelerogram's amplitudes is 0.005s, 0.01s and 0.02s. The integration time used to run the OpenSees models is set to 0.0005 seconds and must be smaller than the time step of the given record. The smaller the increment is the longer time is required to complete the analysis, while the convergence problem diminishes.

In the case of steel structures, the percentage of the critical damping applied to all of the structures elements except braces, is 2%. The braces are excluded from being damped due to the nature of nonlinear hysteretic behaviour when the dissipated energy is released. In order to better correlate the results of the building, the fundamental period as well as the 2nd vibration mode from the OpenSees software and Etabs 3D model are given in Table 4.6. Both periods of building were calculated in elastic range based on the elastic stiffness.

Table 4.6. CBF building period in finite elements software simulation

Height [m]	T_a [s]	T_1 [OpenSees]		T_1 [Etabs 3D]	
		T1	T2	T1	T2
15.2	0.760	0.825	0.208	0.816	0.210

Thus, in elastic range both values resulted for T1 in OpenSees and ETABS are very close.

4.5.1 Selecting the ground motions

In general, the seismic hazard for a given location is characterized by uniform hazard spectral ordinates, S_a , that are specified at periods of 0.2, 0.5, 1.0, and 2.0s for a return period of 2475 years or 2% probability of exceedance in 50 years. For Victoria, the spectral ordinates in units of ground acceleration are showed in Table 4.2. Thus, in this study, all ground motions were selected so that their spectra matched the UHS in the range delimited by the period of interest: $0.2T_1$ and $1.5T_1$. For analyses, two assemblies of seismic ground motions given in Table 4.7 have been selected. The first assembly is composed of 7 crustal ground motions that were selected from the PEER Ground Motion Database Beta Version (2010) in order to match the magnitude scenarios for Victoria considered as being in the range of M6.5 to M7.2. These records correspond to Class C soil for which the shear wave average velocity is between 360 and 760 m/s. The second assembly of ground motions is used to simulate the Cascadia Subduction event, and consists of seven ground motions with a magnitude of M9.0. Researchers anticipate similarities between the Tohoku records registered during the M9 Tohoku event (March 2011) and potential records generated by Cascadia subduction fault. The seven records corresponding to site class C were selected from the following website: www.k-net-bosai.go.jp

Table 4.7: Selected ground motions characteristics

ID	Event	Station	Comp	M _w	R _{hvp} [km]	PGA [g]	PGV [m/s]	PGV/PGA [s]	t _d [s]
CRUSTAL GROUND MOTIONS									
C1	Loma Prieta	Anderson Dam	739-250	6.9	19.9	0.244	0.203	0.0832	10.51
C2	Loma Prieta	Gilroy Array #3	767-0.0	6.9	36	0.555	0.358	0.0066	6.36
C3	Loma Prieta	Lab Apeel 9	787-360	6.9	54	0.278	0.292	0.0107	11.57
C4	Northridge	Castaic	963-90	6.7	44	0.568	0.517	0.0093	9.08
C5	Northridge	Palo Alto	986-195	6.4	37	0.186	0.236	0.0129	11.43
C6	Northridge	LA-UCLA Grounds	1006-90	6.7	25	0.278	0.217	0.008	11.30
C7	Northridge	Moorpark-Fire Station	1039-180	6.7	36	0.292	0.204	0.0071	14.22
SUBDUCTION GROUND MOTIONS									
S1	2011/11/3 Tohoku	MYG001	EW	9	155	0.43	0.23	0.054	83
S2	2011/11/3 Tohoku	MYG004	EW	9	184	1.22	0.48	0.04	85
S3	2011/11/3 Tohoku	FKS005	EW	9	175	0.45	0.35	0.079	92
S4	2011/11/3 Tohoku	FKS010	EW	9	189	0.86	0.56	0.066	66
S5	2011/11/3 Tohoku	FKS009	EW	9	216	0.83	0.44	0.054	74
S6	2011/11/3 Tohoku	IBR004	EW	9	273	1.03	0.38	0.037	33
S7	2011/11/3 Tohoku	IBR006	EW	9	283	0.78	0.30	0.039	36

Table 4.7 reveals the list of selected records and shows the earthquake magnitude M_w , the epicentral distance, R , the peak ground acceleration PGA, peak ground velocity PGV and the Trifunac duration t_d of the earthquake. The ratio between the PGV/PGA, peak ground velocity to peak ground acceleration is an important factor for selecting the ground motions based on their frequency content.

The number of selected records per group agrees to ASCE-SEI 2007 provisions. Thus, when three different records are considered the maximum response should be selected. Afterwards, when seven records are considered the results are expressed as being the mean. The selected accelerograms as recorded are illustrated in Figure 4.10 and Figure 4.11.

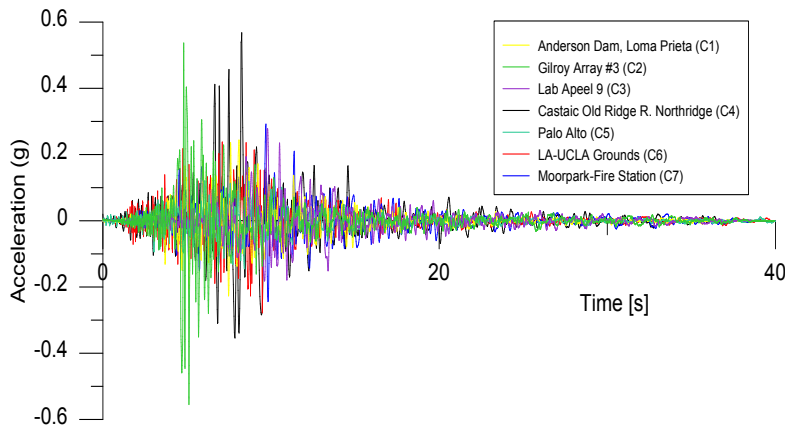


Figure 4.10. Selected crustal ground motions

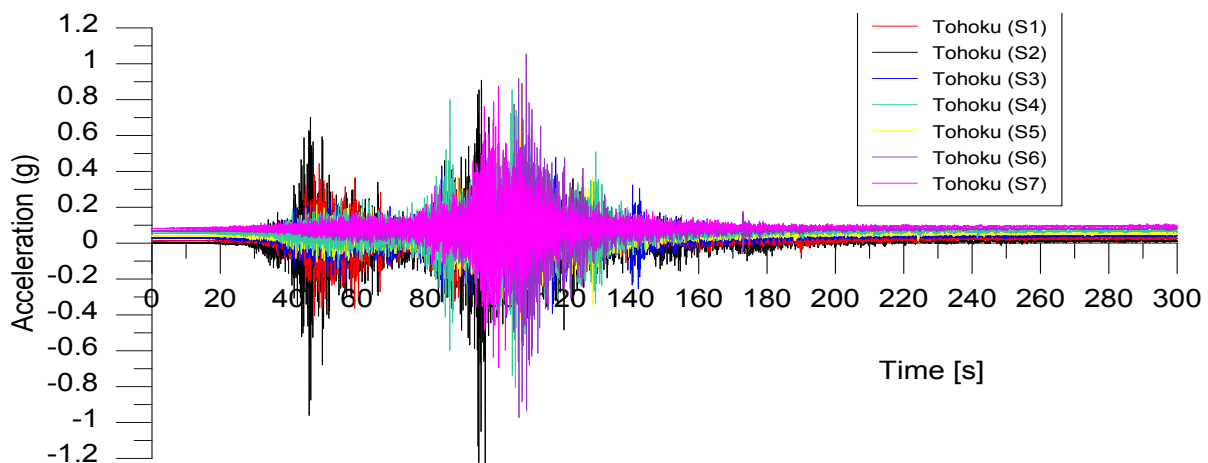


Figure 4.11. Selected subduction ground motions accelerations

4.5.2 Ground motions scaling procedure

The ground motions selected have to undergo a scaling procedure in order to match the uniform hazard spectrum between $0.2 \cdot T_1$ and $1.5 \cdot T_1$ at the building location. The NBCC 2010 code does not specify a procedure regarding ground motions scaling. Although, it is mentioned that all selected ground motions should be scaled to match the UHS ordinate at the fundamental period, T_1 (ordinate $S(T_1)$) and to be at least above the UHS at all points corresponding to the period of higher modes. More in detail, the ASCE/SEI 2007 provisions require that the mean of the 5% damped response spectra of a minimum of seven scaled ground motions should match or be above the UHS, over the period of interest $0.2 \cdot T_1 - 1.5 \cdot T_1$ as depicted in Figure 4.3. Herein, the ASCE/SEI2007 requirements are applied.

During the inelastic behaviour of structure, the structure's stiffness starts to degrade and the building should sustain an elongated fundamental period that may be larger than $1.5 \cdot T_1$ (Kalkan and Chopra, 2010).

The employed method for scaling ground motions is based on the Reyes and Kalkan methodology (2011) which consists on minimizing the discrepancy between the scaled acceleration response spectrum of each record and the UHS over the specified period range ($0.2 \cdot T_1 - 1.5 \cdot T_1$). Thus, in the studied case, the interval of interest is between $0.2 \cdot T_1 = 0.165$ s and $1.5 \cdot T_1 = 1.237$ s. The resulted scale factors are given in Table 4.8. It is noted that scale factor of 1.0 was used for all subduction records.

Table 4.8: CBF scale factors for a 4-storey frame with gusset plates

Crustal Ground Motions							
GM ID	C1	C2	C3	C4	C5	C6	C7
Scale Factor	1.82	1.00	1.62	1.032	2.16	2.31	1.98
Subduction Ground Motions							
GM ID	S1	S2	S3	S4	S5	S6	S7
Scale Factor	1	1	1	1	1	1	1

For example in Figure 4.12 and Figure 4.13 the unscaled spectral accelerations of the crustal and subduction ground motions are depicted, while in Figures 4.14 and 4.15 the scaled acceleration spectra for crustal and subduction, respectively, are illustrated, as well as the mean of 7 records.

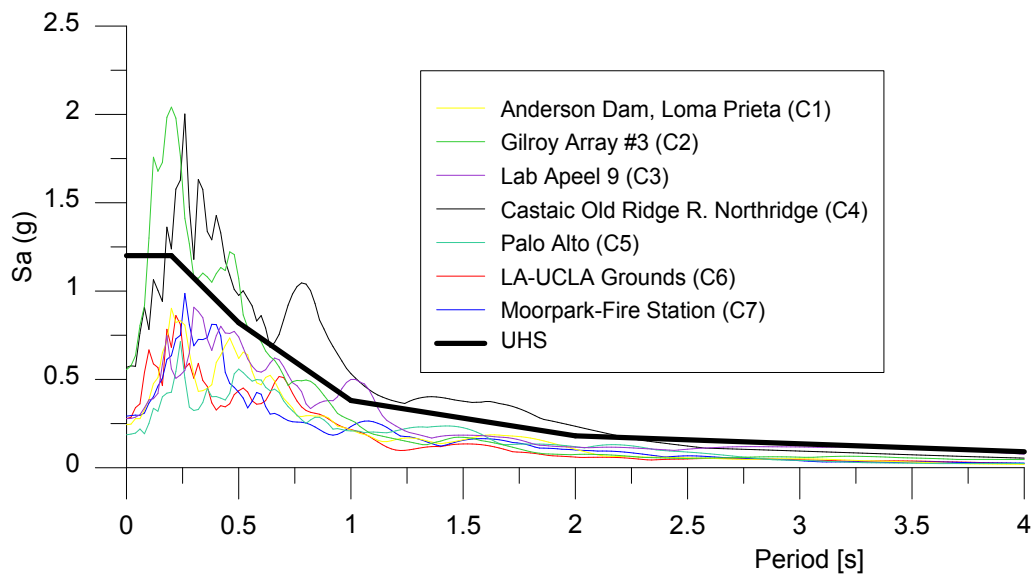


Figure 4.12: Crustal GM's non-scaled spectral accelerations $Sa_{(g)}$

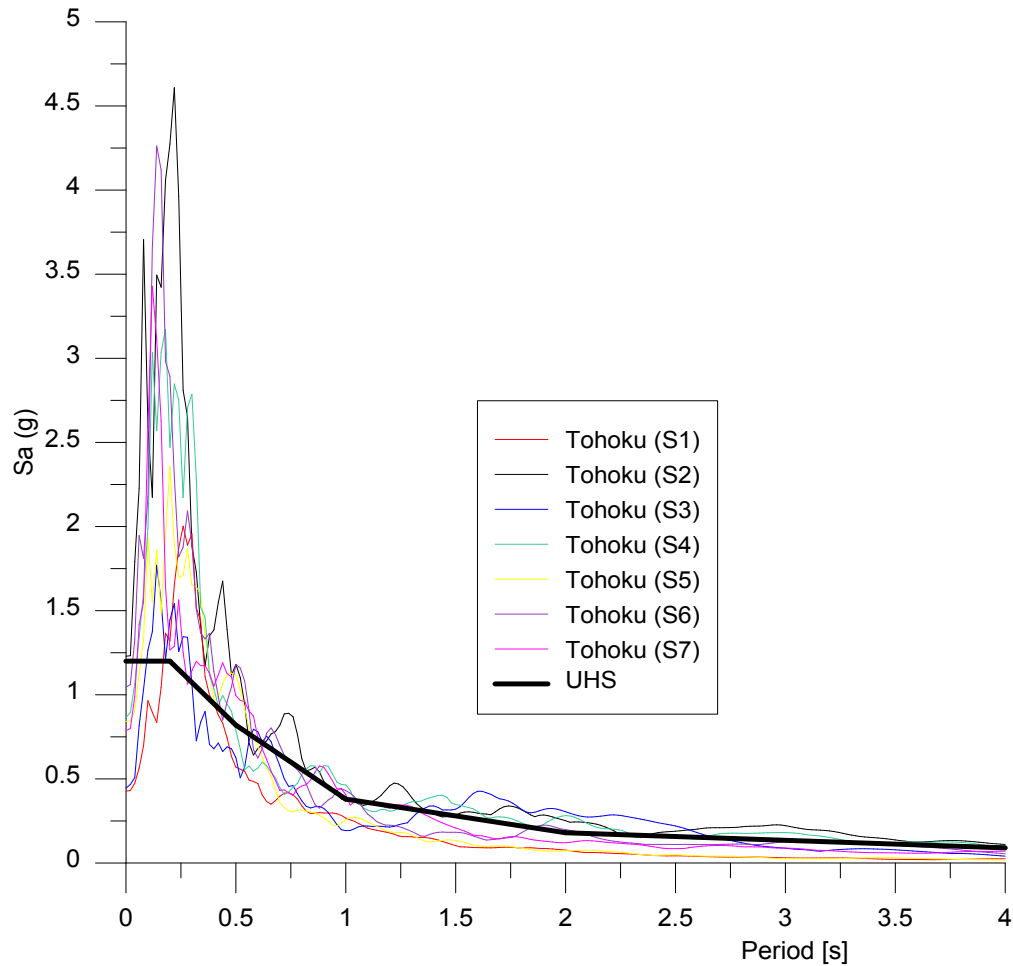


Figure 4.13: Subduction GM's non-scaled spectral accelerations $Sa_{(g)}$

The acceleration response spectrum obtained from the selected Tohoku records exhibit very large ordinates in the short period range 0.1-0.35s. Thus, low-rise buildings with a fundamental period in this range may be exposed to ground motions that are two times larger than those required by the code. However, buildings with a fundamental period larger than 1.6 seconds are not exposed to increased acceleration response spectrum ordinates. Although in the interval of 0.7-0.8 s, the average spectrum shows a slightly lower value than that required by code, the scale factor was not raised above 1.0 (Tirca et al. 2012). It is noted that for class C soil the uniform hazard spectrum and the design spectrum are the same.

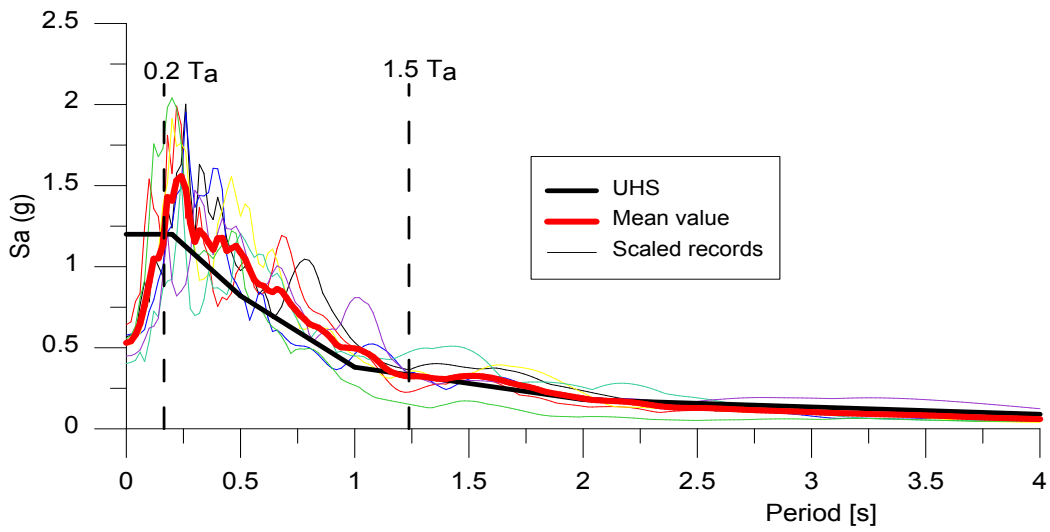


Figure 4.14: Spectral acceleration of scaled Crustal GMs with the Mean and UHS

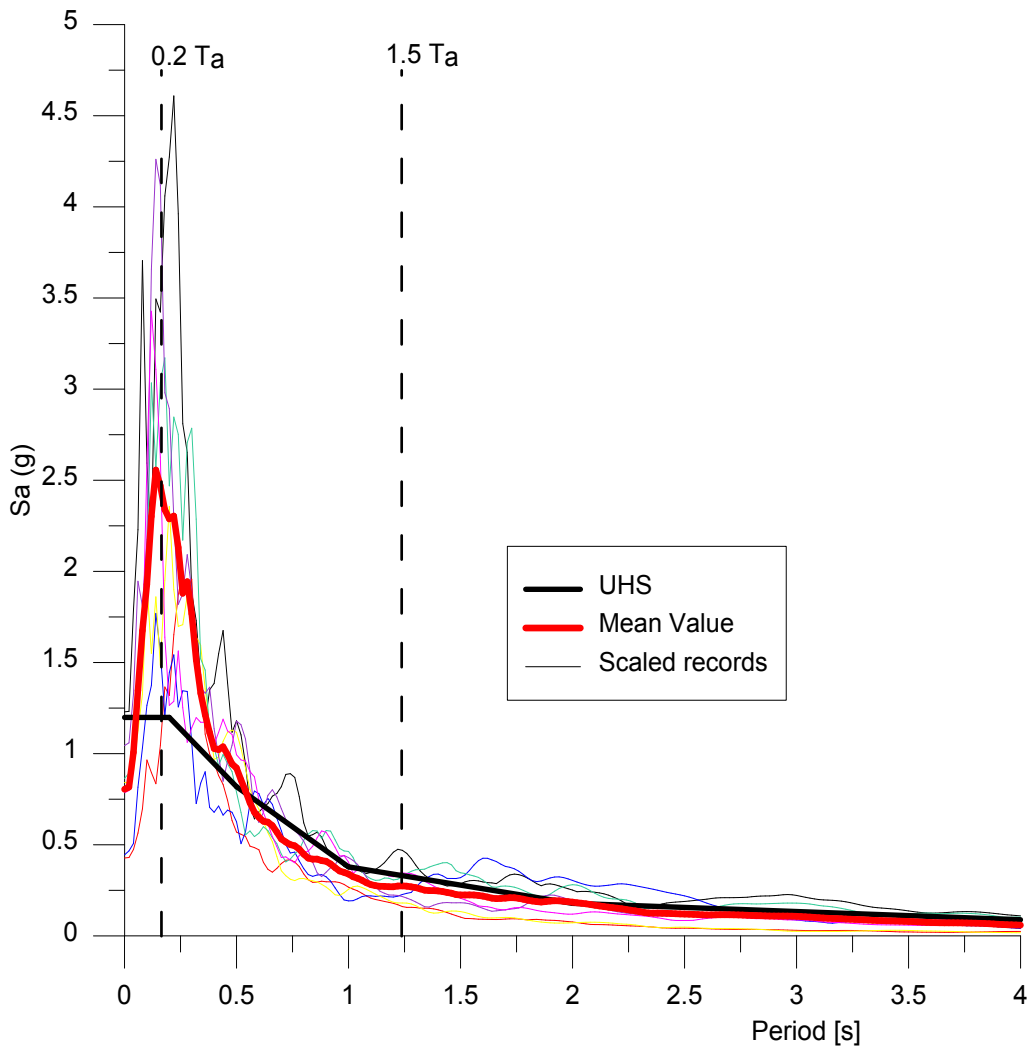


Figure 4.15: Spectral acceleration of scaled Subduction GMs with the Mean and UHS

4.5.3 Seismic response of the studied CBF's

The behaviour of the 4-storey CBF was analysed under the 14 records. The distribution of inter-storey drift over storey height for each ground motion of each assembly is shown in Figure 4.16. The results demonstrate a larger inter-storey drift values obtained under the crustal than the subduction records.

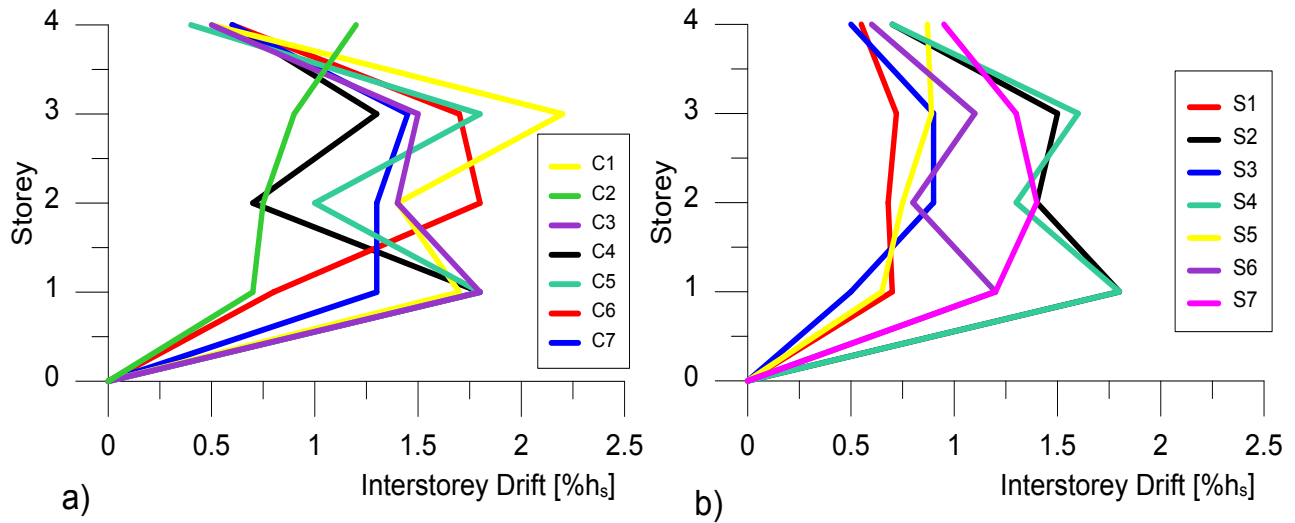


Figure 4.16. The CBF response in terms of peak interstorey drift for: a) crustal, b) subduction.

The behaviour of a 4-storey CBF is discussed in detail by analyzing the seismic response under two crustal and two subduction records that subjected the building to large demands. These selected ground motions are the two Northridge records C5 (986-195) and C7 (1039-180), as well as two of Tohoku records such as S2 (MYG004) and S4 (FKS010). It is noted that MYG004 accelerogram is composed of two overlapping ground ruptures and FKS010 was generated from a large ground motion energy input.

The time-history response of all braces under the C5 ground motion is illustrated in Figure 4.17 where braces are identified by the given joints according to Figure 4.8. The brace response is showed in terms of force-displacement. As reported, braces of the bottom two floors (1st and 2nd)

were subjected to large inelastic deformations in tension and compression after buckling occurred, while braces of the upper two storey have performed in the elastic range. The maximum deformation demand occurred at the second floor where 80 mm brace deformation was reported in compression. Braces of the 1st floor level have undergone almost the same deformation demand as the 2nd floor braces. As depicted in Figure 4.16, the maximum interstorey drift occurred at the 1st floor level and is about 1.7%h_s. Due to the large deformation of the 2nd floor brace, large interstorey drift was occurred at the 3rd floor, as well (1.65%h_s). Further, the time-history response series of each floor under the C5 ground motion is shown in Figure 4.18 in terms of floor's deformations and the corresponding interstorey drift. As illustrated in Figure 4.18b, all floors deformed on the same building's side. At the 1st and 3rd floor level, a maximum displacement of 80 mm and 74 mm, respectively was recorded. In addition, the maximum interstorey drift occurred right after the time when the PGA was reached (t ~ 9.0 s). The residual (permanent) interstorey drift values are given in Table 4.9. It is noted that five seconds of zero accelerogram's amplitude were added to each ground motion in order to analyse the residual interstorey drift. From Table 4.9, the maximum residual interstorey drift occurred at the 1st floor.

Table 4.9. Interstorey and residual interstorey drift under the C5 and C7

Ground Motion	ID	Storey	Interstorey drift % h _s	Residual interstorey drift % h _s
C5	986-195	4	0.4	0.3
		3	1.8	0.4
		2	1.0	0.2
		1	1.8	0.5
C7	1039-180	4	0.6	0.15
		3	1.45	0.4
		2	1.3	0.25
		1	1.3	0.35

The response of the 4-storey CBF building in term of force-displacement experienced by braces is illustrated in Figure 4.19 under the C7 record. This record shows 4-5 peaks between $t = 8.0$ s and $t = 15.0$ s. The maximum interstorey drift under the C7 record occurred at the 3rd floor level and is equal to $1.45 \%h_s$. Braces of bottom two floors experienced inelastic deformations after buckling occurred, while the braces of the upper two floors remained in the elastic range. The larger brace's deformation occurred at the 2nd floor level and is about 60 mm in both tension and compression (Figures 4.19 e and f). Similarly, all floors deformed on the same building's side (Figure 20 b) and the maximum residual interstorey drift occurred at the 3rd floor (e.g. $0.4\%h_s$ as per Table 4.9).

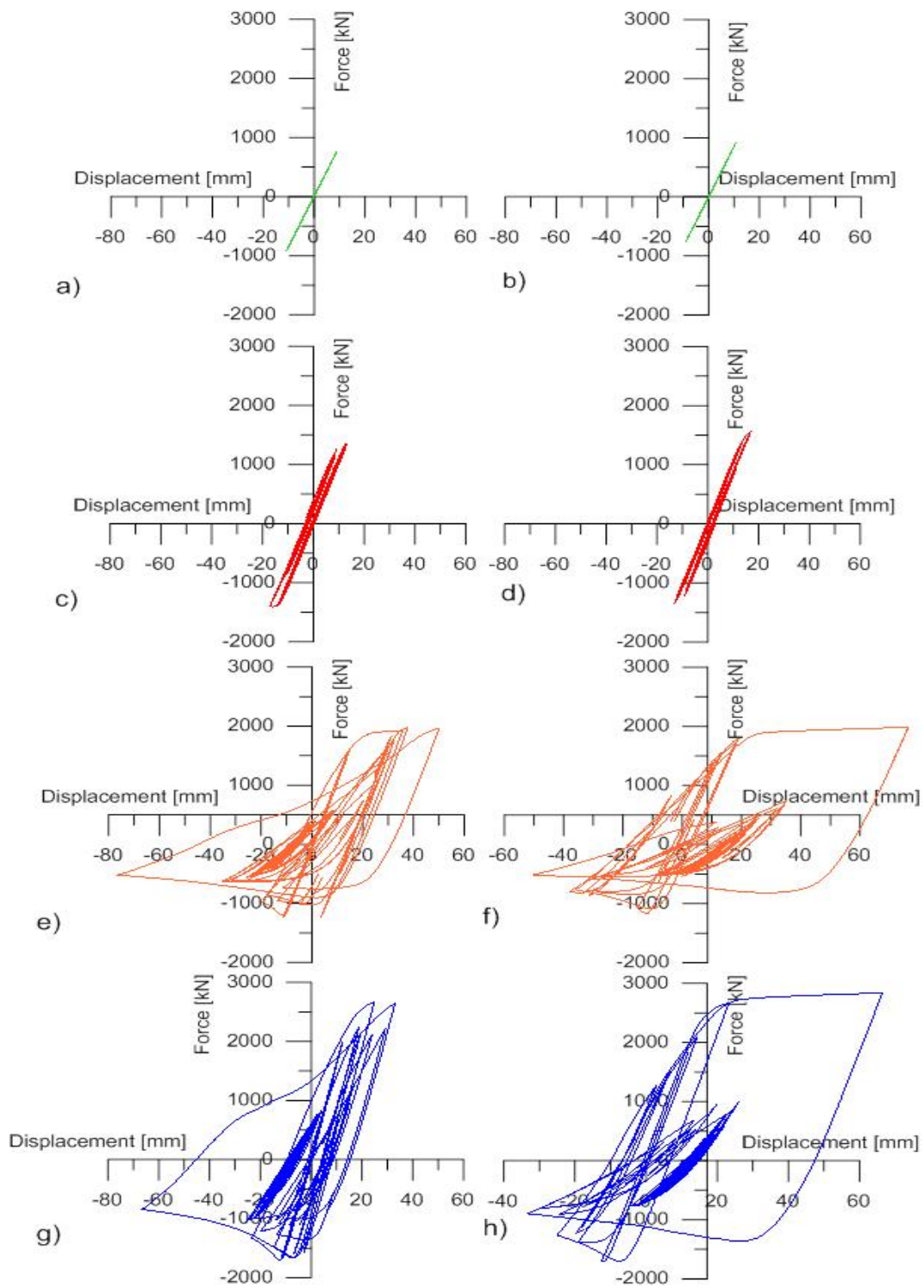


Figure 4.17. The CBF time-history response of braces under C5 record: a) 4th St. Brace 9-13, b) 4th St. Brace 10-12, c) 3rd St. Brace 6-10, d) 3rd St. Brace 7-9, e) 2nd St. Brace 2-7, f) 2nd St. Brace 3-6, g) 1st St. Brace 1-3, h) 1st St. Brace

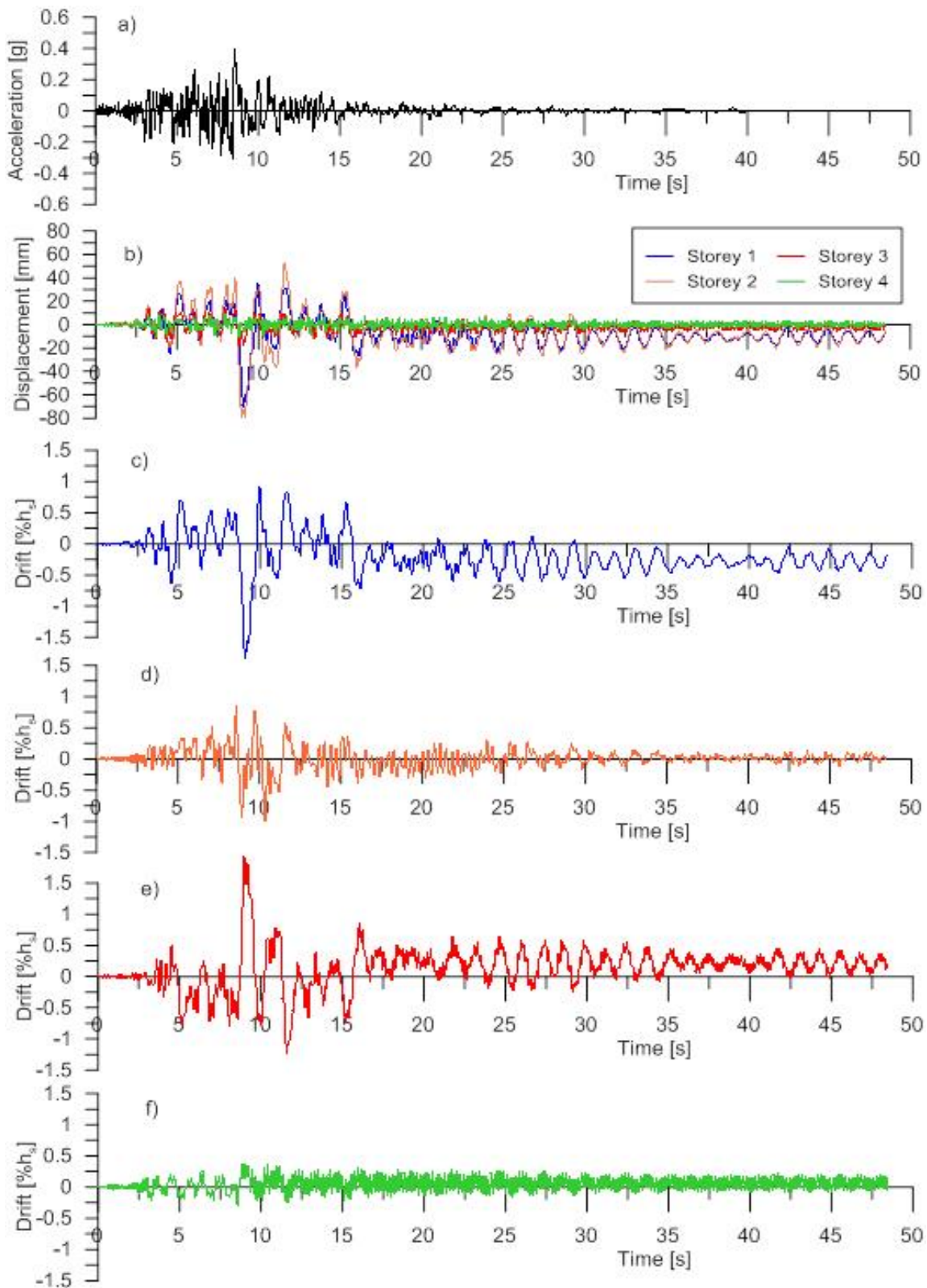


Figure 4.18. CBF time-history response under C5: a) Scaled GM, b) Storey-displacement time-history series, c) 1st St interstorey drift, d) 2nd St. interstorey drift, e) 3rd St. interstorey drift, f) 5th St. interstorey drift

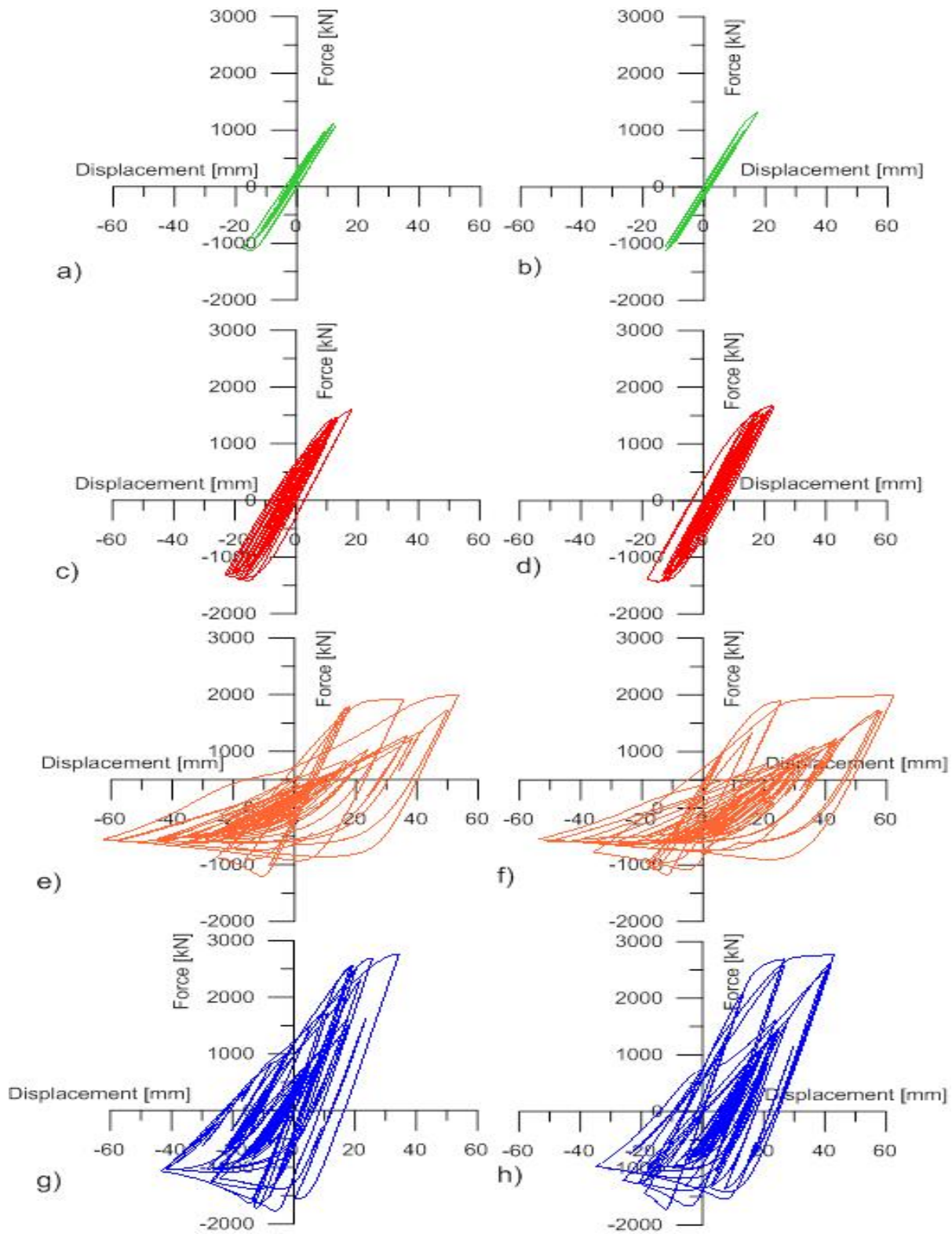


Figure 4.19. CBF time-history response of braces under C7: a) 4th St. Brace 9-13, b) 4th St. Brace 10-12, c) 3rd St. Brace 6-10, d) 3rd St. Brace 7-9, e) 2nd St. Brace 2-7, f) 2nd St. Brace 3-6, g) 1st St. Brace 1-3, h) 1st St. Brace 2-4.

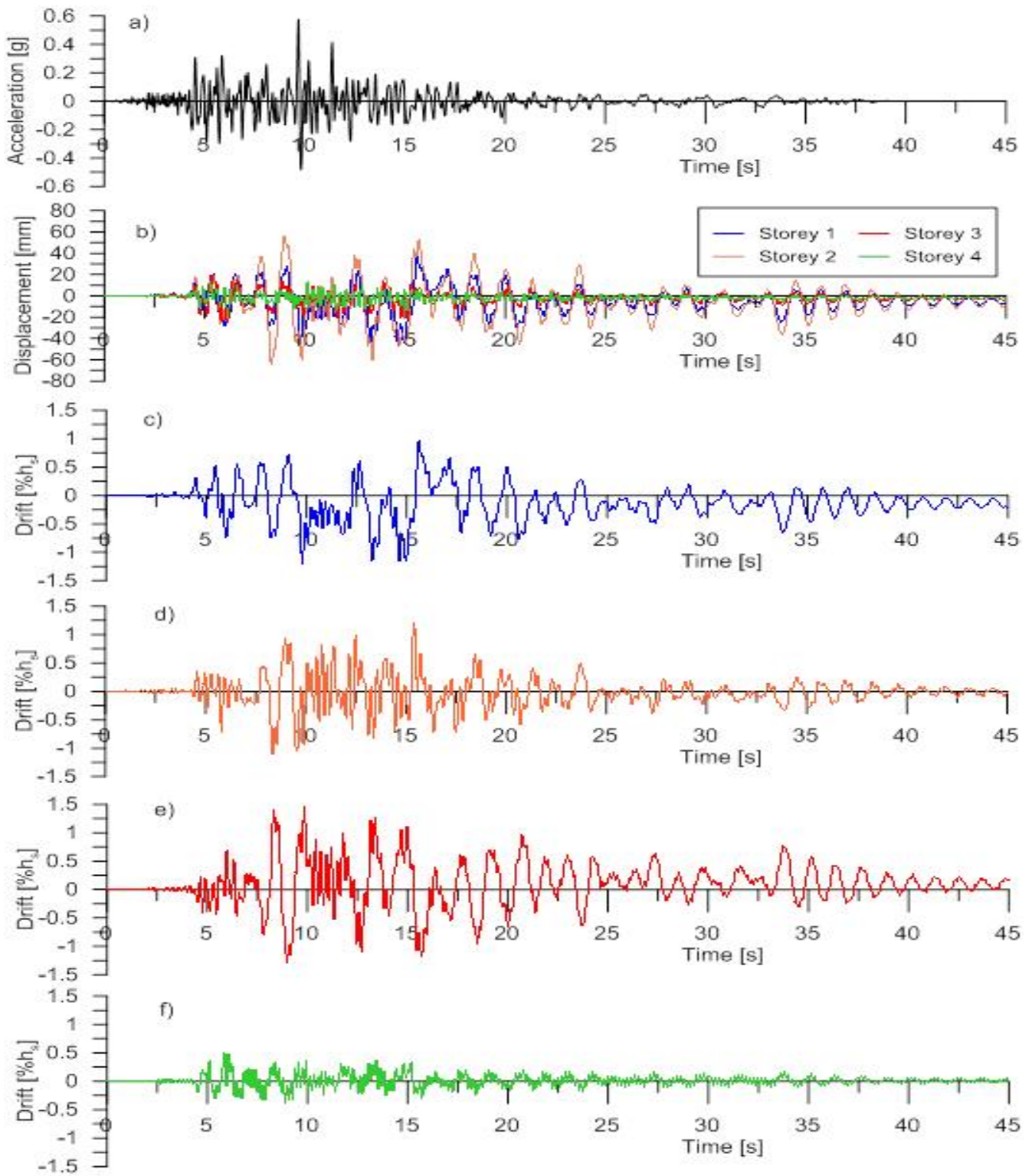


Figure 4.20. CBF time-history response under C7: a) Scaled GM, b) Storey- displacement time-history series, c) 1st St. interstorey drift, d) 2nd St. interstorey drift, e) 3rd St. interstorey drift, f) 4th St. interstorey drift

Both selected subduction ground motions S2 and S4 demanded a similar peak interstorey drift over the building height which is $1.8\%h_s$ and occurred at the 1st floor (Figure 4.16). Under both records, the larger damage demand occurred at the bottom two floors where braces experienced buckling followed by yielding in tension. In both cases the maximum demand in brace deformation was about 80 mm at the 1st floor and about 60 mm at the 2nd floor. Braces of the 3rd floor have experienced inelastic response but the demand was smaller than that imposed to the floor below. Braces of the top floor level have reached buckling in compression. The force-deformation hysteresis loops imposed by S2 record to all braces are depicted in Figure 4.21, while the time-history series of floors deformation and interstorey drift are depicted in Figure 4.22. The S2 accelerogram showed in Figure 4.22a illustrates double peaks on both directions that occurred about at the same time: $t = 46.02$ s and $t = 96.42$ s. It is interesting to note that the 1st and 2nd floor experienced larger interstorey drift when the second large shock was input into the building, while the 3rd floor experienced the same peak interstorey drift under both shocks.

Table 4.10 contains both peak interstorey drift and residual interstorey drift recorded under both S2 and S4 records. A maximum residual interstorey drift of $0.45\%h_s$ was recorded under S2 at the 1st floor level. The corresponding residual drift value is lower under the S4 record ($0.25\%h_s$) and was reached at the 3rd floor. Time-history response in term of force-deformation hysteresis loops are illustrated for all braces in Figure 4.23, while the time-history series of floors displacement and interstorey drifts are presented in Figure 4.24. Under the S4, the peak

Table 4.10. Interstorey and residual interstorey drift under S2 and S4

Ground Motion	ID	Storey	Interstorey drift % h_s	Residual interstorey drift % h_s
S2	MYG004	4	0.7	0.18
		3	1.5	0.28
		2	1.4	0.2
		1	1.8	0.45
S4	FKS010	4	0.7	0.1
		3	1.6	0.25
		2	0.1	0.14
		1	1.8	0.23

maximum floor displacement accelerograms values that occur in both positive and negative directions were recorded at $t=87.21s$ ($t=87.15s$) and $t=105.4s$ ($107.37s$) as seen in Figure 4.24a.

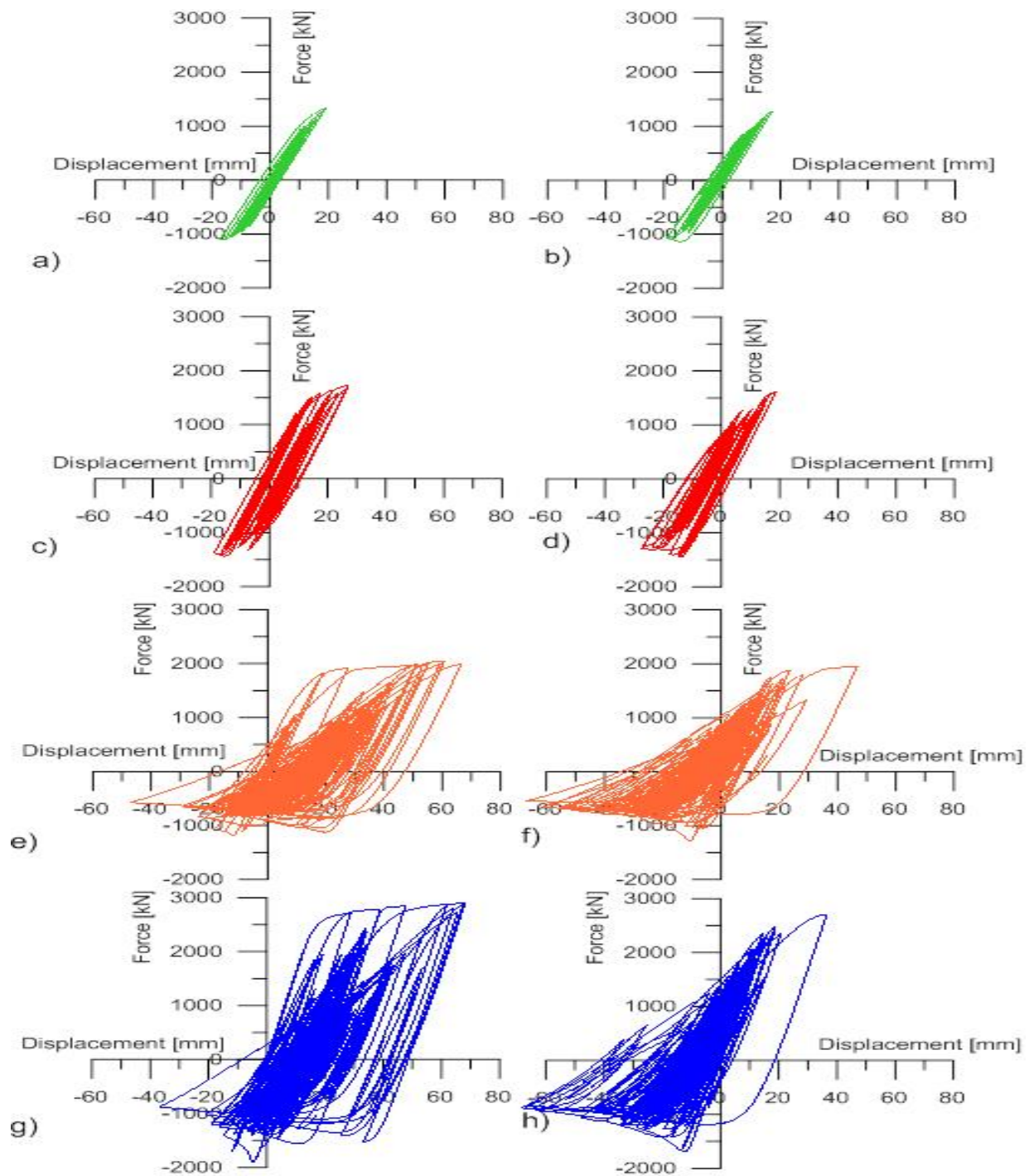


Figure 4.21. CBF time-history response of braces under S2: a) 4th St. Brace 9-13, b) 4th St. Brace 10-12, c) 3rd St. Brace 6-10, d) 3rd St. Brace 7-9, e) 2nd St. Brace 2-7, f) 2nd St. Brace 3-6, g) 1st St. Brace 1-3, h) 1st St. Brace 2-4

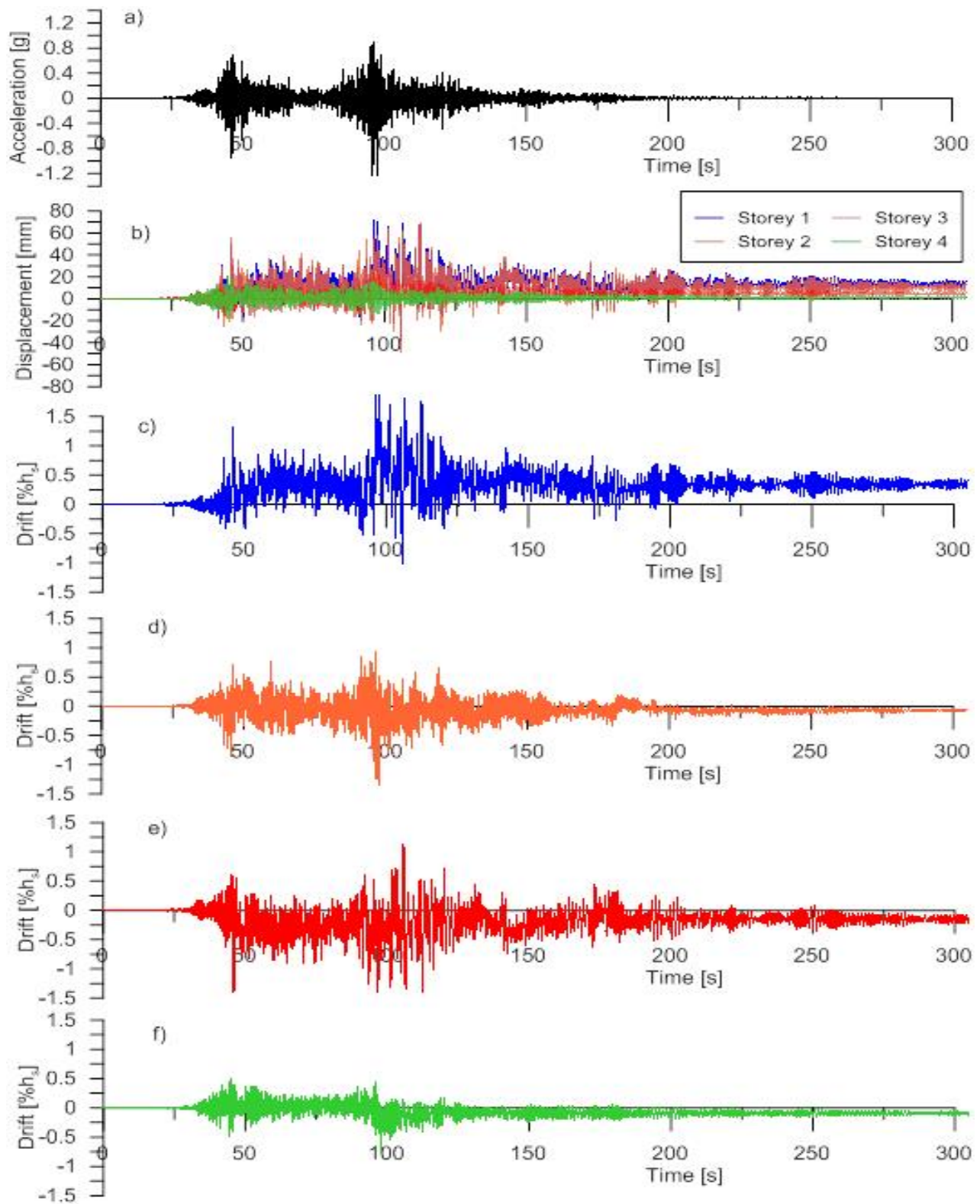


Figure 4.22. Time-history CBF response under S2: a) Scaled GM, b) Time-history series of storey –displacement, c) 1st St. interstorey drift, d) 2nd St. interstorey drift, e) 3rd St. interstorey drift, f) 4th St. interstorey drift

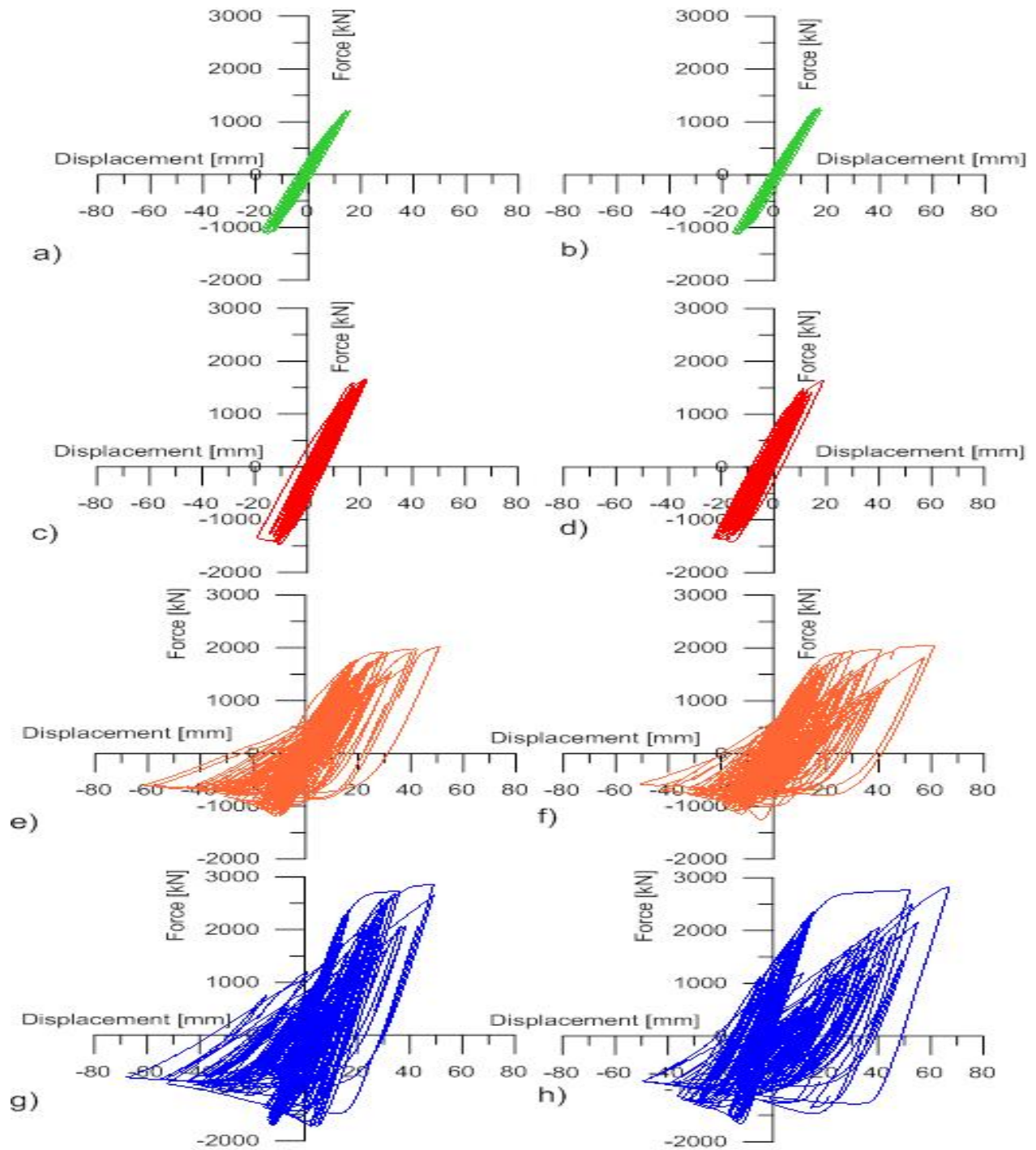


Figure 4.23. Time- history response of CBF braces under S4: a) 4th St. Brace 9-13, b) 4th St. Brace 10-12, c) 3rd St. Brace 6-10, d) 3rd St. Brace 7-9, e) 2nd St. Brace 2-7, f) 2nd St. Brace 3-6, g) 1st St. Brace 1-3, h) 1st St. Brace 2-4

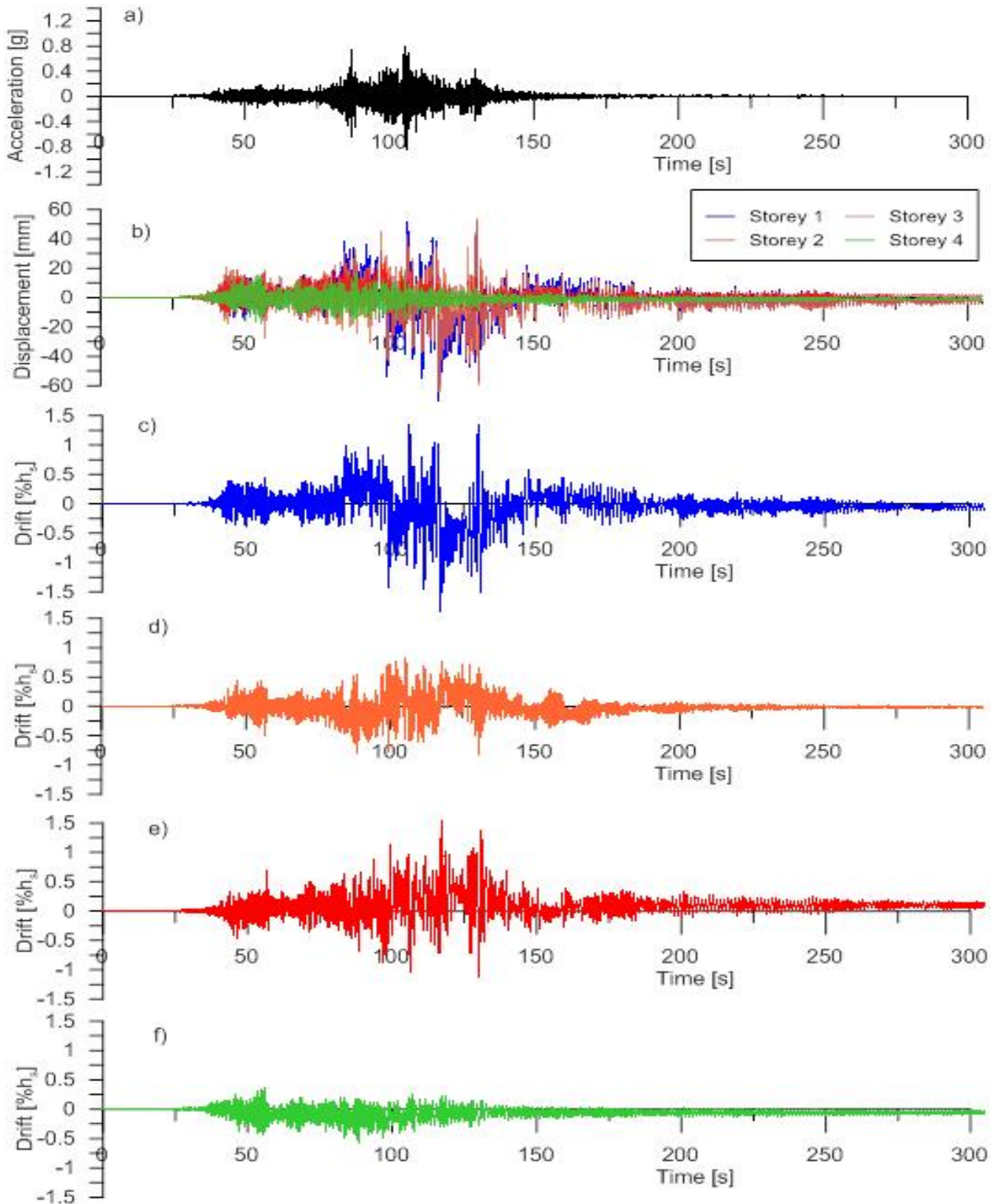


Figure 4.24. Time-history response of CBF under S4: a) Scaled GM, b) Storey - Displacement time-history series, c) 1st St. inter-storey drift, d) 2nd St. inter-storey drift, e) 3rd St. inter-storey drift, f) 4th St. inter-storey drift

Chapter 5. Seismic Analysis of a 4-Storey Building Equipped with Double-Pin Connections Displaced in-Parallel Using OpenSees

5.1 Design of the 4-storey CBF Equipped with Double-Pin Connections Displaced in-Parallel

The 4-storey moderately ductile CBF that has been designed in Chapter 4 is employed in this chapter in order to study the seismic response of the new proposed system: CBF with dissipative double-pin connections.

The same ground motions that were employed in the previous chapter, and showed in Table 4.7, are considered. A comparison between the seismic response of the two CBFs with and without dissipative connections is conducted.

5.2 Dissipative Connection Design for the 4-Storey CBF

The same members designed for the moderately ductile CBF that are given in Table 4.5 are used herein, while the changes are only applied at the level of the brace-to-column connections.

The design procedure of the CBF structure equipped with double-pin joints consists on sizing these brace-to-column connections to yield and dissipate the seismic input energy before braces reach their buckling strength. In this respect, it is recommended that the pin member should yield in bending at an applied force that equates 60-80% of brace's compressive strength, C_r . In this design, the computed pins' sizes of double-pin connections with pins displaced in-parallel are shown in Table 5.1. For example, the compressive resistance of HSS 178x178x13 brace located at the 1st floor level is $C_r=1729$ kN, whereas the seismic force resulted from the

static equivalent method is $C_f=1288.1$ kN. The difference between C_f and C_r is about 35%. The selected set of pins placed in-parallel is composed of 2 pins of a rectangular cross-section of 30mm x 45mm. Both pins have a cumulated ultimate force $P_u=1580$ kN, which is lower than the compression resistance of the brace and is higher than the seismic force demand. The P_u value satisfies Equation 5.1.

$$C_f < P_u < C_r \quad (5.1)$$

Although in the experimental tests depicted in Chapter 3 it was shown that the pin member was located on its weak axis, in this numerical example, the pin is located on its strong axis. However, further experimental tests have to be carried out in order to conclude on the position of pins versus their main cross-sectional axes. In general, the cross-section of pins placed in-parallel or in-line is smaller than that of a single pin.

Table 5.1. Pin member sizes for the 4-storey CBF with double-pin joints

St.	HSS Brace	Brace C_f [kN]	Brace C_r [kN]	Double-pin [mm]	Parallel Pins P_u [kN]
4	127 x 127 x 9.5	466.5	651.7	25 x 30	585.2
3	152 x 152 x 9.5	921.1	995.9	30 x 35	956
2	178 x 178 x 9.5	1165.6	1289.2	30 x 40	1248
1	178 x 178 x 13.0	1288.1	1729.0	30 x 45	1580

The double-pin connection with pins displaced in-parallel replace the gusset plate connections of brace-to-column joints, as is illustrated in Figure 5.1. However, in the OpenSees model, the properties of the gusset plate are removed and a new axial spring made up of *Pinching4* material is added in the zeroLength element. In the case of pins placed in-parallel, two axial springs will be added. These springs will simulate the behaviour of the proposed dissipative

connection discussed in Chapter 3. In the design, all structural members are intended to behave elastically, while the pin connections are sized to dissipate the input energy.

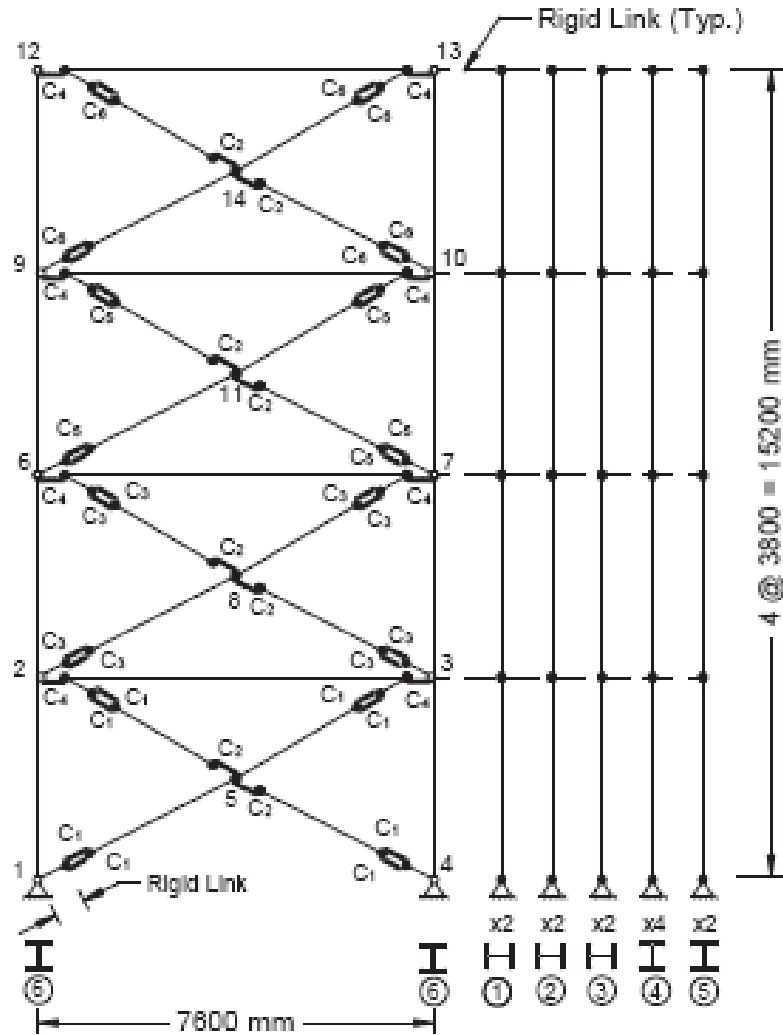


Figure 5.1. Elevation of a 4-storey CBF equipped with double-pin brace-to-column joints (OpenSees model)

5.3 Ground Motions Scaling Procedure for the 4-Storey Frame with Double-pin Connections

The building's fundamental period is established by evaluating the OpenSees frame model, and is revealed to be $T_1=1.386s$ while the second period is $T_2=0.360s$. The T_1 value of the new system is about 150% larger than the period of the CBF system given in Chapter 4.

The building was subjected to the same ground motion assemblies that are given in Table 4.7. The calculated scale factor, as explained in the previous chapter, is given in Table 5.2. Because the pin connection provides lower stiffness, the period increases and all crustal ground motions were re-scaled according to the computed buildings period.

Table 5.2. Scale factors applied to GMs used to analyse the 4-storey CBF with double-pin

Crustal Ground Motions							
GM	C1	C2	C3	C4	C5	C6	C7
Scale Factor	2.23	1.04	1.45	0.81	2.26	2.26	1.52
Subduction Ground Motions							
GM	S1	S2	S3	S4	S5	S6	S7
Scale Factor	1	1	1	1	1	1	1

5.4 Seismic Response of the Studied CBF with Double-Pin Connections

The behaviour of the 4-storey CBF was analysed under the new scaled 14 records. The distribution of inter-storey drift over storey height recorded under each ground motion of each assembly is shown in Figure 5.2.

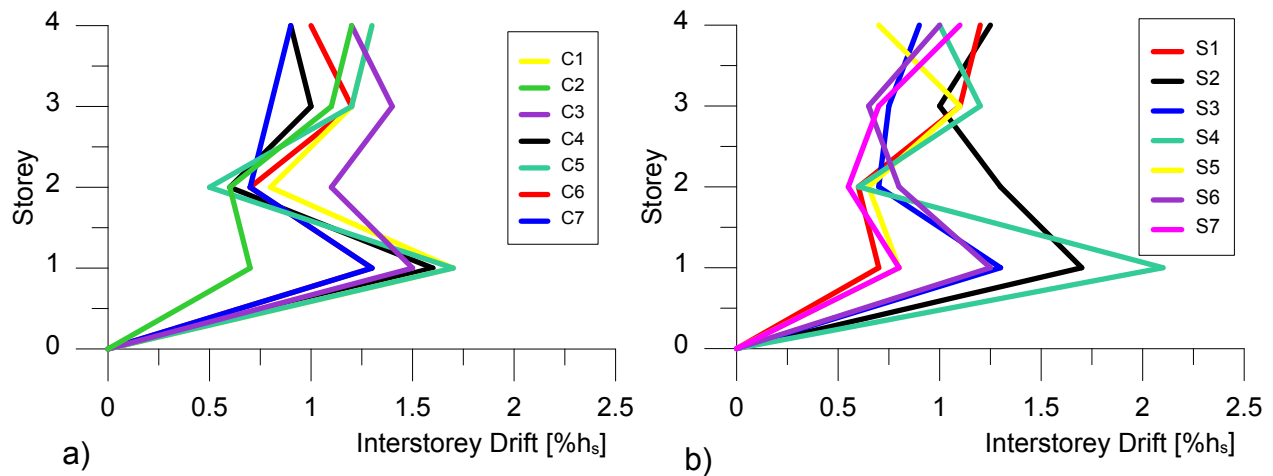


Figure 5.2. Interstorey drift of CBF with double-pin joints displaced in-parallel under: a) Crustal records b) Subduction records

Under all ground motion excitations, the HSS braces have remained elastically as expected. The results recorded under the C7 input are illustrated in Figure 5.3. It is demonstrated that braces of CBF with double-pin joints behave linearly elastic at all floors in both directions: tension and compression.

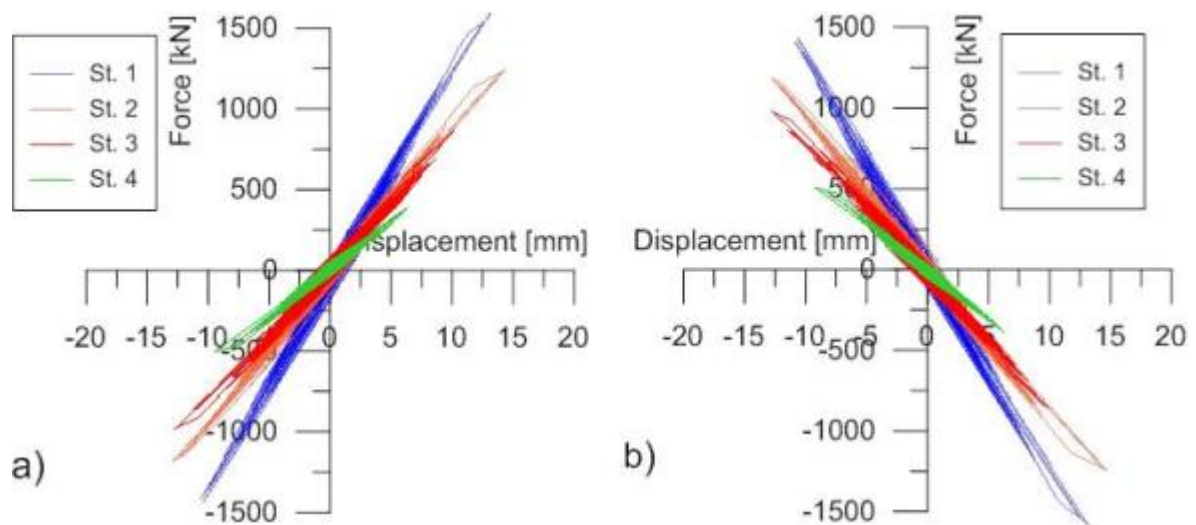


Figure 5.3. Behaviour of braces of CBF with double-pin connections under C7 record: a) 4th st. Brace 9-13, 3rd St. Brace 6-10, 2nd St. Brace 2-7, 1st St. Brace 1-3, b) 4th St. Brace 10-12, 3rd St. Brace 7-9, 2nd St. Brace 3-6, 1st St. Brace 2-4

Under the C5 record, pins located at the 3rd floor and made of rectangular 30x35mm cross-section reach their cumulative ultimate strength of 956 kN at the time $t = 18$ s when they exhibited a maximum displacement of 35 mm, as illustrated in Figure 5.4. The maximum floor displacement under the C5 record reaches 86 mm at the 3rd storey as depicted in Figure 5.5.

In the case of C7 record, the applied ground motion does not trigger the ultimate strength of the cumulated value for the pin forces in the overall frame response and provides a maximum joint displacement of 20 mm that is shown in Figure 5.6.

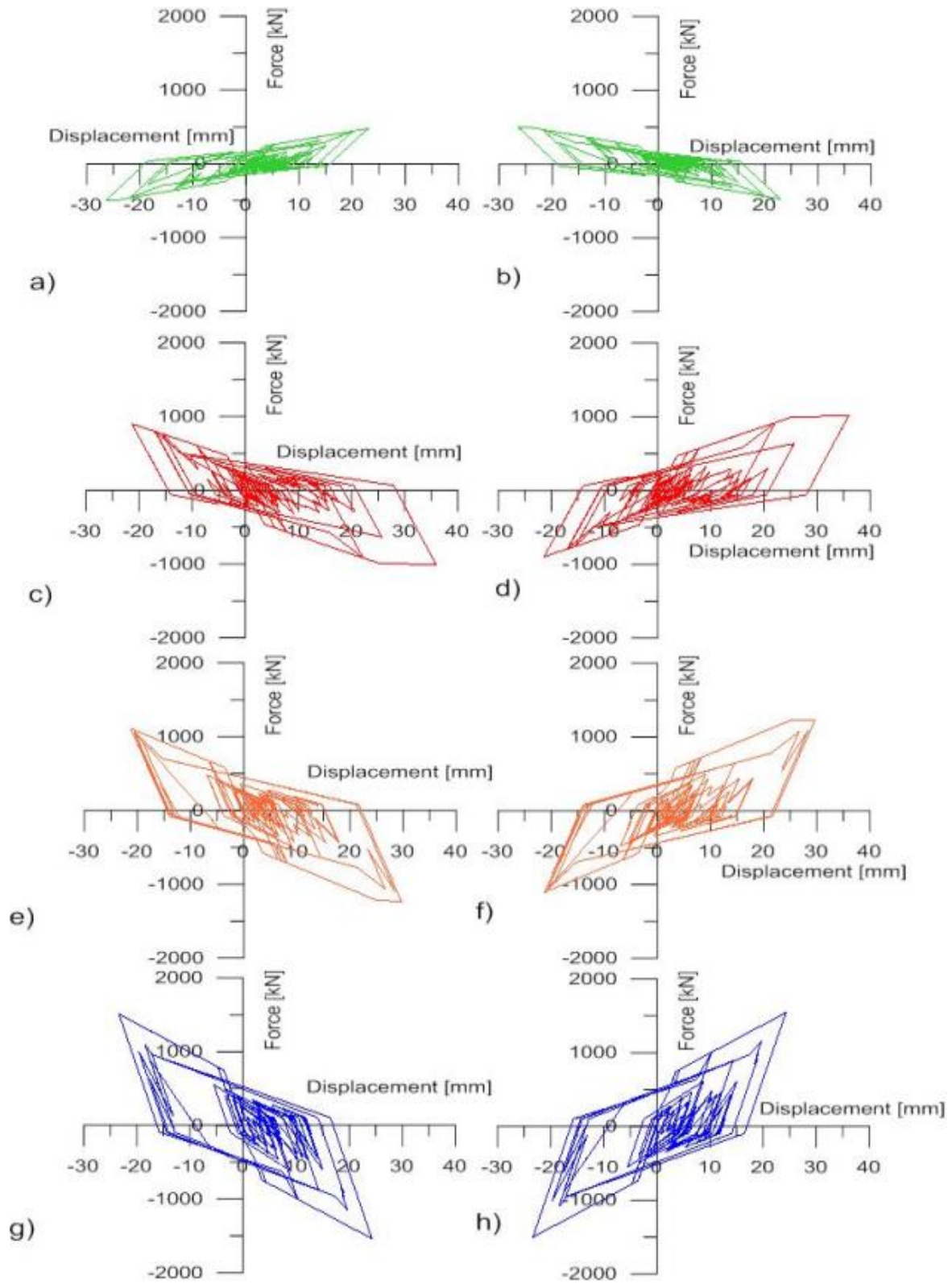


Figure 5.4. Time-history response in terms of force-displacement of double-pin joints under C5: a) 4th St. Brace 9-13 joint, b) 4th St. Brace 10-12 joint, c) 3rd St. Brace 6-10 joint, d) 3rd St. Brace 7-9 joint, e) 2nd St. Brace 2-7 joint, f) 2nd St. Brace 3-6 joint, g) 1st St. Brace 1-3 joint, h) 1st St. Brace 2-4 joint

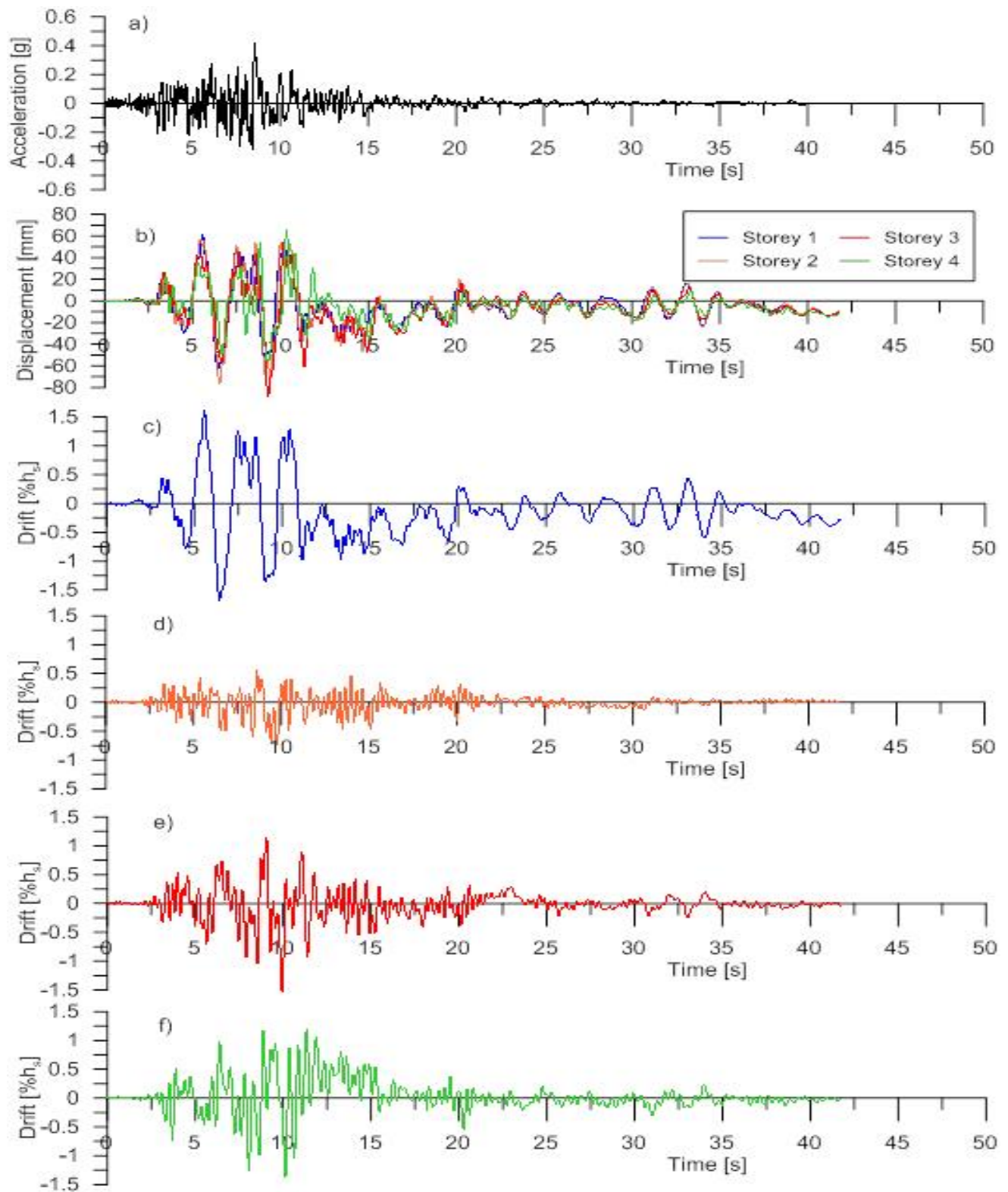


Figure 5.5. Time-history series obtained for CBF with pins in-parallel under C5: a) Scaled GM, b) Storey-displacement time-history series, c) 1st St. interstorey drift, d) 2nd St. interstorey drift, e) 3rd St. interstorey drift, f) 4th St. interstorey drift

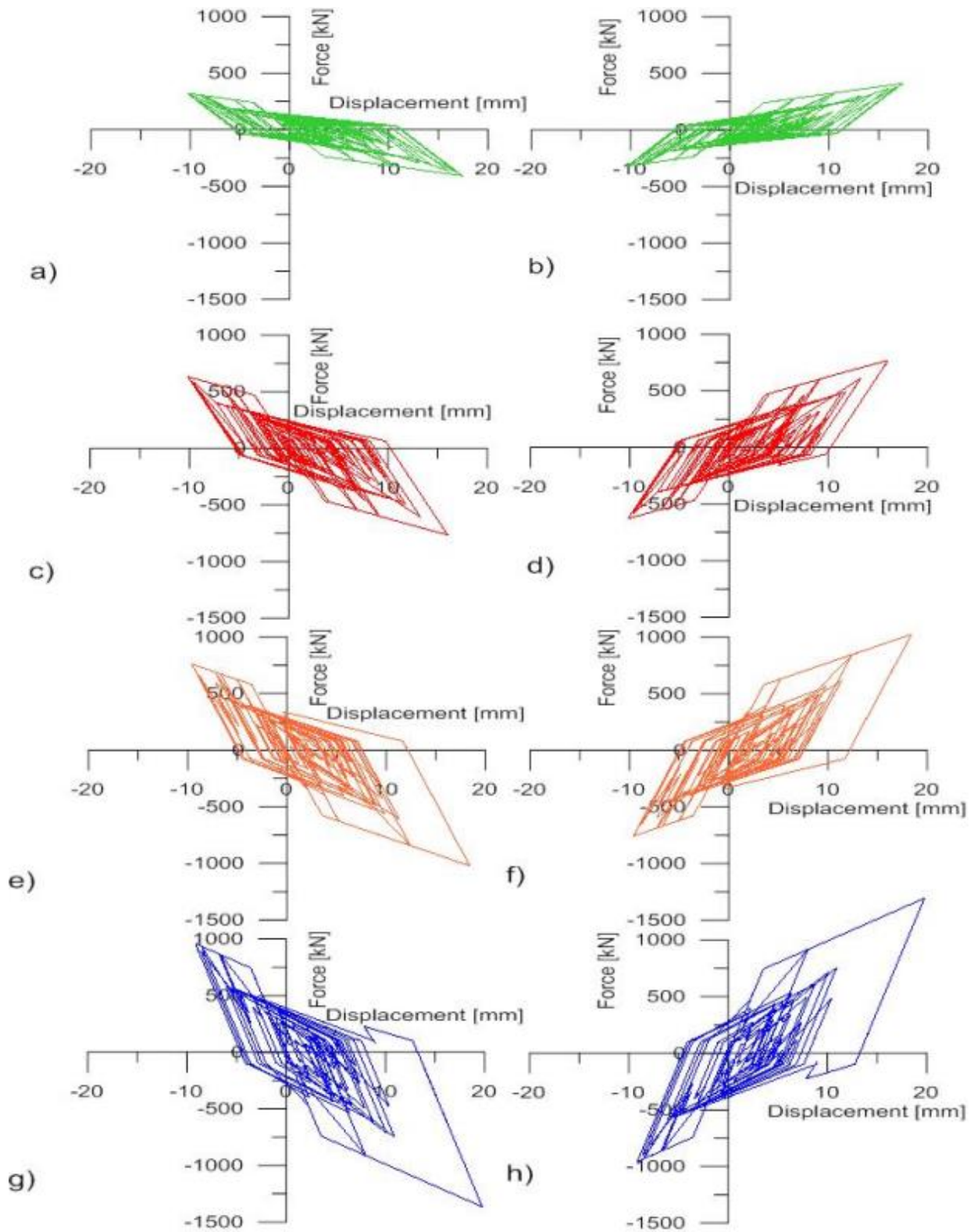


Figure 5.6. Time-history response in terms of force-displacement of double-pin joints under C7: a) 4th St. Brace 9-13 joint, b) 4th St. 4 Brace 10-12 joint, c) 3rd St. Brace 6-10 joint, d) 3rd St. Brace 7-9 joint, e) 2nd St. Brace 2-7 joint, f) 2nd St. Brace 3-6 joint, g) 1st St. Brace 1-3 joint, h) 1st St. Brace 2-4 joint

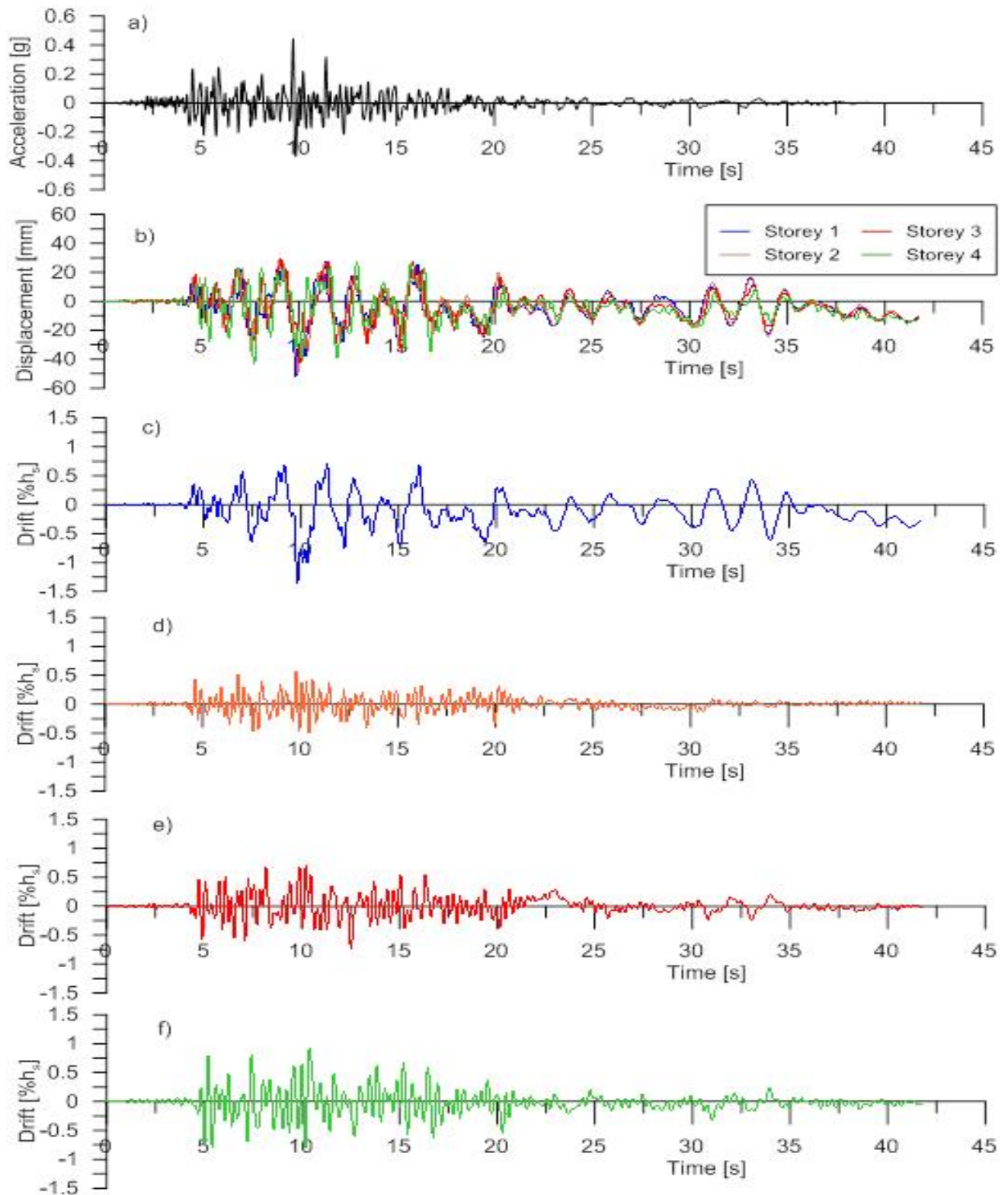


Figure 5.7 Time-history series obtained for CBF with pins in-parallel under C7: a) Scaled GM, b) Storey-displacement time-history series, c) 1st St. interstorey drift, d) 2nd St. interstorey drift, e) 3rd St. interstorey drift, f) 4th St. interstorey drift

Under the subduction S2 record even the 4th floor pins made of a rectangular 25x30mm cross-section reach their cumulative ultimate strength of 582.2kN at the time of 125s, when experienced a maximum displacement of 35mm, as shown in Figure 5.8. The S2 ground motion subjected the building to premature failure at t=125s, due to the accumulation of strain in the structural elements after the highest PGA reached at the t = 97.54 s (see S2 accelerogram) was passed. The storey-displacement time-history series are illustrated in Figure 5.9.

A similar premature failure was reached when the building was subjected to the S4 record. The collapse was reached at t = 126s after the building overpasses the highest accelerogram peak. The storey-displacement time-history series are illustrated in Figure 5.10.

It is recommended to apply a lower scaling factor to subduction ground motions in order to allow the structure to complete its inelastic cyclic incursion. Therefore, the subduction records impose larger damage to the CBF building with dissipative pin connections.

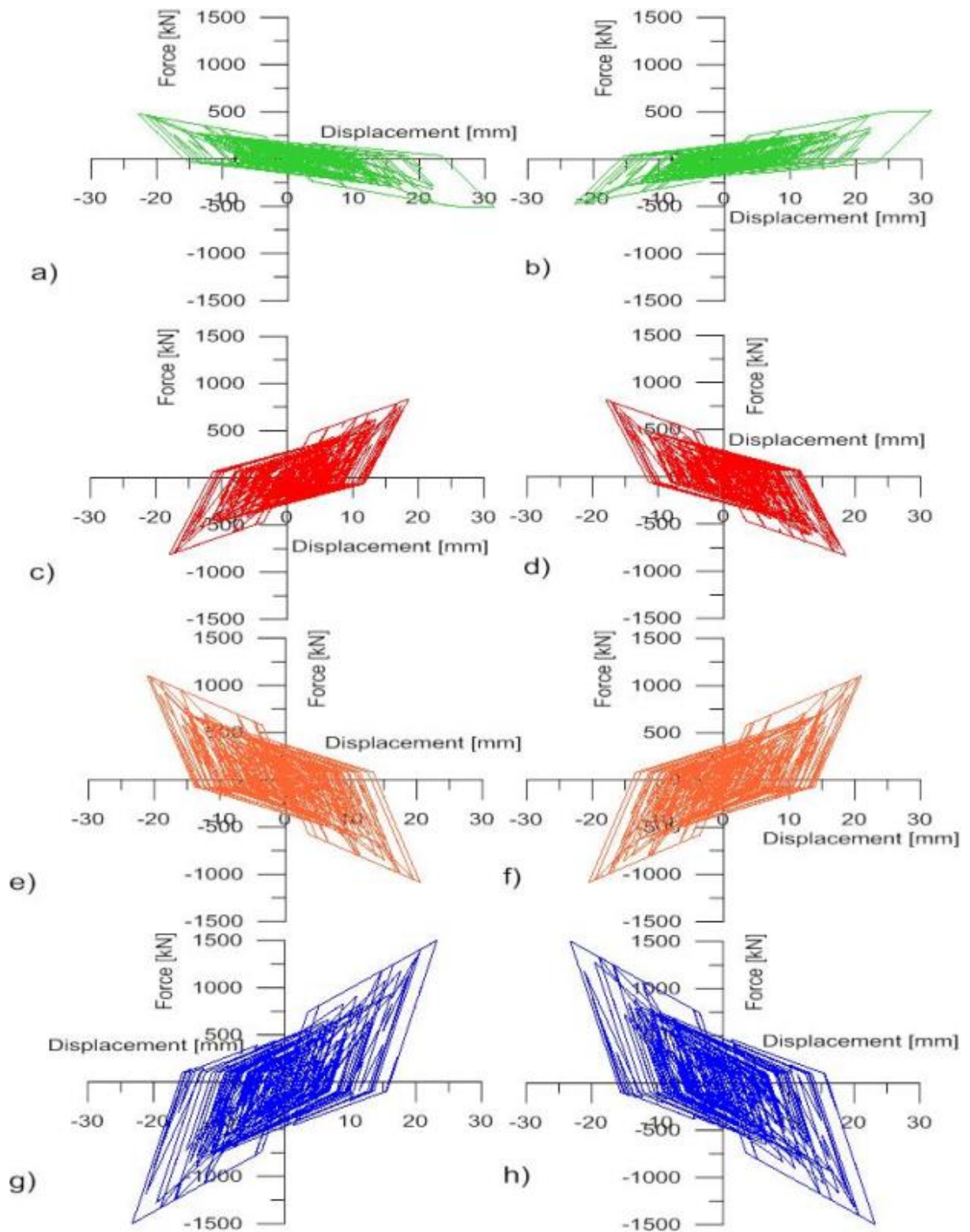


Figure 5.8. Time-history response in terms of force-displacement of double-pin joints under S2: a) 4th St. Brace 9-13 joint, b) 4th St. Brace 10-12 joint, c) 3rd St. Brace 6-10 joint, d) 3rd St. Brace 7-9 joint, e) 2nd St. Brace 2-7 joint, f) 2nd St. Brace 3-6 joint, g) 1st St. Brace 1-3 joint, h) St.1 Brace 2-4.

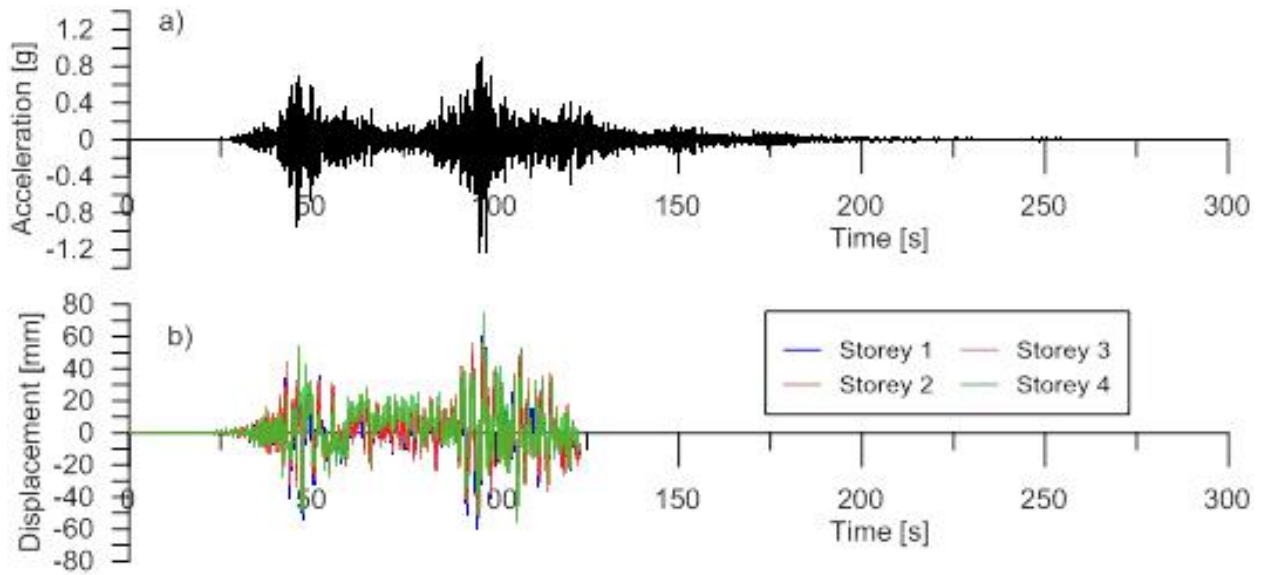


Figure 5.9. Time-history series obtained for CBF with double-pin joints displaced in-parallel under S2: a) Scaled GM, b) Storey-displacement

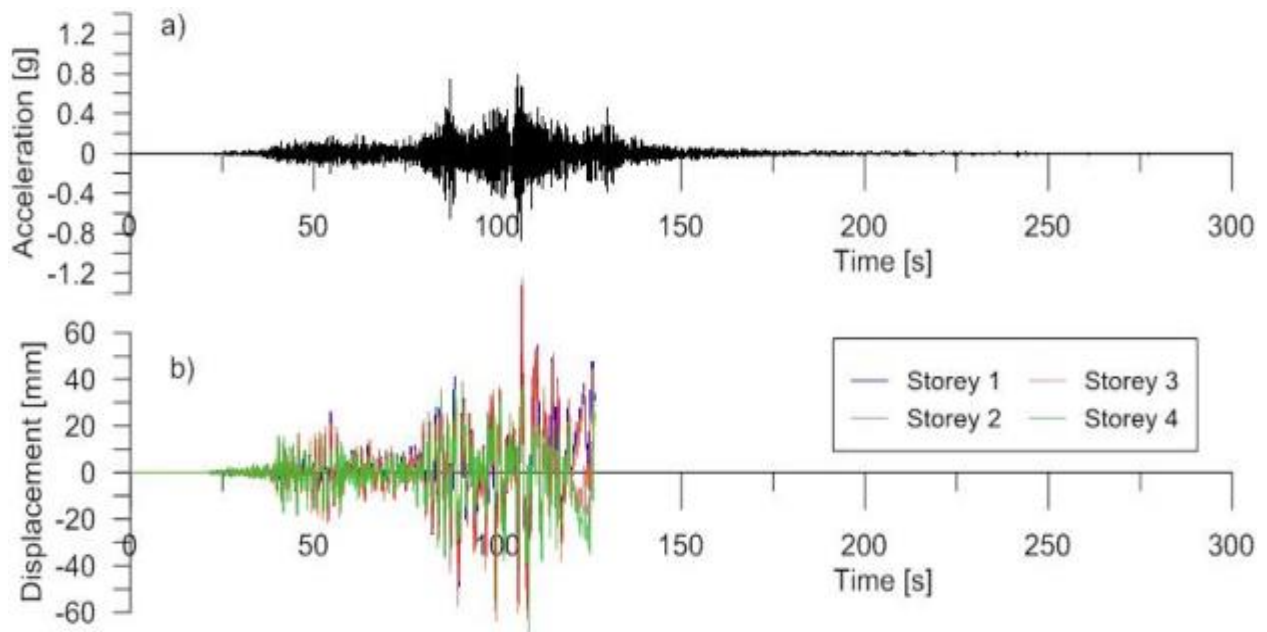


Figure 5.10. Time-history series obtained for CBF with double-pin joints displaced in-parallel under S4: a) Scaled GM, b) Storey-displacement time-history series.

5.5 CBFs with and without Double-pin Connections: Comparative Results

5.5.1 The analysis run time under selected ground motions

The run time results from the simulation of the CBFs with gusset plates that was illustrated in Chapter 4 and that obtained for the CBFs equipped with double-pin joints (DPP) as per Chapter 5 output are shown in Table 5.3 for the applied Crustal GMs and in Table 5.4 for the Subduction GMs. All analyses conducted in OpenSees on the CBF system successfully runs, while several models with incorporated double-pins fail to run completely. All ground motions have at their end a five seconds of zero acceleration amplitude in order to analyse the response under free vibrations.

Furthermore, in both aforementioned tables, for analyses that encountered failure are highlighted and a reduced scale factor was proposed. As resulted, when a slightly lower scale factor was applied (e.g. C1, C3, C4), the analysis was completed. A similar case was observed when the building was subjected to subduction ground motions.

Table 5.3: Crustal GMs total run time

Ground Motion	GMs total time (s)	CBF (s)	CBF with DPP (s)	CBF with DPP Initial Scale Factor	CBF with DPP Proposed Scale Factor
C1	39.6	44.6	27	2.2321	1.962
C2	40	45	45	1.0468	-
C3	39.57	44.57	23.5	1.4566	1.197
C4	40	45	28	0.813	0.709
C5	44.8	49.8	42.5	2.265	-
C6	60	65	65	2.263	-
C7	40	45	45	1.5281	-

Table 5.4: Subduction GMs total run time

Ground Motion	GMSs total time (s)	CBF run time (s)	CBF with DPP (s)	CBF with DPP Initial Scale Factor	CBF with DPP Proposed Scale Factor
S1	300	305	305	1	-
S2	300	305	125	1	0.876
S3	300	305	128	1	0.861
S4	300	305	126	1	0.836
S5	300	305	163	1	0.904
S6	300	305	305	1	-
S7	300	305	305	1	-

5.5.2 Interstorey drift and Residual interstorey drift resulted from all analyses

The interstorey drift expressed in percentage of h_s and resulted for CBFs with and without dissipative pin connections is show in Table 5.5. The residual (permanent) interstorey drift represents the interstorey drift of the last recorded value at the end of applied ground motions that included the 5 seconds free vibrations. The obtained residual interstorey drift values are given in Table 5.5 as well.

In order to collect data from the models that have initially failed the reduced scale factor was applied to corresponding ground motions and the results are also given in Table 5.5. As depicted in Table 5.5 a maximum residual drift of $0.6\%h_s$ resulted for both CBFs and CBFs with dissipative connections that were subjected for either crustal or subduction records.

Table 5.5. Interstorey and residual interstorey drift of CBF with and without double-pin

GM	ID	Storey	CBF	CBF + DPP	CBF	CBF + DPP	GM	Storey	CBF	CBF + DPP	CBF	CBF + DPP
			Drift % hs		Residual Drift % hs				Drift % hs		Residual Drift % hs	
C1	739-250	4	0.5	1.3	0.1	0.4	MYG001	4	0.55	1.2	0.16	0.19
		3	2.2	1.2	0.6	0.3		3	0.72	1.1	0.24	0.28
		2	1.4	0.8	0.2	0.1		2	0.68	0.6	0.22	0.25
		1	1.7	1.7	0.5	0.51		1	0.7	0.7	0.11	0.23
C2	767-0	4	1.2	1.2	0.4	0.15	MYG004	4	0.7	1.25	0.18	0.23
		3	0.9	1.1	0.2	0.2		3	1.5	1	0.28	0.21
		2	0.75	0.6	0.3	0.15		2	1.4	1.3	0.2	0.15
		1	0.7	0.7	0.25	0.25		1	1.8	1.7	0.45	0.59
C3	787-360	4	0.5	1.2	0.1	0.25	FKS005	4	0.5	0.9	0.17	0.18
		3	1.5	1.4	0.3	0.2		3	0.9	0.75	0.24	0.14
		2	1.4	1.1	0.15	0.15		2	0.9	0.7	0.18	0.13
		1	1.8	1.5	0.4	0.35		1	0.5	1.3	0.1	0.17
C4	963-90	4	0.6	0.9	0.3	0.2	FKS010	4	0.7	1	0.1	0.14
		3	1.3	1	0.3	0.3		3	1.6	1.2	0.25	0.13
		2	0.7	0.6	0.2	0.15		2	0.1	0.6	0.14	0.12
		1	1.8	1.6	0.45	0.5		1	1.8	2.1	0.23	0.18
C5	986-195	4	0.4	1.3	0.3	0.12	FKS009	4	0.87	0.7	0.23	0.18
		3	1.8	1.2	0.4	0.09		3	0.89	1.1	0.19	0.61
		2	1	0.5	0.2	0.11		2	0.75	0.65	0.17	0.13
		1	1.8	1.7	0.5	0.34		1	0.65	0.8	0.1	0.41
C6	1006-90	4	0.6	1	0.15	0.35	IBR004	4	0.6	1	0.1	0.5
		3	1.7	1.2	0.2	0.6		3	1.1	0.65	0.24	0.2
		2	1.8	0.7	0.3	0.1		2	0.8	0.8	0.13	0.13
		1	0.8	1.3	0.1	0.4		1	1.2	1.25	0.28	0.6
C7	1039-180	4	0.6	0.9	0.15	0.25	IBR006	4	0.95	1.1	0.17	0.26
		3	1.45	0.8	0.4	0.2		3	1.3	0.7	0.26	0.13
		2	1.3	0.7	0.25	0.1		2	1.4	0.55	0.1	0.05
		1	1.3	1.3	0.35	0.4		1	1.2	0.8	0.15	0.38

5.5.3 The Influence of *Pinching4* model parameters

In Chapter 3, the properties of *Pinching4* material used to model the pins behaviour have been calibrated according to experimental test results. However, in Figure 5.11, the effect of parameter *rForceP* on the overall response of CBF structure equipped with double-pin displaced in-parallel is studied under the *C7* ground motion. The *rDispP* value remained constant and equal to 0.7, while two different values were assigned to the *rForceP* parameter such as 0.65 and 0.45. The obtained results are depicted in Figure 5.11 in terms of force-deformation hysteresis loops generated under the *C7* ground motion. The time-history displacement series recorded at each floor are depicted for both variable *Pinching4* material parameters in Figure 5.12. The same *C7* record was considered.

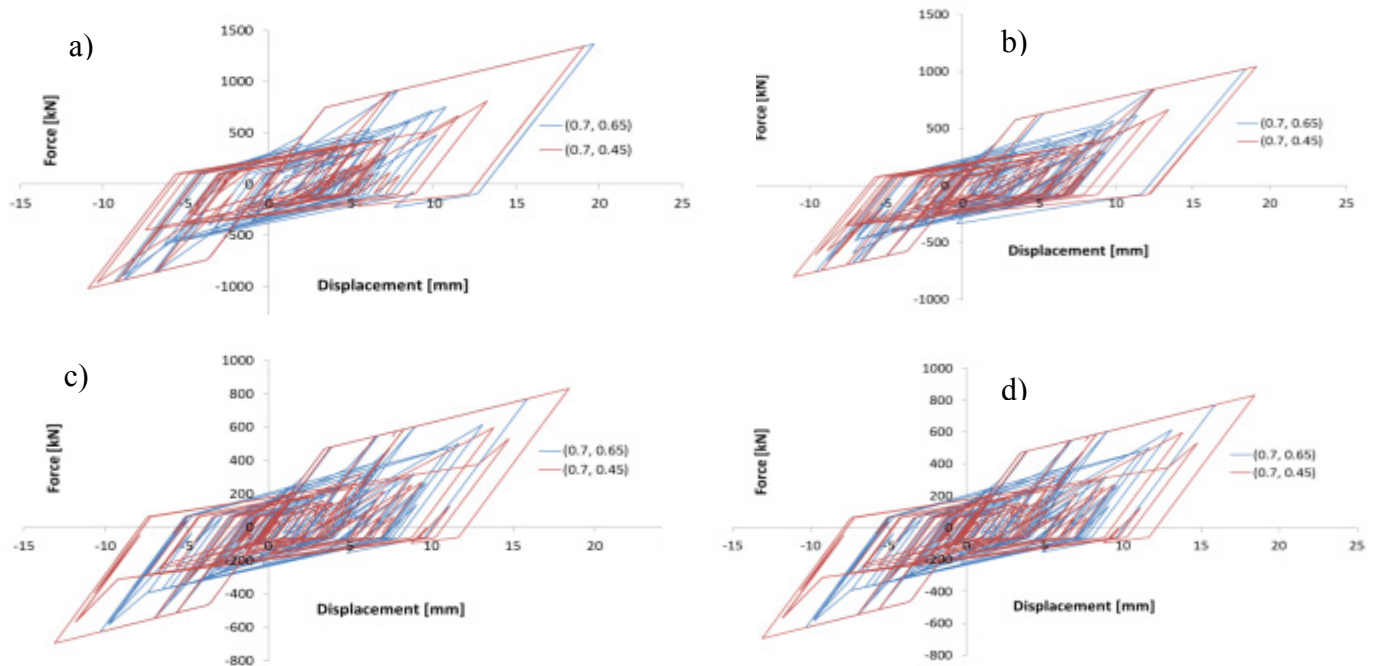


Figure 5.11. Hysteretic response of double-pin joints with pins in-parallel under *C7* record obtained for different *Pinching4* material parameters: *rForceP* = 0.65 and 0.45: a) 1st St. Brace 1-3 joint, b) 2nd St.2 Brace 2-7 joint, c) 3rd St. Brace 6-10 joint, d) 4th St. Brace 9-13 joint.

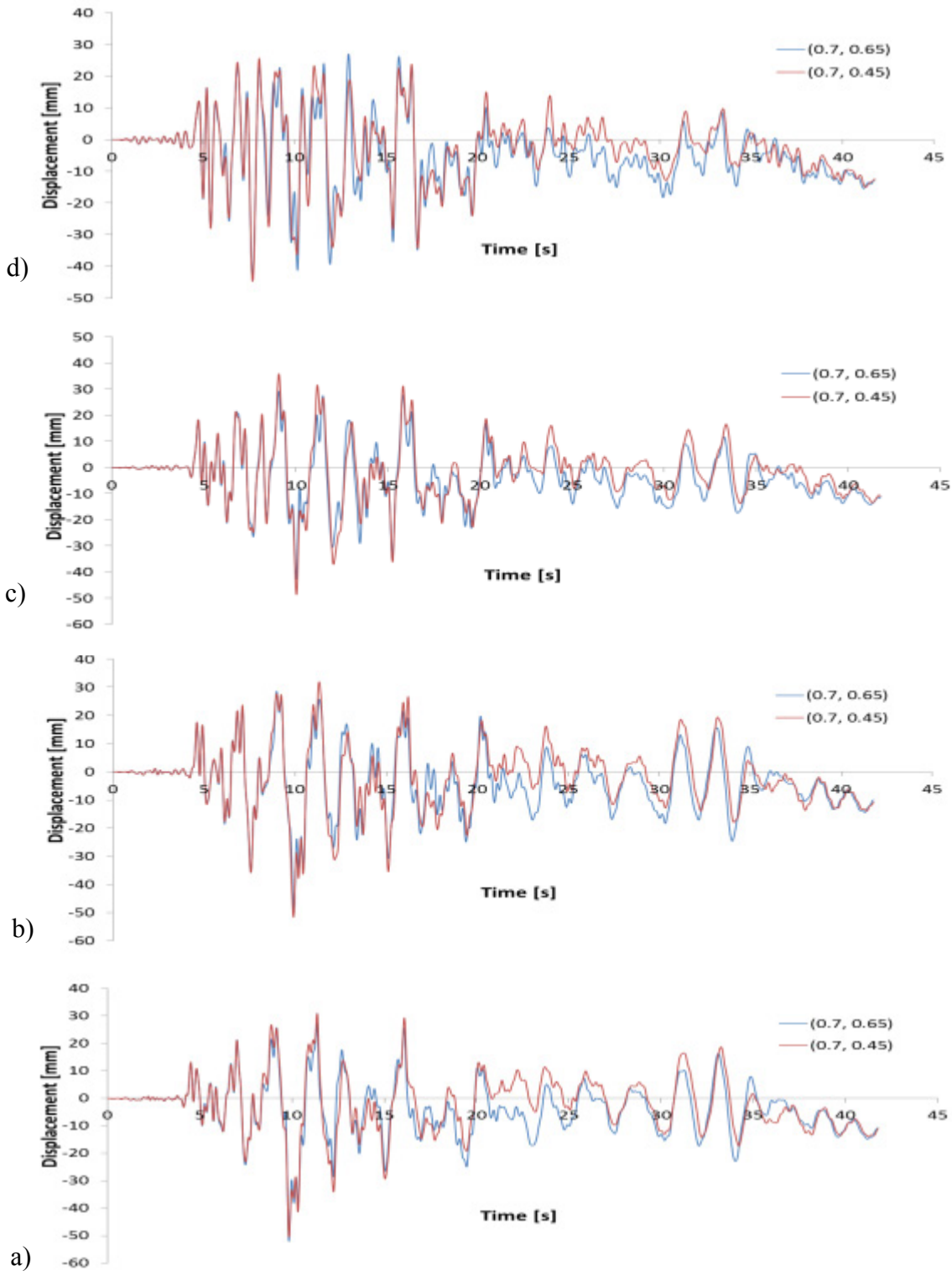


Figure 5.12. Time-history floor displacement series resulted under C7 record when *Pinching4* material parameter *rForceP* received 0.65 and 0.45 value: a) Storey 1, b) Storey 2, c) Storey 3, d) Storey 4.

The energy ratio obtained from the surface area of each cycle undergone by the brace equipped with dissipative double-pin connection is shown in Table 5.6. The energy ratio was computed when building was subjected to the C7 ground motion. The energy ratio was computed by divided the cumulative hysteresis loop area resulted under the calculation based on $rForce= 0.65$ to that obtained under the calculation based on $rForce= 0.45$.

Table 5.6. Energy ratio per cycle resulted by divided the hysteresis loops obtained for $rForce= 0.65$ to those obtained with $rForce= 0.45$

Cycle	Storey 1	Storey 2	Storey 3	Storey 4
2	1	1	0.33	1
3	1	1	1.58	1
4	1	1	0.84	1
5	1	1	0.28	1
6	1	1	8561	1
7	1	1	2.10	1
8	0.95	1	4.53	1
9	1.05	0.76	3.25	1
10	1.82	1.25	2.90	1
11	3.19	0.67	0.39	1
12	1.22	1.21	2.88	1.10
13	0.77	1.02	18.19	1.16
14	1.04	1.08	4.36	0.87
15		0.80	0.31	1.39
16		1.47	7.64	1.13
17		0.98	1.91	1.05
18				1.00
19				1.21

Chapter 6. Conclusions and Future work

6.1 Conclusions

In this research, the overall behaviour of two types of dissipative pin connections are emphasized, namely, single-pin and double-pin connections. The double-pin connection is represented in two configurations based on the position of pin members. Thus, the behaviour of double-pin connection with pins displaced in-line and in-parallel is discussed. Then, the seismic response of a 4-storey moderately ductile CBF system with and without dissipative connections is analysed, while comparative results between the behaviour of CBF systems with and without dissipative double-pin connections are discussed.

Referring to the behaviour, design and modelling of dissipative pin connections the following conclusions are formulated:

- Computations for pin connection design were carried out using the theoretical beam model and the OpenSees beam model under monotonic loading and cyclic quasi-static displacement loading. The proposed OpenSees model for the single-pin connection device was calibrated against experimental test results. The theoretical beam model is recommended for the preliminary design of dissipative pin connections.
- The OpenSees beam model employs the *Pinching4* material which represents a pinched force-deformation response and it allows users to simulate the deformed shape of the pin member in the outer-plate's hole support after it is loaded below its elastic capacity in bending.
- The dissipative energy capacity of connection devices, computed for the same number of cycles, increase if larger distance between the inner-plates, ($L_{pin}-2a$), is provided. When the distance between inner-plates increases, the portion of pin experiencing plastic deformation

expands across the pin's length, while the maximum stress and strain decrease. In all cases, the larger deformation was recorded at the pin's mid-span, while the larger strain was recorded in the vicinity of inner-plates that transfer the axial forces from the brace to the pin member. The tensile fibres show a slightly larger strain than the compression fibres. This difference increases with the magnitude of applied forces. By numerical studies, the distribution of plastic strains over the pin's length was recorded and in this light, the plastic hinge length is approximated as being: $(L_{pin}-2a + h_p)$, where h_p is the depth of the pin member.

- The length and thickness of the outer-plates influence the behaviour of the dissipative pin connections and the deflection of the pin controls the transversal deflection of outer-plates.
- When the distance between the outer- and inner-plate is larger than the distance between inner-plates, the failure of the pin member occurs in the longer pin segment at the external face of the inner-plate. In the case showing larger distance between inner-plates, the failure occurs in the middle segment, at the internal face of the inner-plate.
- By using double-pin connections, the load-carrying capacity of connection increases two times, while the deflection is similar to that experienced by an equivalent single-pin device. The double-pin connection with pins displaced in-line shows lower strains. Due to the large stiffness of the inner-plate in the plane of loading, both pins displaced in-line are subjected to equal deformation. The double-pin connection device with pins in-line has large redundancy, while displaying lower deflection, stresses and strains than an equivalent single-pin device.
- Additional experimental tests for single- and double-pin connections are required.

Previous research that assesses the behaviour of CBFs equipped with single-pin devices is taken further in this study. Thus, the same building plan is used for a 4-storey office building located in Victoria, B.C., for which the seismic response is analyzed.

- The moderately ductile 4-storey CBF system without and with pin devices was subjected to two sets of seven ground motions that are provided from crustal and subduction seismic sources. All ground motions were scaled as per ASCE/SEI-07 procedure. The building model was analysed using the OpenSees framework. Under crustal records, the CBF system with gusset plate brace-to-frame connections was subjected to large inelastic demand especially at the bottom two floor levels. Thus, braces were subjected to yielding in tension after buckled in compression. However, braces of the upper two floors remained in elastic range. The maximum interstorey drift was less than $2\%h_s$, while the maximum residual interstorey drift was less than $0.6\%h_s$. Under the Tohoku subduction records, the demand was larger. All braces experienced inelastic response with a larger demand at the bottom two floors. However, the maximum interstorey drift was less than $2\%h_s$ and the maximum residual interstorey drift was less than $0.6\%h_s$. Overall, the subduction records imposed larger seismic demand than crustal records.

Analyses conducted on the 4-storey CBF system with dissipative double-pin connections conduct to the following conclusions:

- The theoretical beam model can be used for preliminary design applications for low rise buildings. The pin overall connections are designed to yield at 60~80% of the buckling strength of braces, leading to an elastic response from the brace element. The proposed design steps are: i) design braces as per the moderately ductile CBF system, ii) build the tri-linear curve for pin device, iii) design the remaining structural members to remain in elastic range while pins dissipate energy.

- CBF system with dissipative pin connections have larger fundamental period of vibration and attract lower base shear forces. In general their fundamental period is 150% larger than that corresponding to the CBF system.
- The frames with pin dissipative connections reveal residual deformations in acceptable limits. The maximum residual interstorey drift is less than $0.6\%h_s$ under both crustal and subduction records. The maximum interstorey drift is less than $2.5\%h_s$.
- The CBFs with dissipative connections are sensitive to the frequency content of the ground motions. The encountered failure of the pins in a few crustal and subduction records is due to frequency content of ground motions. Tohoku records of magnitude 9 are too strong for the CBF designed based on the code provisions. Under Tohoku records the low-rise CBF buildings are at risk.
- Until further experimental tests are conducted, it is not recommended to select CBF with in-line or in-parallel connections in seismic areas. This type of double-pin connection has large redundancy.
- The energy dissipating capability of the dissipative pin connections is almost the same as the brace behaving in tension or compression with the advantage of a uniform distribution of results between tension and compression cycles. For middle-rise buildings located in high seismically activity areas, the in-line and parallel pin connections are recommended instead of the single-pin connection devices. The CBF systems with dissipative connections provide a reduced overall cost. These connections are easy replaceable after the occurrence of damage.

- Experimental testing of the dissipative connections with different outer plate and inner plate thicknesses is required to better clarify the effect of the outer plate in bending and the inner plate in axial force as a whole to the overall connection design;

- Numerical modelling with multi-pins connections correlated and calibrated to the results from a testing procedure of the overall connections response and the evaluation of each dimension in Figure 6.1 for the response of the connection.

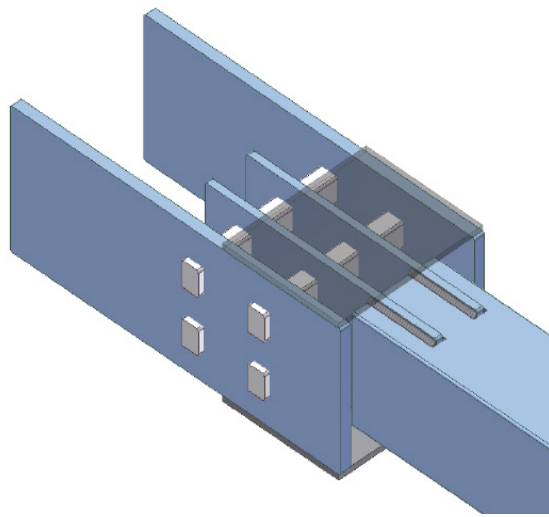


Figure 6.2: Reinforced multi-pin connections

- Overall response of the connection with the outer plates stiffened and restrained by a welded plate as in Figure 6.2, for a better evaluation of the outer plates bearing imposed upon the connection.

Further studies are necessary on the behaviour of the dissipative connections embedded into higher levels of structural frames for a better evaluation of the residual deformation response in regards to ground motions characterised by long periods and high amplitudes.

References

- Calado , L. (2004). Lisbon Experimental Test Results.
- Calado, L., Ferreira, J., & Feligioni, S. (2004). *Characterization of Dissipative Connectios for Concentric Bracing System in Steel Frames in Seismic Areas*. Instituto Superior Tecnico. Instituto Superior Tecnico in Lisboa.
- Caprarelli, C. (2012). *Modelling and design of earthquake resistant low-rise Concentrically Braced Frames with dissipative single-pin connections*. Montreal, Canada: Concordia University.
- Castiglioni, C. (2010). Milano experimental test results.
- Chou, C.-C., & Chen, P.-J. (May 2009). Compressive behavior of central gusset plate connections for a buckling-restrained braced frame. *Journal of Constructional Steel Research*, 65(5), 1138-1148.
- Constantinou, M. a. (1993). *Seismic Response of Structures with Supplemental damping. The Structural Design of Tall Buildings*.
- CSA. (2009). *Design of Steel Structures*. Toronto, Ontario: Canadian Standard Association.
- Desjardins, E., & Legeron, F. (2010). Method to reduce seismic demand on connections of Concentrically Braced systems. *2nd International Structures Specialty Conf*. Winnipeg, Manitoba: CSCE.
- ECCS (Ed.). (1986). *Seismic Design Recommended Testing Procedure For Assessing the Behaviour of Structural Steel Elements Under Cyclic Loads* (Vol. TWG 1.3.). Brussels, Belgium: Technical Committee - Structural safety and loading.

- European Committee for Standardization. (n.d.). Design of steel structures. In *Eurocode 3* (EN1993-1-9-2005 ed.). Brussels, Belgium.
- Federal Emergency Management Agency. (2000). *Prestandard and commentary for the seismic rehabilitation of buildings* (Vol. FEMA 356). Washington, D.C., U.S.A.: Building Seismic Safety Council of the National Institute of Building Services.
- Gray, M., Christopoulos, C., & Packer, J. (2010). Cast steel yielding fuse for concentrically braced frames. *9th U.S. Nat. & 10th Can. Conf. on Earthquake Eng., Paper No. 595*. Toronto, Ontario.
- Hsiao, P., Lehman, D., & Roeder, C. (2012). Improved analytical model for special concentrically braced frames. *Journal of Constructional Steel Research*, 73:80-94.
- Izverani, C. (2007). *The seismic behaviour of steel braces with large sections*. Montréal: Département des Génies Civil, Géologique et des Mines. École Polytechnique de Montréal.
- Kalkan, E., & Chopra, A. (2010). . *Practical guidelines to select and scale earthquake records for nonlinear response history analysis of structures*. USGS.
- Kassis, D., & Tremblay, R. (2008). *Brace fuse system for cost effective design of low-rise steel buildings*. Paper No. 248. Quebec, QC: CSCE 2008 Annual Conference.
- Mazzoni, S., McKenna, F., Scott, M., & Fenves, G. (2006). *OpenSees command language manual*. (P. E. Center, Ed.) Berkeley, U.S.A.: University of California.
- McKenna, F., Scott, M., & Fenves, G. (2009). *Open system for earthquake engineering simulation*.
- NRCC. (2010). *National Building Code of Canada 13th Edition*. Ottawa, Ontario: National Research Council of Canada.

- Plumier, A., Castiglioni, C., Vayas, I., & Calado, L. (2004). Behaviour of seismic resistant braced frame with innovative dissipative connections. *EUROSteel*. Maastricht, The Netherlands.
- Plumier, A., Doneux, C., Castiglioni, C., Brescianini, J., Crespi, A., Dell'Anna, S., et al. (2004). *Two innovations for earthquake resistant design*. EUR 22044EN, Technical Steel Research, European Commission.
- Plumier, A., Doneux, C., Castiglioni, C., Brescianini, J., Crespi, A., Dell'Anna, S., et al. (2006). *Two innovations for earthquake resistant design*. European Commission.
- Rezai, M., Prion, H., Tremblay, R., Boutay, N., & Timler, P. (2000). Seismic Performance of Brace Fuse Elements for Concentrically Steel Braced Frames. *Stessa*, (pp. 39-46). Montreal.
- St-Onge, E. (2012). *Comportement et conception sismique des fusibles ductiles pour les structures en acier*. Montreal, Canada: Ecole Polytechnique.
- Technical Committee - Structural safety and loading. (1986). *TWG 1.3 Seismic Design Recommended Testing Procedure for Assessing the Behaviour of Structural Steel Elements under Cyclic Loads*. Brussels, Belgium.
- Thanopoulos, P. (2006). *Behaviour of seismic resistant steel frame with energy absorbing devices*. Athens, Greece: National Technical University of Athens.
- Tirca, L., Caprarelli, C., & Danila, N. (17 June 2011). Behaviour of a Low Rise Concentrically Braced Frame Building with and without Dissipative Pin Connections. *CSCE Annual*. Ottawa, ON.

- Tirca, L., Caprarelli, C., & Danila, N. (2012, December 16). Seismic Simulation and Design of Low-Rise CBF Buildings with and without Dissipative Connectuins using OpenSees. *STESSA*, (pp. 365-371). Santiago, Chile.
- Tirca, L., Caprarelli, C., Danila, N., & Calado, L. (2012). Modelling and Design of Dissipative Connections for Brace to Column Joints. *7th International workshop on connections in steel structures*. Timisoara, Romania.
- Tirca, L., Danila, N., & Caprarelli, C. (2013). Numerical Modelling for dissipative pin devices for brace column connections. *Journal of Constructional Steel Research*, "in print".
- Tirca, L., Morales, J., Guo, G., & Chen, L. (2010). Optimal design of friction dampers for multi-storey buildings. *9th US National and 10th Canadian Conference on Earthquake Engineering: Reaching Beyond Borders*. Toronto, ON, Canada: EERI.
- Tremblay, R., St-Onge, E., Rogers, C., Morrison, T., Legeron, F., Desjardins, E., et al. (2011). Overview of ductile seismic brace fuse systems in Canada. *EUROSteel Conf*, (pp. 939-945). Budapest.
- Vayas, I., & Thanopoulos, P. (2005). Innovative dissipative (INERD) pin connections for seismic resistant frames. *int. Journal of Steel Structures*, Vol. 5.
- Vayas, I., & Thanopoulos, P. (2006). Dissipative (INERD) connections for seismic resistant steel braced frames. *DOI: 10.1002/stab.200610108*.
- Ziemian, R. (2010). *Guide to stability design criteria for metal structures*. J. Wiley & Sons.